

**AB INITIO STUDY OF STRUCTURAL STABILITY AND ELECTRONIC  
PROPERTIES OF  $\text{ZrO}_{2-x}\text{S}_x$  FOR  $0 \leq x \leq 2$**

By

**Masilu Godfrey Mulaudzi**

DISSERTATION

Submitted in fulfillment of the requirements for the degree of

**Master of Science**

In

**Physics**

In the

**FACULTY OF SCIENCE AND AGRICULTURE**

**(School of Physical and Mineral Sciences)**

At the

**UNIVERSITY OF LIMPOPO (Turfloop Campus)**

**SUPERVISOR: Dr. L. Ackermann**

**CO-SUPERVISOR: Prof. P.E. Ngoepe**

**2015**

### **Declaration**

I declare that the dissertation hereby submitted to the University of Limpopo (Turfloop Campus) for the degree of Master of Science has not previously been submitted by me for a degree at this or any other university, that it is my own work both in design and execution, and that all material contained herein has been duly acknowledged.

**Mr M.G Mulaudzi**

**Surname, Initials (title)**

\_\_\_\_\_

**Date**

## **Acknowledgments**

I would like to thank:

- My Supervisors and advisors, Dr Lutz Ackermann and Professor Phuti Ngoepe, who taught me the art of finding good research topics and how to handle research.
- The Material Modelling Centre (MMC) members, who kept life interesting by providing numerous occasions to chat about science and life in general.
- My parents, who have always encouraged me to pursue my studies although things were rough.
- My friends from far away, who did not forget about me for these tough years.
- My Fiancee, Mokhithi, for her support and encouragements, for keeping me from turning into a mad scientist, and for basically everything else.
- The Material Modelling Centre administrator Mr Jacob Mothapo for the encouraging words that's inspired me to work hard.
- Sponsors of this project: University of Limpopo (UL) and the National Research Foundation.

## **Dedications**

This work is dedicated to:

### **My wonderful Baby girl and Baby boy**

Tebogo Abigail and fhulufhelo Godfrey

### **My wonderful Wife**

Mokhithi

### **My wonderful siblings**

Mbulaheni, Phophi, Thabelo and Rofhiwa

### **My wonderful mother and father**

Matshiba and Azwihangwisi

**Ndi a livhuwa!!**

## Abstract

While the effect of sulphur on  $c\text{-ZrO}_2$  is often considered in application of advanced solid oxide fuel cells and biomass gasification cleanup, there has been little study on the effect of sulphur on general structure of  $c\text{-ZrO}_2$ . In this work a study of the structural, energetic, electronic and elastic properties of doped  $c\text{-ZrO}_{2-x}\text{S}_x$ ,  $t\text{-ZrO}_{2x}\text{S}_x$  and  $m\text{-ZrO}_{2-x}\text{S}_x$  solid solutions has been carried out using *ab-initio* total energy calculation of the density functional theory under plane wave pseudopotential method within generalized gradient approximation using the self-consistent virtual crystal approximation (VCA). It has been shown that all the calculated properties obtained after relaxation are in good agreement with available experimental and other calculated values, particularly at  $x=0$ . Furthermore, the formation and cohesive energies were calculated to determine the relative stability of all three non-sulphated and sulphated polymorphs of  $\text{ZrO}_2$ . The density of states and band structures have been computed for  $x = 0.0 - 0.5$ , and the actual size of the band gap of  $\text{ZrO}_2$  compounds narrowed with partial replacement of oxygen by sulphur, while peaks above Fermi level move towards the Fermi level. The material changes its insulating properties to semiconductor material as a function of sulphur concentration, which might be useful for potential application. We also investigated and calculated, for the first time, the effect composition variation on mechanical stability, the independent elastic constants and other elastic parameters of the sulphated compounds. The polycrystalline bulk moduli, shear moduli, Young and Poisson's ratio have been deduced by using Voight-Reuss-Hill (VRH) approximation. In addition we also show the geometric and electronic structure of pure  $\text{ZrOS}$  and  $\text{ZrS}_2$  and compare them with the obtained geometric and electronic structures of  $\text{ZrO}_{2-x}\text{S}_x$ .

## Contents

CHAPTER 1 .....	1
1. Background and aim of research .....	1
1.1. Zirconium dioxide .....	2
1.2. Crystal structure of Zirconium oxide:.....	3
1.3. Phase transformation: .....	5
1.4. $c$ -ZrO <sub>2</sub> and sulphur contact in biomass gasification .....	8
1.5. Comparison of ZrO <sub>2</sub> , ZrOS and ZrS <sub>2</sub> .....	8
1.6. Background on methodology and properties to be investigated.....	10
1.6.1. Heats of formation, formation enthalpy and cohesive energy .....	12
1.6.2. Elastic Constants.....	12
1.6.3. Electronic density of states and electron charge density difference .....	12
1.7. Objectives .....	13
CHAPTER 2 .....	14
2. Ab initio methods .....	14
2.1. Electron density instead of the wavefunction .....	14
2.2. Crystals and Unit Cells.....	17
2.3. Approximations for the Exchange-Correlation Functional .....	18
2.3.1. Local Density Approximation (LDA).....	18
2.3.2. Generalized Gradient Approximation (GGA) .....	20
2.3.3. Hybrid Functionals.....	21
2.4. DFT as implemented in codes.....	22
2.5. Planewave pseudopotential method .....	22
2.5.1. Planewaves and pseudopotentials .....	23
2.5.2. Pseudopotential approximation .....	25
2.6. $k$ -sampling.....	26
2.7. Theoretical approach to the solid solution or alloys problem.....	28

2.7.1.	Ramer and Rappe VCA Approach.....	29
2.7.2.	Bellaiche and Vanderbilt VCA Approach .....	29
2.8.	Numerical details and theory of properties to be investigated .....	30
2.8.1.	Cohesive and formation energy .....	30
2.8.2.	Elastic properties .....	31
2.9.	Density of states.....	36
2.10.	Calculation Steps of the Work.....	37
CHAPTER 3 .....		38
3.	Results and discussions .....	38
3.1.	Cut-off energy and k-points convergence of $ZrO_{2-x}S_x$ .....	38
3.1.1.	Cut-off energy.....	38
3.1.2.	k-points .....	38
3.1.3.	Summary of cut-off energies and <i>k</i> -points .....	40
3.2.	Structural properties .....	40
3.2.1.	Crystal structure .....	40
3.2.2.	Formation energies and cohesive energies.....	50
3.2.3.	Summary of structural properties.....	55
3.3.	Density of states.....	56
3.3.1.	Electronic properties .....	56
3.3.2.	Summary of electronic properties .....	75
3.4.	Mechanical properties .....	76
3.4.1.	Single crystal elastic constants .....	77
3.5.2.	Polycrystalline elastic properties .....	86
3.5.3.	Summary of mechanical stability .....	104
CHAPTER 4 .....		106
4.1.	Conclusions and summary .....	106
4.2.	Future work and recommendations.....	109

BIBLIOGRAPHY ..... 110



## LIST OF TABLES

Table 1 Physical properties of zirconium oxide ( $ZrO_2$ ) .....	3
Table 2 Crystallographic data for cubic, tetragonal and monoclinic zirconia .....	4
Table 3 Crystallographic data for zirconium disulphide and zirconiumoxysulphide ..	10
Table 4 Calculated structural parameters $c$ - $ZrO_2$ and of corresponding available theoretical calculations. ....	41
Table 5 The optimised structural parameters of $ZrOS$ , $ZrO_{1.5}S_{0.5}$ and $ZrS_2$ .....	41
Table 6 Experimental, calculated and other first principle lattice parameters for $t$ - $ZrO_2$ .....	46
Table 7 Experimental, calculated and other first principle lattice parameters and angle $\beta$ for $m$ - $ZrO_2$ .....	46
Table 8 Calculated cohesive energy (eV) and formation energies (eV) for undoped and Sulphur-doped zirconia. Bracketed values are from other theoretical work.....	51
Table 9 Comparison of the band gap values obtained in this work with previous calculations and experiment. Energy values are given in eV .....	57
Table 10 calculated, theoretical and experimental elastic constant for $c$ - $ZrO_2$ .Exp.: experimental data; WC: present work; HF: Hartree-Fock; TB: tight binding; PIB: potential-induced breathing; LD: lattice dynamics .....	77
Table 11 Variation of lattice independent elastic constant for $c$ - $ZrO_{2-x}S_x$ for $0 \leq x \leq 2$ ..	78
Table 12 calculated, theoretical and experimental elastic constant for $t$ - $ZrO_2$ .; see key of table 11. (c) Indicates that the elastic constant is given in the cubic axes,(t) in primitive tetragonal axes, and no indication means chosen set of axes unknown....	79
Table 13 Variation of independent lattice elastic constant for $t$ - $ZrO_{2-x}S_x$ for $0 \leq x \leq 2$ ...	80
Table 14 Calculated, theoretical and experimental independent elastic constant for $m$ - $ZrO_2$ . PAW: projected augmented wave. See key of Table 11 .....	82
Table 15 Variation of calculated independent elastic constant for $m$ - $ZrO_{2-x}S_x$ for $0 \leq x \leq 2$ .....	83
Table 16 Anisotropy ratios for $m$ - $ZrO_{2-x}S_x$ for $x = 0$ .....	102

## LIST OF FIGURES

Figure 1 Structural models of three polymorphic forms of $ZrO_2$ , a) cubic, b) tetragonal and c) monoclinic crystal lattice.....	4
Figure 2 A comparison of the methodology for solving the many-body Schrödinger equation and effective one-electron Kohn-Sham equation [77]......	17
Figure 3 Schematic of the LDA (Koch & Holthausen) [83]......	19
Figure 4 Comparison of a wavefunction in the Coulomb potential of the nucleus (blue) to the one in the pseudopotential (red). The real and the pseudowavefunction and potentials match above a certain Cut-off. ....	27
Figure 5 The graphs of total energy (eV/atom) against energy cut-off and total energy (eV/atom) against number of k -points for the $c-ZrO_2$ .....	39
Figure 6 Variation of the lattice parameter and volume expansion rate with S mole fraction x, in $c-ZrO_{2-x}S_x$ solid solution. ....	43
Figure 7 Variation of the lattice constant dilation or shrinkage with S mole fraction x. for $c-ZrO_{2-x}S_x$ solid solution. ....	44
Figure 8 Variation of bond length (Å) with S mole fraction x in $c-ZrO_{2-x}S_x$ solid solution.....	44
Figure 9 Variation of the lattice parameters and volume expansion rate with S mole fraction x for $t-ZrO_{2-x}S_x$ solid solution.....	47
Figure 10 Variation of the lattice parameters and volume expansion rate with S mole fraction x for $m-ZrO_{2-x}S_x$ solid solution.....	48
Figure 11 Variation of a) axial ratio (c/a) of $t-ZrO_{2-x}S_x$ , b) lattice anisotropy (c/b) and c) monoclinic angle $\beta$ of $m-ZrO_{2-x}S_x$ solid solutions with S mole fraction x. ....	49
Figure 12 Variation of the formation energy and cohesive energy with S mole fraction for $c-ZrO_{2-x}S_x$ solid solution. ....	52
Figure 13 Variation of the formation energy and cohesive energy with S mole fraction for $t-ZrO_{2-x}S_x$ solid solution .....	53
Figure 14 Variation of the formation energy and cohesive energy with S mole fraction for $m-ZrO_{2-x}S_x$ solid solution .....	54
Figure 15 Crystal structures of (a) ZrOS (b) $c-ZrO_2$ and (c) $ZrS_2$ .....	56
Figure 16 Total BS and DOSs of the a) unsulphated $c-ZrO_2$ and sulphated $c-ZrO_2$ , b) $c-ZrO_{1.9}S_{0.1}$ and c) $c-ZrO_{1.8}S_{0.2}$ structures.....	58

Figure 17 Partial DOSs of the a) unsulphated $c\text{-ZrO}_2$ , and sulphated $c\text{-ZrO}_2$ , b) $c\text{-ZrO}_{1.9}\text{S}_{0.1}$ and c) $c\text{-ZrO}_{1.8}\text{S}_{0.2}$ structures.....	59
Figure 18 Total BS and DOSs of the sulphated $c\text{-ZrO}_2$ , a) $c\text{-ZrO}_{1.7}\text{S}_{0.3}$ , b) $c\text{-ZrO}_{1.6}\text{S}_{0.4}$ and c) $c\text{-ZrO}_{1.5}\text{S}_{0.5}$ structures. ....	60
Figure 19 Partial DOSs of the sulphated $c\text{-ZrO}_2$ , a) $c\text{-ZrO}_{1.7}\text{S}_{0.3}$ , b) $c\text{-ZrO}_{1.6}\text{S}_{0.4}$ and c) $c\text{-ZrO}_{1.5}\text{S}_{0.5}$ structures. ....	61
Figure 20 a) Total BS and DOSs, and b) Partial DOSs of ZrOS. ....	63
Figure 21 Total BS and DOSs of the a) unsulphated $t\text{-ZrO}_2$ and sulphated $t\text{-ZrO}_2$ , b) $t\text{-ZrO}_{1.9}\text{S}_{0.1}$ and c) $t\text{-ZrO}_{1.8}\text{S}_{0.2}$ structures. ....	65
Figure 22 Partial DOSs of the a) unsulphated $t\text{-ZrO}_2$ and sulphated $t\text{-ZrO}_2$ , b) $t\text{-ZrO}_{1.9}\text{S}_{0.1}$ and c) $t\text{-ZrO}_{1.8}\text{S}_{0.2}$ structures. ....	66
Figure 23 Total BS and DOSs of the sulphated $t\text{-ZrO}_2$ , a) $t\text{-ZrO}_{1.7}\text{S}_{0.3}$ , b) $t\text{-ZrO}_{1.6}\text{S}_{0.4}$ and c) $t\text{-ZrO}_{1.5}\text{S}_{0.5}$ structures. ....	67
Figure 24 Partial DOSs of sulphated $t\text{-ZrO}_2$ , a) $t\text{-ZrO}_{1.7}\text{S}_{0.3}$ , b) $t\text{-ZrO}_{1.6}\text{S}_{0.4}$ and c) $t\text{-ZrO}_{1.5}\text{S}_{0.5}$ structures. ....	68
Figure 25 Total BS and DOSs of the a) unsulphated $m\text{-ZrO}_2$ and sulphated $m\text{-ZrO}_2$ , b) $m\text{-ZrO}_{1.9}\text{S}_{0.1}$ and c) $m\text{-ZrO}_{1.8}\text{S}_{0.2}$ structures. ....	69
Figure 26 Partial DOSs of the a) unsulphated $m\text{-ZrO}_2$ and sulphated $m\text{-ZrO}_2$ , b) $m\text{-ZrO}_{1.9}\text{S}_{0.1}$ and c) $m\text{-ZrO}_{1.8}\text{S}_{0.2}$ structures. ....	70
Figure 27 Total BS and DOSs of the sulphated $m\text{-ZrO}_2$ , a) $m\text{-ZrO}_{1.7}\text{S}_{0.3}$ , b) $m\text{-ZrO}_{1.6}\text{S}_{0.4}$ and c) $m\text{-ZrO}_{1.5}\text{S}_{0.5}$ structures. ....	71
Figure 28 Partial DOSs of the sulphated $m\text{-ZrO}_2$ , a) $m\text{-ZrO}_{1.7}\text{S}_{0.3}$ , b) $m\text{-ZrO}_{1.6}\text{S}_{0.4}$ and c) $m\text{-ZrO}_{1.5}\text{S}_{0.5}$ structures. ....	72
Figure 29 a) Total BS and DOSs, and b) Partial DOSs and of the $\text{ZrS}_2$ structures...	74
Figure 30 Variation of bandgaps of $(ctm)\text{-ZrO}_{2-x}\text{S}_x$ solid solution for $x=(0-0.5)$ .....	75
Figure 31 Variation of the tetragonal structure mechanical stability criterion with S mole fraction for $t\text{-ZrO}_{2-x}\text{S}_x$ solid solution.....	81
Figure 32 Variation of the monoclinic structure mechanical stability criterion with S mole fraction for $m\text{-ZrO}_{2-x}\text{S}_x$ solid solution.....	84
Figure 33 Variation of the monoclinic structure mechanical stability criterion with S mole fraction for $m\text{-ZrO}_{2-x}\text{S}_x$ solid solution.....	85
Figure 34 Variation of the a) $C'$ , b) $C_{44}$ and c) $E$ of S mole fraction for $c\text{-ZrO}_{2-x}\text{S}_x$ solid solution.....	87

Figure 35 Variation of the Poisson's ratio with S mole fraction for $c\text{-ZrO}_{2-x}\text{S}_x$ solid solution.....	88
Figure 36 Variation of the Young modulus with S mole fraction for $t\text{-ZrO}_{2-x}\text{S}_x$ solid solution.....	89
Figure 37 Variation of the Poisson's ratio with S mole fraction for $t\text{-ZrO}_{2-x}\text{S}_x$ solid solution.....	90
Figure 38 Variation of the young modulus with S mole fraction for $m\text{-ZrO}_{2-x}\text{S}_x$ solid solution.....	92
Figure 39 Variation of the Poisson's ratio with S mole fraction for $m\text{-ZrO}_{2-x}\text{S}_x$ solid solution.....	93
Figure 40 Variation of the bulk modulus, shear modulus and Pugh's ratio with S mole fraction for $(ctm)\text{-ZrO}_{2-x}\text{S}_x$ solid solution .....	95
Figure 41 Variation of anisotropic factor with S mole fraction for $c\text{-ZrO}_{2-x}\text{S}_x$ solid solution.....	97
Figure 42 Variation of Cauchy pressure with S mole fraction for $c\text{-ZrO}_{2-x}\text{S}_x$ solid solution.....	98
Figure 43 Variation of anisotropic factor with S mole fraction for $t\text{-ZrO}_{2-x}\text{S}_x$ solid solution.....	100
Figure 44 Variation of Cauchy pressures with S mole fraction for $t\text{-ZrO}_{2-x}\text{S}_x$ solid solution.....	101
Figure 45 Variation of anisotropic factor with S mole fraction for $m\text{-ZrO}_{2-x}\text{S}_x$ solid solution.....	103
Figure 46 Variation of anisotropic factor with S mole fraction for $m\text{-ZrO}_{2-x}\text{S}_x$ solid solution.....	104



# CHAPTER 1

## GENERAL INTRODUCTION

### 1. Background and aim of research

Zirconium dioxide (zirconia) is one of the most studied ceramic materials. Pure zirconia has four polymorphs, namely cubic, tetragonal, monoclinic, and orthorhombic zirconia. The latter forms only at elevated pressures. Zirconia can be modified by doping with other metal oxides such as magnesia and yttria. The tetragonal to monoclinic phase transformation significantly enhances the strength and toughness of partially stabilized zirconia [1], apart from doping with the metal oxides, addition of sulphur to  $ZrO_2$  has been concluded to be an alternative for stabilisation of cubic zirconia by partial replacement of oxygen by sulphur. Zirconia is a widely used ceramic in many technological applications. This is clearly attributed to its unique mechanical and chemical properties such as surface acidity and basicity, oxidation and reduction properties, porosity, stable surface area at high temperatures, high melting point, good mechanical strength, low thermal conductivity, and corrosion resistance [2].

Zirconia is used as an effective catalyst in many important reactions such as dehydration, elimination, hydrogenation, and oxidation reactions. Moreover, zirconia can be acidified to give a strong acid catalyst which can be effective in many reactions, such as alkene isomerization, hydrocracking, and alkylation [3]. Additionally, the cubic phase of zirconia also has a very low thermal conductivity, which has led to its use as a thermal barrier coating or TBC in jet- and diesel-engines to allow operation at higher temperatures [4]. Stabilized zirconia is used in oxygen sensors and fuel cell membranes because it has the ability to allow oxygen ions to move freely through the crystal structure at high temperatures. This high ionic conductivity (and a low electronic conductivity) makes it one of the most useful electro-ceramics. The high thermal stability and high ionic conductivity of zirconia make it a useful material for refractory purpose, in insulation, abrasives, enamels and ceramic glazes. And Zirconia has been recently considered in prosthetic dentistry for the fabrication of crowns and fixed partial dentures [5].

Biomass and solid oxide fuel cell (SOFC) are ones of the most promising auxiliary renewable energy sources. These systems offer highly efficient renewable energy and are modular in nature making them ideal for decentralised CHP (combined heat and power) applications and as a result have recently gained much attention [6, 7, 8].

As indicated in section 1.4, the studies of the effect of sulphur impurity on the structural properties of zirconia show the possibility of the partial replacement of oxygen atoms by sulphur atoms [9]. It is hypothesized that such replacement takes place in the ceramic part of the SOFC anode materials [10], and also after sulphidation at 623 K with H<sub>2</sub>S, around 1.8 wt% of sulphur was found on zirconia when sulphur-containing fuels (H<sub>2</sub>S or mixed H<sub>2</sub>/H<sub>2</sub>S) are used. Based on this hypothesis, the first-principles studies of the effect of sulphur impurity on the stability of *c*-ZrO<sub>2</sub>, *t*-ZrO<sub>2</sub> and *m*-ZrO<sub>2</sub> have been performed. However, in terms of practical applications, *c*-ZrO<sub>2-x</sub>S<sub>x</sub> solid solutions are more attracting. In this work the emphasis was made on the effect of sulphur on cubic zirconia.

The aim of our research is to create and study different structures of *c*-ZrO<sub>2-x</sub>S<sub>x</sub> (for *x* ranging from 0 to 2) using the Virtual Crystal Approximation (VCA) [11, 12]. The variations of ZrO<sub>2-x</sub>S<sub>x</sub> will eventually influence the properties *c*-ZrO<sub>2</sub> such as structural, electronic and mechanical properties. Furthermore, the purpose of this work is to study similar properties for *m*-ZrO<sub>2-x</sub>S<sub>x</sub> and *t*-ZrO<sub>2-x</sub>S<sub>x</sub> (for *x* ranges from 0 to 2) as for *c*-ZrO<sub>2-x</sub>S<sub>x</sub> using the VCA approach and compare the effects sulphur on *c*-ZrO<sub>2</sub> with the effect of sulphur on *t*-ZrO<sub>2</sub> and *m*-ZrO<sub>2</sub>.

### 1.1. Zirconium dioxide

Zirconium (IV) oxide is an extremely important oxide, and it has an extensive number of applications. It is used as a solid state electrolyte, in industrial and in the catalysis area. Furthermore, the extraordinarily high melting point and low thermal coefficient of expansion make it a major component of refractories. Another important reported application is that heated zirconia can be utilized as a source of infrared radiation and white light [13]. The high electrical resistance of the zirconia makes it an excellent oxide material for use as a ceramic insulator [14]. Table 1 summarizes the physical properties of the zirconium (IV) oxide.

**Table 1 Physical properties of zirconium oxide (ZrO<sub>2</sub>)**

Property	Value
Boiling point (°C)	4300
Coefficient of thermal expansion at -80 °C (cm/cm/°C)	8 x 10 <sup>-6</sup>
Colour	White
Density (mg/ml)	
Monoclinic	5.68
Tetragonal	6.10
Cubic	6.27
Entropy of formation at 298 K (Cal.)	- 46.5
Heat of formation at 298 K (Kg Cal./mol)	-261.5
Heat of fusion (Kg Cal./mol)	20.8
Formula weight (mg/ mol)	123.22
Melting point (°C)	2900
Solubility	
Soluble in	HF, Conc. H <sub>2</sub> SO <sub>4</sub> , molten glass
Insoluble in	Water, alkalis, organic solvents
Thermal conductivity at 100 °C (Cal. Sec/cm/cm <sup>2</sup> /°C)	0.004

## 1.2. Crystal structure of Zirconium oxide:

**Cubic phase:** Smith has identified the crystal structure of cubic zirconia [15]. The cubic phase is stable above 2370 °C to melting point. The cubic phase has a fluorite-type structure with a unit cell dimension of 5.27 Å. Each Zr<sup>4+</sup> ion is coordinated to eight oxygen atoms, while each oxygen atom is bonded to four zirconium atoms in a tetrahedral manner. Figures 1 show the structure of cubic zirconia [16].

**Monoclinic phase:** The crystal structure of the monoclinic phase is characterized by unit cell parameters of  $a = 5.169 \text{ \AA}$ ,  $b = 5.232 \text{ \AA}$ , and  $c = 5.341 \text{ \AA}$  with  $\beta = 99^\circ$ . The crystal structure of this phase demonstrates that the zirconium cations are seven-fold coordinated with oxygen. Oxygen coordinates nearly tetrahedrally to zirconium cations with one angle slightly larger than the tetrahedral angle (109.5°). Another



property of this structure is the existence of two alternative layers forming the seven-fold coordination.

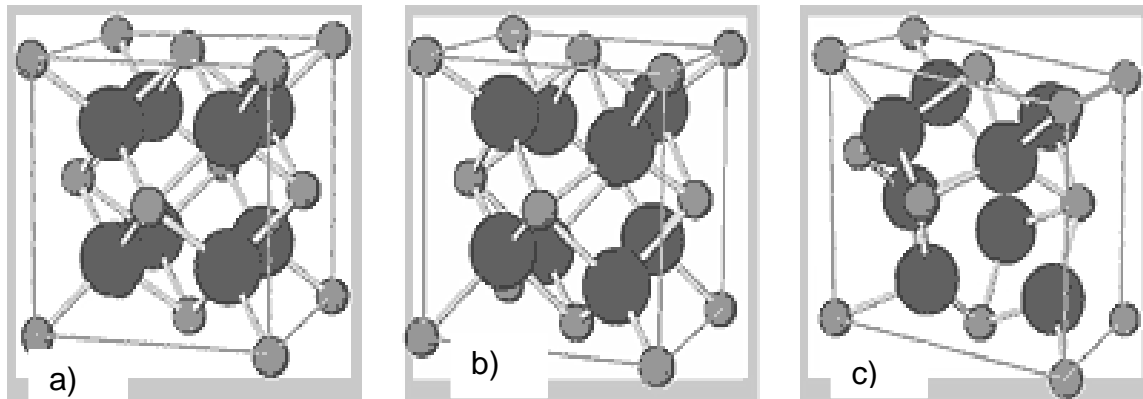


**Figure 1** Structural models of three polymorphic forms of  $ZrO_2$ , a) cubic, b) tetragonal and c) monoclinic crystal lattice.

Light sphere =Zr and dark sphere =O

The sevenfold coordination site of  $Zr^{4+}$  arises from the fact that there are two parallel oxygen layers present in the structure of the monoclinic zirconium oxide in which the zirconium atom layer is located between these oxygen layers parallel to the (100) planes.

**Table 2** Crystallographic data for cubic, tetragonal and monoclinic zirconia

$ZrO_2$	Space group, no	Cell parameter (Å)	Z	$V(Z=1)$ (Å <sup>3</sup> )	Atomic coordinates	Nearest Zr-Zr distances(Å)	Refs.
<i>c</i>	<i>Fm-3m, 225</i>	a=5.09	4	32.97	Zr:(0,0,0) O:(1/4,1/4,1/4)	3.599	[16]
<i>t</i>	<i>P42/nmc, 137</i>	a=3.591 c=5.169	2	33.33	Zr:(0,0,0) O:(0,1/2,0.204)	3.591 3.623	[15, 17]
<i>m</i>	<i>P21/c, 14</i>	a=5.1505 b=5.2116 c=5.3173	4	35.22	Zr1:(0.275, 0.0400, 0.208) O <sub>1</sub> :(0.070, 0.332, 0.345) O <sub>2</sub> :(0.445, 0.757, 0.489)	3.334 -4.301	[18]

The first layer is the  $Zr^{4+}$  coordinated to four oxygen atoms which form a square plane similar to half of an eight-fold cubic structure. In the second layer, the  $Zr^{4+}$  ion

is coordinated to the three other oxygen atoms which form a trigonal shape with the plane parallel to the phase of the first layer as shown in Figure 1. The monoclinic phase is stable at room temperature to about 1170 °C [18].

**Tetragonal phase:** The tetragonal phase is stable above 1170 °C and below the cubic range temperature of about 2370 °C. The tetragonal zirconia structure is very similar to the cubic structure with a slight difference. The former still maintains the eight-fold coordination of the zirconium cation. However, the bond distances between the zirconium ions and the four oxygen atoms is 2.45 Å, while the distances to the other four oxygen atoms is almost 0.4 Å difference, 2.065 Å [Figure 1] [15, 17].

### 1.3. Phase transformation:

Zirconia can exhibit phase transformation from one structure to another as a function of temperature and pressure as follows [1]:



The monoclinic–tetragonal phase transformation has been extensively studied due to its theoretical and practical importance. Upon phase transformation, the lattice parameters change, and zirconia undergoes contraction on heating and expansion on cooling through the transformation. X-ray diffraction analysis [19] has shown that the transformation does not occur at a fixed temperature, but the extent of transformation is changed with changing temperature. Previously, Wolten [20] has illustrated that the monoclinic-tetragonal transition is thermodynamically reversible and exhibits a large thermal hysteresis between cooling and heating cycles. Furthermore, the transformation rate is dependent upon the particle size of the zirconia powder. The larger the particle size of the prepared zirconia, the faster the phase transformation occurs. One of the major advantages of the monoclinic to tetragonal transformation is the volume contraction which can dramatically improve the fracture toughness and strength of zirconia ceramics [1]. However, the transformation from tetragonal to monoclinic is rapid and is accompanied by a 3 to 5 percent volume increase that causes extensive cracking in the material. This behaviour destroys the mechanical properties of fabricated components during cooling and makes pure zirconia useless for any structural or mechanical application. Several oxides, which dissolve in the zirconia crystal structure, can slow down or

eliminate these crystal structure changes. Commonly used effective additives are MgO, CaO, and Y<sub>2</sub>O<sub>3</sub> [21, 22, 23, 24, 25]. With sufficient amounts added, the high temperature cubic structure can be maintained to room temperature. Cubic stabilised zirconia is a useful refractory and technical ceramic material because it does not go through destructive phase transitions during heating and cooling.

A metastable tetragonal phase can be achieved at low temperatures using a variety of synthetic approaches. Garvie et al. [26, 27] attribute the low temperature stability of the tetragonal phase to the low surface energy of the tetragonal phase compared to that of the monoclinic phase. They claim that the critical size for stabilization of the tetragonal phase was 30 nm. When the crystallite size exceeds 30 nm, the material exhibits a transformation from the tetragonal phase to more the stable monoclinic phase. The controlled, stress-induced volume expansion of the tetragonal to monoclinic inversion is used to produce very high-strength, hard, tough varieties of zirconia for mechanical and structural applications. There are several different mechanisms that lead to strengthening and toughness in zirconia that contains tetragonal grains. While this is a complex subject matter, in principle, these depend on the grain sizes, the thermal history and the kind and amount of stabilising additive in the body. These variations lead to two strong, commercially available partially stabilised zirconia (PSZ) microstructures identified as tetragonally toughened zirconia (TTZ) and tetragonal zirconia polycrystal (TZP) ceramics [28, 29]. The TTZ is zirconia, partially stabilised with magnesium oxide (MgO) often designated MgTTZ or MgPSZ consisting of uniformly dispersed tetragonal precipitates in larger cubic phase crystals. The secondary thermal aging process requiring tight manufacturing controls for proper microstructural development has limited the supplier base for the tetragonally toughened zirconias. The second variety, TZP, is a pure tetragonal phase, very fine grain material, stabilised with rare earth oxides, primarily yttria and, less commonly, ceria. They are often designated YTZP for the yttria stabilised product and CeTZP for the ceria stabilised product. The TZP material has found uses in cutting and wear resistant applications due to its reliable and outstanding hardness and toughness. TZP properties degrade rapidly when the material is exposed to water vapour at 200 to 300°C, so controlled use conditions are important for good performance. All of the toughened zirconia show a degrading of properties

with increasing temperature, and this class of high strength, tough materials is generally limited to use at temperatures below 800°C [21, 22, 23, 26, 28, 29].

Additionally, the presence of water, upon calcination, was found to increase the rate of aggregation to form large particles and enhance the transformation [30]. This is also probably attributed to the lowering of the monoclinic surface energy as a result of water adsorption. Morgan [31], however, has prepared a monoclinic zirconia with a crystallite size smaller than 30 nm. This contradiction raises the question whether the tetragonal phase or a metastable phase is the more stable one. Addition of sulphate anions can also play an important role in phase transformation. Bridging sulphate ions stabilize the structure of zirconia since they can retard the formation of oxo-bonds between zirconium atoms and oxygen atoms. This will prevent sintering at high temperature, and hence, prevent rapid phase transformation and will stabilize the surface area [32, 33]. Furthermore, bridging sulphate groups are believed to contribute to thermal stabilization by increasing of the Zr-O-Zr separation from 3.4 Å to about 4.3 Å [32, 33, 34]. There are, in fact, other factors which also influence the phase transformation such as the precursor, pH, and aging time [35, 36]. Srinivasan, et al. [35] precipitated zirconia at different pH values within the range 3-13. The samples were calcined at 500 °C for different periods of time. They found that the sample precipitated at low pH exhibited fast phase transition from the tetragonal form to the monoclinic one. Furthermore, the phase transformation occurred more rapidly in an oxygen environment than in an inert gas atmosphere. The role of oxygen adsorption is believed to be as follows: the oxygen creates defect sites which generate more strains and dislocations sites which, in turn, initiate the phase transformation [3]. In case of sol-gel synthesis, the transition amorphous phase metastable crystalline ZrO<sub>2</sub> occurs at the temperature much lower than the equilibrium phase diagram states. The region of stability of the metastable polymorphs depends on the size of crystallites, the dispersity of final powder, hydrostatic stresses, the presence of impurities in structure, etc. As they all are deeply interconnected, so far it is not possible to distinguish the one which is the most dramatic. Hence, there is no common theory describing the occurrence and further thermal evolution of pure metastable zirconia and its solid solutions. At the same time, the proper choice of precursor synthesis conditions allows to control the size of crystallites, the specific area, grain size in the final ceramics, i.e. allows the direct crystallization of metastable phases [37].

#### 1.4. *c*-ZrO<sub>2</sub> and sulphur contact in biomass gasification

In gasification gas clean-up, zirconia and some doped forms of zirconia have been concluded to be selective catalysts for tar and ammonia oxidation [38, 39]. As we know, ZrO<sub>2</sub> is a metal oxide with acidic, basic, oxidizing and reducing properties [40] and with three stable crystal structures: cubic, tetragonal and monoclinic [41]. The characteristics of ZrO<sub>2</sub> based catalysts can be influenced by dopants which modify the basic, acidic surface properties and thermal stability of ZrO<sub>2</sub>. Some dopants, such as Y<sub>2</sub>O<sub>3</sub>, can create oxygen vacancies in the ZrO<sub>2</sub> anion lattice and stabilize ZrO<sub>2</sub> to tetragonal or cubic structure [41] whereas other dopants, such as SiO<sub>2</sub>, are not expected to create oxygen vacancies [42, 43] but enhance the thermal stability by restricting the growth of ZrO<sub>2</sub> particles. One of the problems in the use of catalysts is the fact that the biomass gasification gas contains usually remarkable amounts of H<sub>2</sub>S (in the range of 100 to even 500 ppm depending on the feedstock) [44]. For this reason, the sulphur tolerance of the catalyst is very important [44]. Nevertheless, Juutilainen et al. [38] say that H<sub>2</sub>S has little effect on the alumina doped zirconia catalyst and that the adsorption of H<sub>2</sub>S on the alumina doped zirconia is weak under the synthetic gasification gas conditions. In general, three possible sulphidation pathways on metal oxides with H<sub>2</sub>S are suggested: (1) exchange of oxygen from metal oxide to sulphur, (2) dissociation of H<sub>2</sub>S into HS<sup>-</sup> and H<sup>+</sup>, the latter forming hydroxyl-groups on the catalysts surface and (3) coordinative bonded hydrogen-sulphide which can be the source of Brønsted acidity [45]. According to Ziolk et al. [46] after sulphidation at 623 K with H<sub>2</sub>S, around 1.8 wt% of sulphur was found on zirconia. The H<sub>2</sub>S was observed to be dissociatively adsorbed and the surface oxygen ions could be replaced by sulphur. It was concluded that the replacement of oxygen by sulphur ions upon H<sub>2</sub>S adsorption seemed to increase the basicity or redox properties. Moreover, the selectivity to acetone in isopropanol decomposition was increased after sulphidation [46].

#### 1.5. Comparison of ZrO<sub>2</sub>, ZrOS and ZrS<sub>2</sub>

Zirconium has nearly equal energy of the 4d and 5s levels, and this allows most of the zirconium chemistry to involve the four electrons in these two levels. The Zr<sup>4+</sup> is a highly charged ion with a relatively large radius (0.86 Å). The Zr(IV) compounds exhibit high coordination numbers because Zr(IV) does not have a partially filled shell. Therefore, Zr(IV) does not display a stable lower valence species. Solutions of

zirconium salts can exhibit many chemical reactions such as hydrolysis, polymerization and hydration, depending on conditions. Zirconium salts dissociate in water at low pH value. For example,  $Zr^{4+}$  ions hydrate with bonding to eight water molecules to form a square antiprism [47].

Metal oxides and metal sulphides as  $ZrO_2$  and zirconium sulphide ( $ZrS_2$ ) have different structures and different properties even though the oxygen and sulphur belong to the same group in the periodic table. Because sulphur is directly below oxygen in the periodic table, these elements have similar electron configurations. As a result, sulphur forms many compounds that are analogues of oxygen compounds. There are four principal differences between the chemistry of sulphur and oxygen.

1. O=O double bonds are much stronger than S=S double bonds.
2. S-S single bonds are almost twice as strong as O-O single bonds.
3. Sulphur ( $EN = 2.58$ ) is much less electronegative than oxygen ( $EN = 3.44$ ).
4. Sulphur can expand its valence shell to hold more than eight electrons, but oxygen cannot.

These seemingly minor differences have important consequences for the chemistry of these elements [48].

It is well known that sulphur is larger in size, less electronegative, and the d-orbitals of sulphur are available for bonding [48]. Therefore, it will be very interesting to study the behaviour of the Zr-O-S system which contains both oxygen and sulphur, and to compare it with insulating  $ZrO_2$  systems and semiconducting  $ZrS_2$  systems.

The zirconium disulfide compound is crystallized in a lattice of  $CdI_2$  type with the space group  $D_{3d}^3(P3ml)$ . The lattice parameters are  $a=3.662 \text{ \AA}$  and  $c=5.813 \text{ \AA}$  [49]. The primitive Bravais cell contains one formula unit ( $z=1$ ). The anions take 2(d) = (1/3, 2/3, z) Wyckoff positions in the lattice and the cations take the common 1(a) = (0, 0, 0) positions. In this structure, one zirconium plane is sandwiched by two sulfur planes and the stacking of the layers forms the crystal structure, i.e. (S-Zr-S)(S-Zr-S). In this compound every zirconium atom is located in a slightly distorted octahedron composed of six sulphur atoms.

The ZrOS system contains both oxygen and sulphur; it has a simple cubic lattice with  $a=5.696$  with space-group  $T4-p213$ . The Zr shows the coordination number of seven, being surrounded by three sulphur atoms at  $2.63 \text{ \AA}$ , one sulphur atom at  $2.61 \text{ \AA}$  and three oxygen atoms at  $2.13 \text{ \AA}$ . The co-ordination polyhedron has a point-group symmetry of  $C3\sim 3m$  [50].

**Table 3 Crystallographic data for zirconium disulphide and zirconiumoxysulphide**

	Space group,no	Cell parameter ( $\text{\AA}$ )	Z	$V(Z=1)$ ( $\text{\AA}^3$ )	Atomic coordinates ( $\text{\AA}$ )	Nearest Zr-Zr distances( $\text{\AA}$ )	Refs.
ZrS <sub>2</sub>	$p-3m1,164$	$a=3.680$ $c=5.850$	1	68.61	Zr:(0,0,0) S:(1/3,1/3,1/4)	3.662	[49]
ZrOS	$T4-P213$	$a=5.696$	4	46.20	Zr(0.057) O(0.678) S(0.322)	3.650	[50]

### 1.6. Background on methodology and properties to be investigated

Current experimental data does not provide a detailed fundamental understanding of S solubility in ZrO<sub>2</sub>. In order to fill this gap of knowledge, atomistic simulation is a suitable approach. Despite the great technological importance of this system, few theoretical studies by first principle theory have been carried out to understand the solubility of S in ZrO<sub>2</sub>. But there have been some investigations of effect of sulphur impurities on the stability of *c*-ZrO<sub>2</sub> and its interface with metals (Malyi et al. [51] and on the stabilisation of *c*-ZrO<sub>2</sub> by partial exchange of oxygen and sulphur (Anderson et al. [52])). To the best of our knowledge only sulphur has an effect on stability. *c*-ZrO<sub>2</sub> has been the subject of study using first principle theory. It should be pointed out that these theoretical studies have provided valuable complementary information to experimental findings.

The use of computer simulation techniques is becoming more important in the understanding of the physical properties of materials. Steadily growing computer power and improvements in numerical algorithms are making more materials problems approachable by computer simulations. First principles computations, in which properties of materials are derived from quantum mechanics, are particularly

interesting because they allow for the exploration of new materials even before a procedure to synthesize them has been devised [53, 54]. First principle calculations based on Density Functional Theory (DFT) [55] have become a tool for investigations of solid material properties, as they provide the possibility to consider interactions between atoms from a chemical point of view.

The application of first principle electronic band structure methods to the study of disordered alloys and solid solutions requires some approximation for the treatment of the alloy disorder. A direct approach is to use the supercell approximation [56], to study one or more configurations in a supercell with artificially imposed periodic boundary conditions. Such calculations generally require the use of very large supercells in order to mimic the distribution of local chemical environments, and tend to be computationally very demanding. A much simpler and computationally less expensive approach is to employ the Virtual Crystal Approximation (VCA) [57], in which one studies a crystal with primitive periodicity, but composed of fictitious virtual atoms that interpolate between the behaviour of the atoms of the parent compounds. This approach has seen a wide use in band structure calculations. Another possible approach would be to make use of the coherent potential approximation (CPA) [58], but unfortunately the CPA is generally not well suited for use in first principles total-energy methods. Clearly, the VCA has the advantage of simplicity and computational efficiency.

The structural properties, electronic structures and stability of  $ZrO_2$  as a function of sulfur content was investigated by using first-principles calculations, implemented as Density Functional Theory (DFT) under the Born-Oppenheimer approximation, and this approach has been utilized in many of the systems, and has produced accurate ground state energies [55]. In recent years, first principles calculation has been gradually extended to complex systems such as doped systems, solid solutions and superlattices, and low-dimensional systems such as solid surface, nanotubes, quantum wells and quantum dots.

Some of the properties including heats of formation, cohesive energy, formation enthalpy, elastic properties and the density of states will be reviewed below as they are appropriate for the current study.



### 1.6.1. Heats of formation, formation enthalpy and cohesive energy

It has become quite commonplace, for electronic structural calculations of varying rigor, to yield the total energy of a solid. This offers a prospect of estimating the stabilities of structures which are either unavailable or inaccessible experimentally and this, in turn, has implications for making structural stability predictions. Heats of formation and cohesive energy from ab-initio calculations have been successfully used to predict the structural stability of alloys and solid solutions [59, 60, 61, 62]. In this work we will use the heats of formation and cohesive energy to predict the stability of all phases  $ZrO_{2-x}S_x$  for different x values.

### 1.6.2. Elastic Constants

*Ab-initio* calculations for the determination of elastic constants are more complex than the calculations of bulk properties (i.e. lattice constants, heats of formation, etc.). They provide a link between mechanical and dynamical behaviour of crystals, and give important information concerning the nature of forces operating in solids. In particular they provide information on the stability and stiffness of materials. The application of strain on the lattice implies a lowering of symmetry from that of bulk crystal and the strain energy involved is small.

In other work Nikiforov et al. report the elasticity moduli of  $Cd_xHg_{1-x}Te$  solid solutions [63], for which several researchers had done calculations [64, 65, 66]. The problem of ductile versus brittle response of crystals requires the fracture strength in addition to their deformability. Pugh [67] introduced the quotient of bulk modulus to shear modulus,  $B/C'$  as an indication of the extent of fracture range in metals. A high value of  $B/G$  is associated with ductility and a low value with brittleness. In this study we note that the lowest heat of formation is associated with ductility whereas the highest value is associated with the brittleness of the structure. This stipulates the relationship between the heat of formations and the elastic constants in terms of stability.

### 1.6.3. Electronic density of states and electron charge density difference

Similarly the heat of formation, cohesive energy, formation energy, elastic constants and the density of states (DOS) can be used to predict the stability of a solid solution. There is experimental and theoretical evidence that links the electronic structure to the stability of  $ZrO_2$ . This can be observed where the Fermi level lies in

the pseudo-gap of the density of states plot. Density of states and electron charge density of different states are directly linked to the conduction properties of a material. Hou et al. [68] have investigated the electronic structures of  $(\text{Li}_{1-x}\text{Me}_x)\text{FePO}_4$  (Me=Na and Be); some studies also investigated the electronic structures of solids solutions.

### 1.7. Objectives

In this thesis we investigate  $\text{ZrO}_{2-x}\text{S}_x$ , in particular the *c*- $\text{ZrO}_2$  structures as a function of sulphur content using Density Functional Theory (DFT).

We will determine the equilibrium lattice parameters, cell volumes and the heats of formation of the *c*- $\text{ZrO}_{2-x}\text{S}_x$ , *t*- $\text{ZrO}_{2-x}\text{S}_x$  and *m*- $\text{ZrO}_{2-x}\text{S}_x$ . The results will be compared with the available theoretical and experimental data in order to validate the methodologies employed in the current study. We will investigate the stability of the structures at that composition and deduce the most stable structure by comparing their heats of formation and cohesive energy.

In this work we will also perform the calculation of elastic and electronic properties of the *c*- $\text{ZrO}_{2-x}\text{S}_x$  and compare the results with the available experimental and theoretical results. Additionally we will investigate similar properties for *t*- $\text{ZrO}_{2-x}\text{S}_x$  and *m*- $\text{ZrO}_{2-x}\text{S}_x$  structures for selected compositions and observe how the structural stabilities change. A detailed comparison of the calculated results will be presented.

## CHAPTER 2

### THEORETICAL TECHNIQUES

#### 2. *Ab initio* methods

*Ab initio* methods, such as Hartree-Fock or Density Functional Theory (DFT) calculate the electronic structure from first principles, i.e. without the need for empirical fitting parameters. In general, these methods utilize a variational approach to calculate the ground state energy of a many-body system, where the system is defined at the atomic level. The original calculations were performed on systems containing a few atoms. Today, calculations are performed using approximately up to 1000 atoms but they are computationally expensive, sometimes requiring massively parallel computers.

Density Functional theory gives a quantum-mechanical basis for most of the *ab initio* methods used in computational materials science [69]. These methods have made it possible to study complex solid materials of great industrial relevance. The main aims of these applications are the atomic level understanding of the properties and prediction of new data for the development of high-performance materials. In order to accomplish these goals, the numerical methods for solving the single-electron equations should have sufficient accuracy and efficiency. In this chapter, we shall start with a short summary of the Density Functional Theory and the Kohn-Sham scheme and also briefly review the most important approximations within the Density Functional Theory, and the most widely used methods for ordered as well as for disordered systems.

#### 2.1. Electron density instead of the wavefunction

Density functional theory (DFT) has been playing increasingly important roles in many research activities of science and engineering in recent decades and has already become a mainstay for the quantum mechanical investigations of a broad range of complex molecular systems that are of interest in chemistry, biology, and physics [70, 71, 72]. DFT offers viable computational protocols with a good balance between accuracy and computational cost. This feature is particularly useful when one intends to investigate large molecular systems, to which the application of

accurate *ab initio* methods may be difficult or even impossible. The availability of user-friendly software packages greatly assists in applying DFT calculations to individual specific problems.

In DFT, electronic energy  $E$  is expressed as a functional of electron density, viz.,

$$\begin{aligned} E &= \rho(r) \\ &= T[\rho(r)] + V_{ne}[\rho(r)] + V_{ee}[\rho(r)] \end{aligned} \quad 2.1.$$

where  $T$  is the total kinetic energy of electrons,  $V_{ne}$  the potential energy resulting from an external potential and  $V_{ee}$  the electron–electron repulsion energy. Electron density  $\rho(r)$  for an  $N$ -electron system is defined as

$$\rho(r) = N \int |\Psi(\vec{x}_1, \vec{x}_2, \dots, \vec{x}_N; \vec{R}_1, \dots, \vec{R}_{Nn})|^2 d\sigma_1 d\vec{x}_2 \dots d\vec{x}_N \quad 2.2.$$

where  $x_i$  collectively denote spatial ( $R_i$ ) and spin ( $s_i$ ) coordinates. In stark contrast to the wave function  $\Psi$  that depends on  $3 \times N$  (space) +  $N$  (spin) =  $4N$  variables,  $\rho(r)$  contains only three spatial variables, implying that  $E$  may be obtained in a much more straightforward manner using  $\rho(r)$ . In 1964, Hohenberg and Kohn proved that there is a one-to-one correspondence between the ground-state density and the external potential [73]. They also showed that the variational principle holds for the ground-state energy. The variational principle and the Levy constrained-search formulation of DFT [74] ensure that  $E$  can be determined by minimizing it with respect to some  $N$ -representable trial electron densities.

Despite the fundamental importance of the Hohenberg–Kohn theorems, they do not provide explicit forms of the energy functionals in Equation 2.1 (except  $V_{ne}$ ). To

proceed, one needs to know how  $T$  and  $V_{ee}$  are expressed as functionals of  $\rho(r)$ . A practical approach to this problem was proposed by [75]. Their approach attempts to describe the real electron density by way of non-interacting electrons that are described using a Slater determinant of molecular orbitals (MOs) [or Kohn–Sham (KS) orbitals]. When the density is treated this way, the total energy is written as

$$E[\rho(r)] = T_s[\rho(r)] + V_{ne}[\rho(r)] + J[\rho(r)] + E_{xc}[\rho(r)] \quad 2.3.$$

where  $T_s[\rho(r)]$  is the kinetic energy of non-interacting electrons,  $J[\rho(r)]$  the classical electron-electron repulsion energy (Hartree energy), and  $E_{xc}[\rho(r)]$  the exchange-correlation energy. The first term  $T_s[\rho(r)]$ , which accounts for a large portion of  $T[\rho(r)]$ , may now be calculated using KS orbitals as in Hartree–Fock calculations.

Nevertheless the explicit form of  $E_{xc}[\rho(r)]$  remains unknown. In practice, KS equations are solved by employing an approximate  $E_{xc}[\rho(r)]$ ; as such, the accuracy of DFT energy depends critically on the quality of  $E_{xc}[\rho(r)]$ . So far, a number of exchange-correlation functionals have been developed, by either constraint satisfaction or semi empirical fitting [76].

DFT describes the electronic states of atoms, molecules, and material in terms of the three-dimensional electronic density of the system, which is the great simplification over wavefunction theory. DFT is based on a concept of the Thomas-Fermi-Dirac theory that introduced the idea of expressing the total energy of the system a function of total electron density. As seen in figure 2.

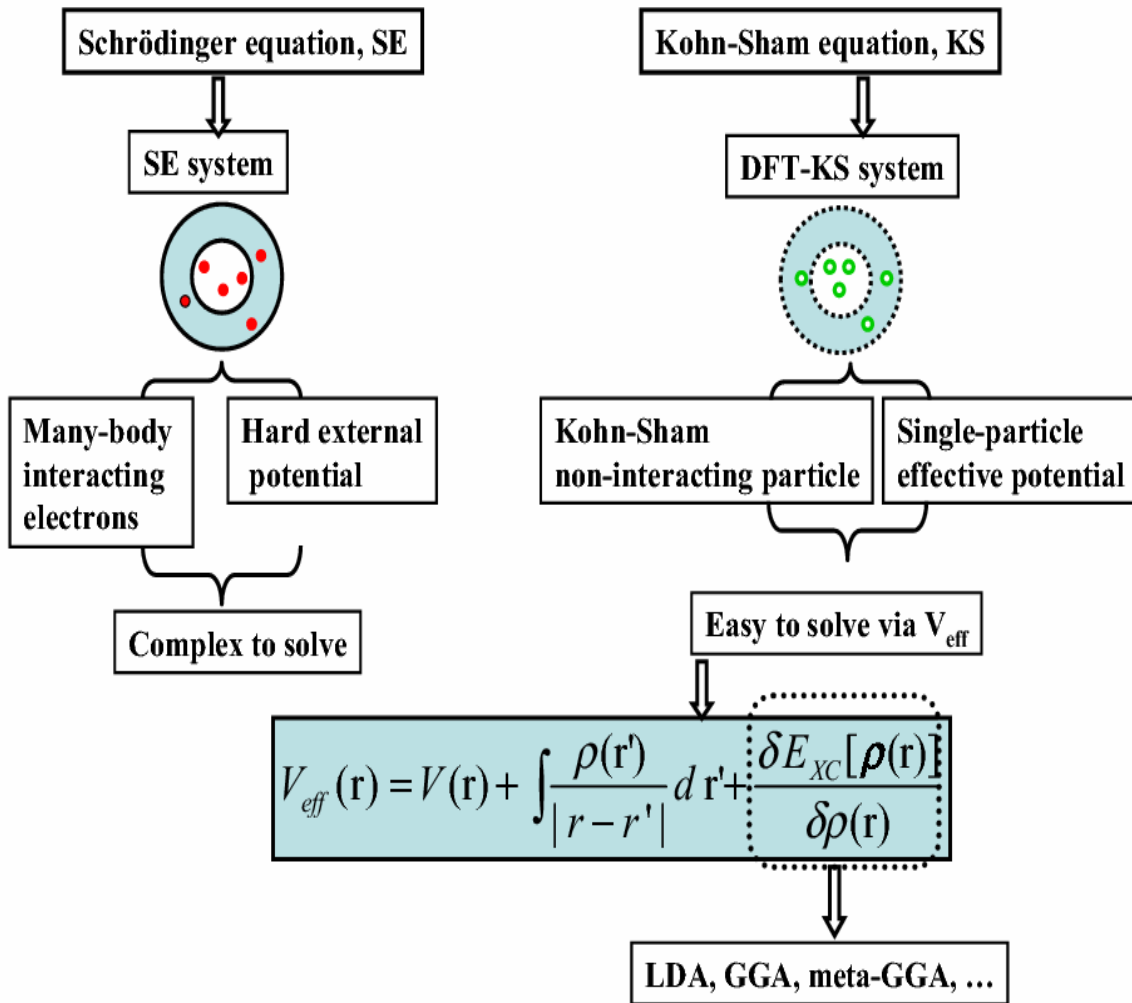


**Figure 2 A comparison of the methodology for solving the many-body Schrödinger equation and effective one-electron Kohn-Sham equation [77].**

## 2.2. Crystals and Unit Cells

In our case we will be working on periodic system and the method that we will be using deals with periodic systems. In the solid state, most materials like to have their atoms arranged in some kind of regular, repeating pattern.

If the nuclei are arranged in a periodically repeating pattern, their potential acting on the electrons must also be periodic. i.e

$$V(\mathbf{r} + \mathbf{L}) = V(\mathbf{r})$$

where  $\mathbf{L}$  is any lattice vector.

If the potential is periodic, then so is the density:

$$\rho(r + L) = \rho(r)$$

$$\rho(r) = |\psi(r)|^2 \text{ as also indicated in equation 2.1 and 2.2.}$$

### 2.3. Approximations for the Exchange-Correlation Functional

$E_{XC}$  functionals are classified into the following five major levels (rungs) of “Jacob's Ladder” according to their types: namely, local spin density approximation (LSDA), generalized gradient approximation (GGA), meta-GGA, hyper-GGA, and generalized random phase approximation [78]. In the field of chemistry, Gaussian- or Slater-type atomic orbitals (AOs) are usually used as basis sets of KS orbitals, while GGA, meta-GGA, or hyper-GGA functionals are mainly used to approximate  $E_{XC}$ . When KS equations are solved for periodic solids or nanomaterials, plane-wave basis sets and pseudopotentials are used often with LSDA or GGA functionals.

#### 2.3.1. Local Density Approximation (LDA)

The simplest approximation that one can make is to imagine that at every point in space we can use the value of the density that the uniform electron gas would have at that point, and allow it to vary from point to point. This is called the Local Density Approximation (LDA). In more detail, we write:

$$E_{xc}^{LDA}[\rho] = \int \rho(\vec{r}) \varepsilon_{xc}(\rho(\vec{r})) d\vec{r} \quad 2.4.$$

$$\varepsilon_{xc}(\rho(\vec{r})) = \varepsilon_x(\rho(\vec{r})) + \varepsilon_c(\rho(\vec{r})) \quad 2.5.$$

where

$$\varepsilon_x(\rho(\vec{r})) = -\frac{3}{4} \left( \frac{3\rho(\vec{r})}{\pi} \right)^{1/3} \quad 2.6.$$

is the Dirac-Slater Exchange Energy of the electron gas. The Coulomb correlation piece is obtained from interpolations of Monte Carlo data by Ceperly and Alder (1980). The typical LDA approximation is the SWVN implementation that implies Slater Exchange plus Coulomb Correlation obtained by Vosko, Wilk and Nussair (1980). Perdew and Wang (1992) made a more accurate implementation [79, 80, 81, 82].

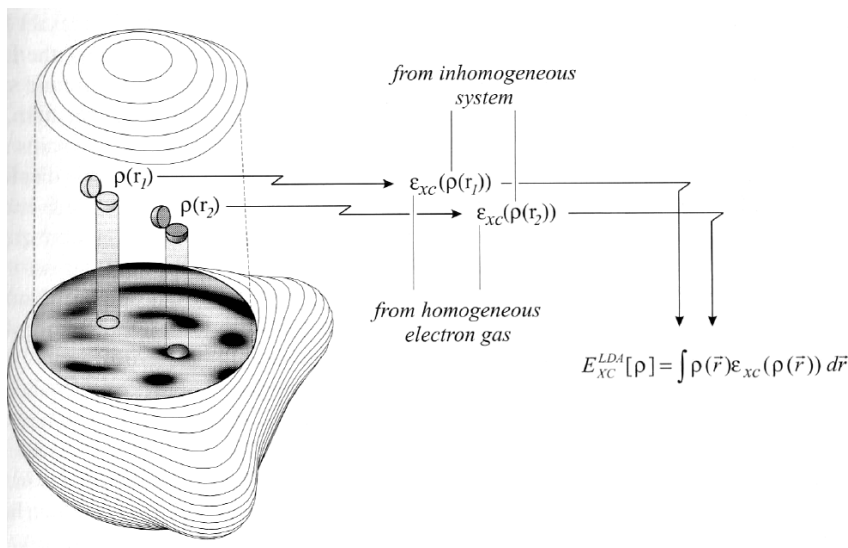


**Figure 3 Schematic of the LDA (Koch & Holthausen) [83].**

This approximation was found to reproduce the ground-state properties of many systems with surprising high accuracy. In particular, the bulk properties of 4d and 5d transitions metals, oxides and others or the surface properties of metals [84], are very well described by within LDA.

They are situations where LDA turns out to be inappropriate even for a qualitative description. During the last decades several more accurate exchange correlation density functionals have become available. LDA are important in the construction of more sophisticated approximations to the exchange-correlation energy, such as generalized gradient approximations or hybrid functionals.



### 2.3.2. Generalized Gradient Approximation (GGA)

The LDA by its self does not contain sufficient accuracy for chemical applications. It is necessary to include terms that explicitly take into account the spatial variation of the density. This formulation of functionals within the Generalized Gradient Approximation (GGA) is what made good accuracy density functional theory possible. As above, approximations are made separately for the Exchange and Coulomb portions.

The Coulomb expressions are quite complex and we will skip writing them down. The popular choices are:

LYP: Lee, Parr & Yang (1988)

PW91: Perdew & Wang (1991)

P86: Perdew (1986)

These can be combined with Exchange-Correlation Functionals. These have the form,

$$E_x^{CGA} = E_x^{LDA} - \sum_{\sigma} F(s_{\sigma}) \rho_{\sigma}^{4/3}(\vec{r}) d\vec{r} \quad 2.7.$$

$$s_{\sigma} = \frac{|\nabla \rho|}{\rho_{\sigma}^{4/3}} \quad 2.8.$$

Two commonly used choices for the Exchange functional are:

Becke (1988):

$$F^B = \frac{\beta s_{\sigma}}{1 + 6\beta s_{\sigma} \text{Sinh}^{-1}(s_{\sigma})} \quad 2.9.$$

Perdew (1986) :

$$F^{86} = \left(1 + 1.296x^2 + 14x^4 + 0.2x^6\right)^{1/15} \quad 2.10.$$

$$x = \frac{s_{\sigma}}{(24\pi^2)^{1/3}} \quad 2.11.$$

The b parameter in the Becke form is fit to accurate densities of a large number of atoms, while that of Perdew does not have any empirical parameters. Typical combinations in common use give rise to the functionals:

Becke & Perdew/Wang: BPW91

Becke & Lee/Parr/Yang: BLYP

These functionals are all LOCAL in the mathematical sense, but go beyond the Local Density Approximation [84, 85, 86, 87, 88, 89, 90].

### 2.3.3. Hybrid Functionals

It should be clear that the HF method has a systematic error. The lack of Coulomb correlation implies that the energies are higher than they should be as charges are allowed to get closer to each other than they should be, thus the bond lengths tend to be smaller and the binding energies larger than experiment. In DFT, on the other hand, the systematic errors occur in precisely the opposite direction. Thus a combination of the HF Exchange and the functional exchange should improve things considerably. The popular B3LYP functional is the prime example of this kind. The performance is excellent, with an RMS error of about 2 kcal/mol on the large G2 molecule reference set. This functional has the form:

$$E_{xc}^{B3LYP} = (1-a)E_x^{LSD} + aE_{xc}^{\lambda=0} + bE_c^{B88} + cE_c^{LYP} + (1-c)E_c^{LSD} \quad 2.12.$$

The parameters  $a$ ,  $b$  and  $c$  control the relative amounts of HF-Exchange and Coulomb Correlation from the various sources and they are determined empirically (by fitting to data).

#### **2.4. DFT as implemented in codes**

In this thesis the plane wave DFT calculations are performed using CASTEP (Cambridge Sequential Total Energy Package). CASTEP is commercially available software from Accelrys developed by Payne and co-workers [91]. The electron-core interaction is described by ultrasoft pseudopotentials proposed by Vanderbilt (see Section 2.5), while electronic wave functions are represented by a sum of plane waves. For electron density minimisation CASTEP applies a self-consistent field scheme. The most popular approximations for the exchange-correlation energy, *i.e.*, LDA and GGA with several different functionals, are implemented. CASTEP's foundations are briefly explained in the subsequent paragraphs.

CASTEP [91, 92] is an ab initio quantum mechanical program which employs density functional theory (DFT) to simulate the properties of solids, interfaces, and surfaces for a wide range of materials classes such as ceramics, semiconductors, and metals. CASTEP is developed in the Theory of Condensed Matter Group at Cambridge University, UK. It is a suite of programs that provides advanced quantum mechanical calculations for chemicals and materials research. CASTEP utilizes the total energy plane-wave pseudopotential method where ionic potentials are replaced with effective potentials which act only on the valence electrons in the system. Electronic wavefunctions are expanded through a plane-wave basis set and exchange and correlation effects in electron- electron interactions can be included within either the local density (LDA) or generalized gradient (GGA) approximations. Combining the use of pseudopotentials and plane wave basis sets makes it easier to calculate the forces on the atoms, enabling efficient optimization of ionic configurations of molecules, solids, surfaces, and interfaces. CASTEP takes the number and type of atoms in a system and predicts properties such as lattice constants, molecular geometry, elastic constants, band-structures, density-of-states, charge densities and wave functions, and optical properties.

#### **2.5. Planewave pseudopotential method**

In a solid, the KS-equations are easily dealt with in reciprocal space, where the differential eigenvalue problem is mapped onto algebraic linear system. The plane-

wave pseudopotential method for the Density Functional Theory (DFT) is a technique used to calculate the variation self-consistent solution with accuracy. This method has been advanced and perfected to reliably predict the static and dynamic properties of molecules and crystalline solids [93].

### 2.5.1. Planewaves and pseudopotentials

In the study of infinite solids it is necessary to exploit the crystal symmetry in order to circumvent the problem of infinite number of electronic degrees of freedom and, as a consequence, of an infinite number of linear equations. Bloch's theorem, which starts with periodicity of crystal lattice, can handle this problem; this property allows to map the problem onto a single cell, repeated in space through the so called periodic boundary conditions, having a small number of atoms and thus, electrons. The model system is constructed in 3D periodic supercell which allow Bloch's theorem to be applied to the electron wave function:

$$\psi_{n,k}(r) = u_{n,k}(r) \exp(ik \cdot r) \quad 2.13.$$

The function  $u(r)$  has the periodicity of supercell. It can be of any suitable mathematical form and usually one chooses a series expansion in terms of a set of basis function. In PW pseudopotential, planewaves are used for this expansion, so that each single-electron wavefunction  $\psi_{n,k}$  is written as

$$\psi_{n,k}(r) = \sum u_{n,k}(G) \exp(i(k + G) \cdot r) \quad 2.14.$$

Where  $k$  belongs to the first Brillouin zone of the crystal,  $G$  is a reciprocal lattice vector and  $n$  is the band index and the  $u_{n,k}$  are the expansion coefficients. The wavevectors  $G'$  are such that the planewaves are commensurate with the supercell. Both the number of  $G$ -vectors in the sum and the number of  $k$ 's considered should in principle be infinite. The exponential term is a planewaves of wavevector  $k$  which must be commensurate with the entire system (i.e. not just the periodically-replicated cell). For an infinite system there is an infinite number of  $k$  vectors, at each of which solutions for  $\psi_{n,k}$  exist. This simply reflects the fact that the number of electrons is infinite. However, a great simplification comes about when one realises that the

change in  $\psi_{n,k}$  with  $k$  becomes negligible for  $k$ -points that are close together. This means that one may calculate at a finite number of  $k$ -points. We speak of this idea as  $k$ -point sampling. The set of vectors  $\{G\}$ , on the other hand, should in principle be infinite to obtain an exact representation of the wavefunction. This is never necessary because summing over a finite number of  $G$ 's will yield sufficient accuracy. Planewaves basis set has many advantages:

- It is simple.
- All necessary matrix elements can be efficiently computed.
- The basis doesn't prefer one location over another, so there are no "Pulay forces".
- A single parameter controls convergence of the basis.

Its disadvantage is that:

- Non-localized basis functions are hard to parallelize efficiently.
- Cannot take advantage of vacuum to reduce the basis size.
- Representing atomic wavefunctions requires a prohibitively large number of planewaves

The advantages speak for themselves i.e the first three mean that one can always ensure that the basis set is adequate for a calculation by increasing the number of planewaves until the quantity of interest stops changing. In other words, the quality of the basis set depends on a single parameter, usually expressed as the energy of a free electron whose wavefunction has the same wavevector as the largest wavevector in the planewave basis,

$$E_c = \frac{\hbar^2(G+k)^2}{2m} \quad 2.15.$$

All planewaves of an energy less than the Cut-off energy  $E_c$  are used in the expansion. The mathematical simplicity of planewaves means the method is easier to implement, crucially so for the calculation of ionic forces which adds little complexity or cost to the calculation. Equally important in this context is the originless nature of planewaves. Their independence from atomic positions means that the forces do not depend on the basis set—there are no 'Pulay' or

'wavefunction' forces [94]. Even more important, new developments are easiest in planewave codes. An idea to calculate a property is most rapidly realised in a planewave basis and even if other methods catch up in time, the planewave approach remains as the reference. From a computational viewpoint the first of the disadvantages appears to be very serious.

### **2.5.2. Pseudopotential approximation**

The rapid oscillations of the wavefunctions near to the nucleus, due to the very strong potential in the region and the orthogonality condition between different states, mean that a very large Cut-off energy and hence basis set, would be necessary. Fortunately, the study of Physics and Chemistry shows that the core electrons on different atoms are almost independent of the environment surrounding the atom and that only the valence electrons participate strongly in interactions between atoms. Thus, the core electron states may be assumed to be fixed and a pseudopotential may be constructed for each atomic species which takes into account the effects of the nucleus and core electrons [95, 96, 97].

The pseudopotential approximation allows the electronic wavefunctions to be expanded using a much smaller number of planewave basis states. It is well known that most physical properties of solids are dependent on the valence electrons to a much greater extent than on the core electrons. The pseudopotential approximation exploits this by removing the core electrons and replacing the strong ionic potential by a weaker pseudopotential that acts on a set of pseudo-wavefunctions rather than the true valence wavefunctions. An ionic potential, valence wave function and corresponding pseudopotential and pseudo-wavefunction are illustrated in fig. 2.5. The valence wavefunctions oscillate rapidly in the region occupied by the core electrons due to the strong ionic potential in this region. These regions maintain the orthogonality between the core wavefunctions and the valence wavefunctions, which is required in the Pauli's exclusion principle.

The pseudopotential is constructed in such a way that its scattering properties or phase shifts for the pseudo wavefunctions are identical to the scattering properties of the ion and the core electrons for the valence wavefunctions, but in such a way that the pseudo-wavefunctions have no radial nodes in the core region. The phase shift

produced by the ion core is different for each angular momentum component of the valence wave function and so the scattering from the pseudopotential must be angular momentum dependent. The most general form for pseudopotential is

$$V_{NL} = \sum_{lm} |lm\rangle V_l \langle lm| \quad 2.16.$$

Where  $\langle lm|$  are the spherical harmonics and  $V_l$  is the pseudopotential for angular momentum  $l$ . Acting on the electronic wave function with this operator decomposes the wave function into the spherical harmonics, each of which is multiplied by the relevant pseudopotential  $V_l$ .

A pseudopotential that uses the same potential for all the angular momentum components of the wave function is called a local pseudopotential. A pseudopotential is a function only of the distance from the nucleus. It is possible to produce arbitrary, predetermined phase shifts for each angular momentum state with a local potential, but there are limits to the amount that the phase shifts can be adjusted for the different angular momentum states, while maintaining the crucial smoothness and weakness of the pseudopotential. Without a smooth, weak pseudopotential it becomes difficult to expand the wavefunctions using a reasonable number of planewaves basis states [98, 99, 100].

## 2.6. *k*-sampling

Electronic states are allowed only at a set of  $k$ -points determined by the boundary conditions that apply to the bulk solid. The density of allowed  $k$ -points is proportional to the volume of the solid. The infinite numbers of electrons in the solid are accounted for by an infinite number of  $k$ -points and only a finite number of electronic states are occupied at each  $k$ -point.

The Bloch theorem changes the problem of calculating an infinite number of electronic wavefunctions to one of calculating a finite number of  $k$ -points. The occupied states at each  $k$ -point contribute to the electronic potential in the bulk solid so that in principle an infinite number of calculations are needed to compute this potential. However the electronic wavefunctions at  $k$ -points that are very close are identical. Hence it is possible to represent the electronic wavefunctions over a region

of  $k$  space by the wavefunctions at the single  $k$ -point. In this case the electronic states at only a finite number of  $k$ -points are required to calculate the electronic potential and hence determine the total energy of the solid.

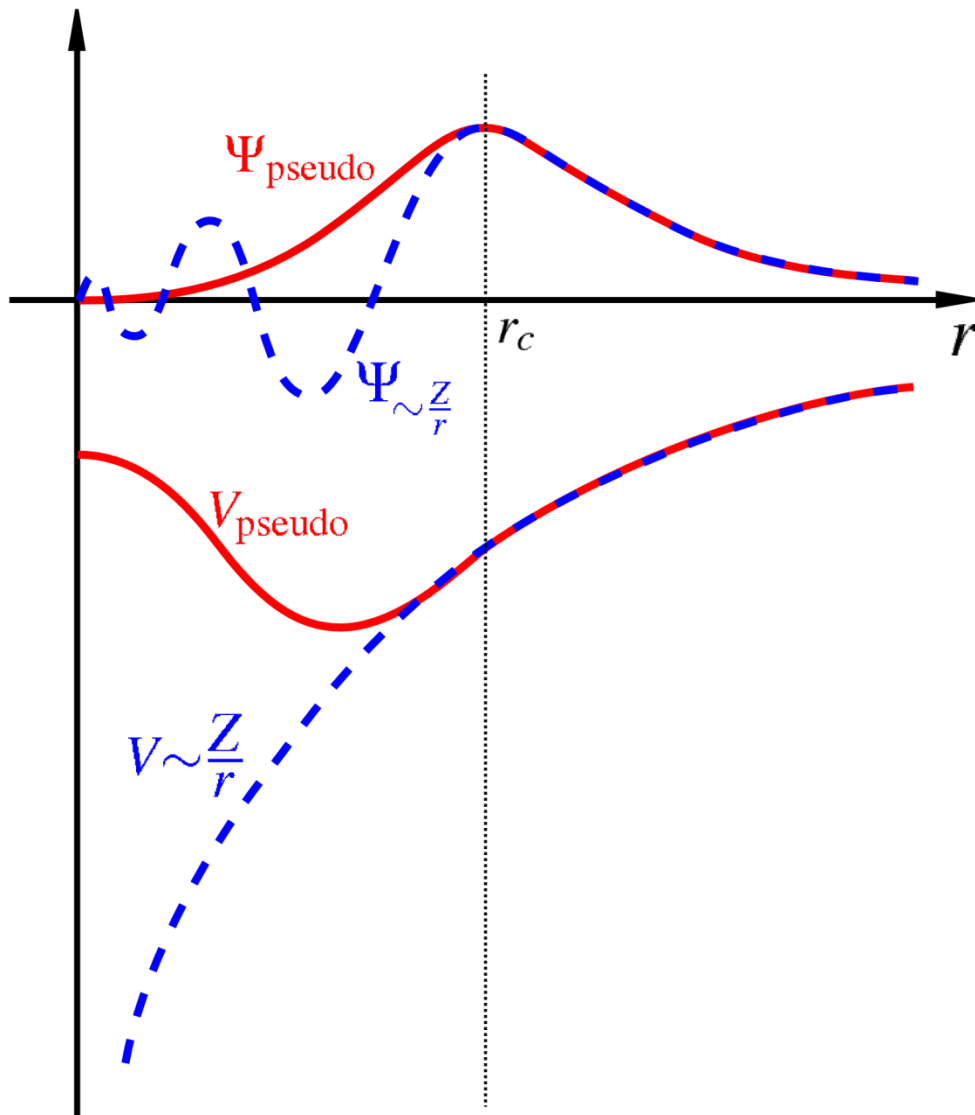


**Figure 4 Comparison of a wavefunction in the Coulomb potential of the nucleus (blue) to the one in the pseudopotential (red). The real and the pseudowavefunction and potentials match above a certain Cut-off.**

Methods have been devised for obtaining very accurate approximations to the electronic potential from a filled electronic band by calculating the electronic wavefunctions at special sets of  $k$ -points. The two most common methods are those



of Chadi and Cohen [97] and Monkhorst and Pack [101]. Using these methods, the electronic potential and the total energy of an insulator can be obtained by calculating the electronic states at a very small number of  $k$ -points. A denser set of  $k$ -points are required to calculate the electronic potential and the total energy of a metallic system in order to define the Fermi surface precisely.

However, the computational cost of performing a very dense sampling of  $k$  space increase linearly with the number of  $k$ -points in the Brillouin zone (BZ). Density functional codes approximate these  $k$  space integrals with a finite sampling of  $k$ -points. Special  $k$ -points schemes have been developed to use the fewest possible  $k$ -points for a given accuracy, thereby reducing the computational cost. The most commonly used scheme is that of Monkhorst and Pack.

### 2.7. Theoretical approach to the solid solution or alloys problem.

Through DFT it possible to calculate the ground-state energy of given microscopic configuration in a disordered system. This choice is however not of practical use: in the theoretical study of solid solution, one should consider several supercells containing thousands of atoms, in order to cope with disorder, and to take into account different configurations. For this reason, such direct approach has always been considered well beyond reachable numerical power. The typical approaches to the study of solid solution are based on approximations in which all the possible, inequivalent, microscopic configurations are averaged into an effective medium having the same crystal structure of the underlying lattice, in order to recover the translational symmetry. The simplest of this historical approach is so-called virtual crystal approximation (VCA) and coherent potential approximation (CPA).

#### **An efficient virtual crystal approximation approach for bulk solid solutions and alloys**

The material properties of solid solutions and alloys have been widely studied both experimentally and theoretically throughout material science. Especially ferroelectric ceramics correspond to a typical material class for which most of the realistic applications are implemented by solid solutions. To treat such material systems within first principles methods, there exist two ways: the supercell (SC) method and the VCA method. Firstly, it is necessary to mention the advantage and shortcoming of both methods. The former can give more correct results but requires more

computational resources compared with the latter. The issue of correctness is related with the fact that the SC method can describe the local interaction between two atoms, but the VCA method cannot do that. It is clear that the effectiveness of the calculation is connected with the fact that the supercell may contain many unit cells compared with the primitive unit-cell of the VCA method. In the year 2000, several modern VCA approaches were developed with their own advantages and shortcomings. Here mainly two issues are considered: capability of treating the heterovalent atoms and accuracy of the calculation. VCA originated from tight binding methods by replacing atoms with effective atoms and choosing the parameterization to return alloy properties. It works very well for some properties, not so well for others. The advantage is the simplicity but it is not sufficiently accurate in some cases. The reason of the incorrectness is mixing of only the potentials.

### 2.7.1. Ramer and Rappe VCA Approach

The reason of the incorrectness is mixing of only the potentials. Ramer and Rappe developed more accurate VCA approach through performing the averaging at the level of atomic calculation,

$$\varepsilon_l^{AVE} = (1-x)\varepsilon_{nl}^A + (x)\varepsilon_{nl}^B \quad 2.17.$$

where the averaging of eigenvalues of valence orbitals [102, 12], Coulomb nuclear potentials, core charge densities and wavefunctions are performed. The shortcoming of this method is not to be able to treat the heterovalent atoms; their method only creates the pseudopotential of the virtual atom composed of homovalent atoms.

### 2.7.2. Bellaiche and Vanderbilt VCA Approach

The weighted averaging method of Bellaiche and Vanderbilt [103] gives another capability to realize effective VCA approach.

$$V_{pseudo}^{site} = (1-x)V_{pseudo}^A + (x)V_{pseudo}^B$$

$$V_{ext} = \sum_j \sum_k^{sites\ species} W_k^j V_{pseudo}^k \quad 2.18.$$

$$z_{valence}^{site} = \sum_k^{species} w_k^{site} z_{valence}^k \quad 2.19.$$

Its advantages are the ability to treat heterovalent systems and generality to apply to all kinds of first principles pseudopotentials. However, this method can be considered also as a kind of simple mixing of pseudopotentials in the case of the norm-conserving types, though the additional averaging process is performed in the case of ultrasoft pseudopotential. Therefore, the resulting values in the case of complex heterovalent systems [11] show small deviation from the SC and the experimental values.

## 2.8. Numerical details and theory of properties to be investigated

### 2.8.1. Cohesive and formation energy

Cohesive energy ( $E_c$ ) can be considered as a measure of a structure's overall chemical stability. It is defined as the difference between a structure's total electronic energy and the sum of the electronic energies of its constituent atoms at infinite separation:

The cohesive (binding) of the pure elements and pseudo element or solid solution ( $ZrO_{2-x}S_x$ ) alloy was computed according to the relation [104, 105]

$$\Delta E = E_{ZrO_{2-x}S_x} - E_{Zr(atom)} - (2-x)E_{O(atom)} - xE_{S(atom)} \quad 2.20.$$

Where  $E_{ZrO_{2-x}S_x}$ ,  $E_{Zr(atom)}$ ,  $E_{O(atom)}$  and  $E_{S(atom)}$  are the total energies of  $ZrO_{2-x}S_x$ , O and S atoms, respectively. The fractions indicate the total number of atoms of constituent species in the unit cell, usually referred to as fractional composition. The energy of a free atom is calculated by creating a P1 supercell with lattice parameter  $a=20 \text{ \AA}$ ,  $b=19 \text{ \AA}$  and  $c=18 \text{ \AA}$  and placing an atom at the centre.

The heats of formation of compounds and associated entropies provide the basis for understanding and constructing phase diagrams. Knowledge of these quantities offers the prospect of disentangling which of the observed phases might occur upon varying the means of fabrication. Such modeling of alloy phase behavior is of considerable technological relevance. The heat of formation can be estimated by

$$\Delta H = E_{\text{ZrO}_{2-x}\text{S}_x} - E_{\text{Zr}(\text{crystal})} - (2-x)E_{\text{O}(\text{crystal})} - xE_{\text{S}(\text{crystal})} \quad 2.21.$$

where  $E_{\text{ZrO}_{2-x}\text{S}_x}$ ,  $E_{\text{Zr}(\text{crystal})}$ ,  $E_{\text{O}(\text{crystal})}$  and  $E_{\text{S}(\text{crystal})}$  are the total energies of  $\text{ZrO}_{2-x}\text{S}_x$ , Zr, O and S at their most stable states, respectively.

The fractional (atomic) composition of element O and S is represented by  $x$ . It thus follows from the above expressions (2.20) and (2.21), that the formation energy depends on the cohesive energy of materials. The negative formation energy indicates that the reaction from pure elements to produce the final compounds is possible and negative cohesive energy means that the final compounds are energetically stable.

## 2.8.2. Elastic properties

### 2.8.2.1. Theory of elasticity

From the perspective of materials physics, the elastic constants  $C_{ij}$  contain some of the more important information that can be obtained from ground-state total-energy calculations. A given crystal structure cannot exist in a stable or metastable phase unless its elastic constants obey certain relationships. The  $C_{ij}$  also determines the response of the crystal to external forces, as characterized by the bulk modulus, shear modulus, Young's modulus and Poisson's ratio and so play an important role in determining the strength of a material [106].

First-principles calculations that use periodic boundary conditions assume the existence of a single crystal, so all elastic constants can be determined by direct computation. The calculated  $C_{ij}$  can then be used to check the experimental bulk and shear moduli, if available and to calibrate model calculations. In addition, the elastic constants can be used to check the phase stability of proposed compounds [107, 108]. First-principles calculations can thus be used to predict the existence and properties of new materials and phases

### 2.8.2.2. Calculation of elastic constants

The simplest case by far is the cubic system where there are only three independent constants,  $C_{11}$ ,  $C_{12}$  and  $C_{44}$ , the off-diagonal stiffness matrix element  $C_{12}$  can be calculated using one or other of the relations

$$B = \frac{1}{2}(C_{11} + 2C_{12}) \quad 2.22.$$

$$C' = \frac{1}{2}(C_{11} - C_{12}) \quad 2.23.$$

Using both of these relations provides a useful independent check on the accuracy of the computation. A symmetry-general formulation of the calculation of elastic constants from total energy calculations is given by Le Page and Saxe [109].

The stress-strain relation may be used to distinguish the elastic and plastic regimes of solid materials [110]. The elastic moduli are the fundamental physical parameters which establish the stress-strain relation in the elastic regime. For an isotropic polycrystalline solid, the two independent elastic parameters are the bulk modulus ( $B$ ) and the shear modulus ( $G$ ). On the other hand, the resistance of solids to plastic or permanent deformation is governed by dislocation motion and may be expressed via the yield stress or mechanical hardness. The hardening mechanism in alloys, which arises from disturbances in the lattice caused by the solute atoms in the matrix, is often described by the classical Labusch-Nabarro model [111, 112]. Furthermore, the ratio of  $B$  to  $G$  is used to describe the brittleness and ductility of metal. High (low)  $B/G$  ratio corresponds to ductile (brittle) material. Of importance in metallurgy is how the solute atoms affect the elastic properties of  $ZrO_2$ .

The elastic properties of single crystals are described by the elements  $C_{ij}$  of the elasticity tensor. For each material, both stress and strain have three tensile and three shear components, giving six components in total. According to the theory of elasticity, a 6 x 6 symmetry matrix with 36 elements is thus needed to describe the relationship between stress and strain. The structural symmetry of crystal makes some of the matrix elements equal and others fixed at zero. For the cubic structures,

only three elastic constants, corresponding to  $C_{11}$ ,  $C_{12}$  and  $C_{44}$ , are independent. Applying two kinds of strains ( $\varepsilon_1$  and  $\varepsilon_4$ ) can give stresses relating to these three elastic coefficients, yielding an efficient method for obtaining elastic constants for the cubic system. This method has been successfully used to study the elastic properties of a range of materials including metallic systems [113]. The mechanical stability criteria of cubic systems as outlined elsewhere [114], is given as follows:

$$C_{44} > 0, C_{11} > |C_{12}| \quad \text{and} \quad C_{11} + 2C_{12} > 0 \quad 2.24.$$

where  $C_{11}$ ,  $C_{12}$  and  $C_{44}$  are the only three independent elastic constants [115]. While for tetragonal structures there are six elastic constants, corresponding to  $C_{11}$ ,  $C_{12}$ ,  $C_{13}$ ,  $C_{33}$ ,  $C_{44}$ , and  $C_{66}$  ( $C_{66} = (C_{11} - C_{12})/2$ ), are independent [116, 117]. Mechanical stability criterion for tetragonal crystal read as;

$$\begin{aligned} (C_{11} - C_{12}) > 0, (C_{11} + C_{33} - 2C_{13}) > 0, \\ (2C_{11} + C_{33} + 2C_{12} + 4C_{13}) > 0, C_{11} > 0, C_{33} > 0, C_{44} > 0, C_{66} > 0, \end{aligned} \quad 2.25.$$

On the other hand, for monoclinic structure, there are 10 independent elastic constants.

Mechanical stability criteria are as follows

$$C_{ij} > 0, (i=1-6),$$

$$\begin{aligned} (C_{22} + C_{33} - 2C_{23}) > 0 \\ (C_{33}C_{55} - C_{35}^2) > 0, (C_{44}C_{66} - C_{46}^2) > 0, [C_{11} + C_{22} + C_{33} + 2(C_{12} + C_{13} + C_{23})] > 0, \\ [C_{22}(C_{33}C_{55} - C_{35}^2) + 2C_{23}C_{25}C_{35} - C_{23}^2C_{55} - C_{25}^2C_{33}] > 0, \\ \{2[C_{15}C_{25}(C_{33}C_{12} - C_{13}C_{23}) + C_{15}C_{35}(C_{22}C_{13} - C_{12}C_{23}) + C_{25}C_{35}(C_{11}C_{23} - C_{12}C_{13})] - [C_{15}^2(C_{22}C_{33} - C_{23}^2) \\ + C_{25}^2(C_{11}C_{33} - C_{13}^2) + C_{35}^2(C_{11}C_{22} - C_{12}^2)] + gC_{55}\} > 0 \end{aligned} \quad 2.26.$$

$$g = C_{11}C_{22}C_{33} - C_{11}C_{23}^2 - C_{22}C_{13}^2 - C_{33}C_{12}^2 + 2C_{12}C_{13}C_{23},$$

Based on three independent single crystal elastic constants of a cubic crystal,  $C_{11}$ ,  $C_{12}$ ,  $C_{44}$ , the elastic moduli for polycrystalline material are calculated following averaging schemes of Voigt (upper bound) and Reuss (lower bound) by Hill [118] as follows:

$$\begin{aligned}
 E &= \frac{9BG}{3B+G}, \nu = \frac{E}{2G-1}, G_V = \left[ \frac{C_{11}-C_{12}+3C_{44}}{5} \right], \\
 G_R &= \left[ \frac{C_{44}(C_{11}-C_{12})}{4C_{44}+3(C_{11}-C_{12})} \right], G = G_H = \left[ \frac{G_V+G_R}{2} \right], \\
 B &= \left( \frac{C_{11}+2C_{12}}{3} \right), C' = \frac{C_{11}-C_{12}}{2}, A = \frac{2C_{44}}{C_{11}-C_{12}}
 \end{aligned} \tag{2.27}$$

where  $E$  is the Young's modulus,  $\nu$  Poisson's ratio,  $G$  isotropic shear modulus,  $B$  bulk modulus,  $C'$  tetragonal shear modulus and Zener anisotropic factor  $A$ . The Hill average, in general, is selected as the estimation of bulk modulus and shear modulus [119].

Secondly, the calculated elastic constants for tetragonal structures allows us to obtain the macroscopic mechanical parameters namely bulk moduli ( $B$ ) and shear moduli ( $G$ ) – for example, using the Voigt (V) approximation, as:

$$\begin{aligned}
 B_v &= \frac{1}{9} \{ 2(C_{11}+C_{12}) + C_{33} + 4C_{13} \}; \\
 G_v &= \frac{1}{30} \{ (M + 3C_{11} - 3C_{12} + 12C_{44} + 6C_{66}) \};
 \end{aligned} \tag{2.28}$$

$$\begin{aligned}
 C^2 &= (C_{11} + C_{12})C_{33} - 2C_{33}^2, M = C_{11} + C_{12} + 2C_{33} - 4C_{13}. \\
 E &= C_{33} - 2\nu C_{13}, \nu = \frac{C_{13}}{C_{11} + C_{12}} \text{ and } A_1 = \frac{2C_{66}}{C_{11} - C_{12}}
 \end{aligned} \tag{2.29}$$

On a basal plane (the plane perpendicular to the principal axis (c axis) in a tetragonal or structure).

$$A_2 = \frac{4C_{44}}{C_{11} + C_{33} - 2C_{13}} \quad 2.30.$$

, On (010) plane.

The calculated elastic constants for monoclinic phase allow us to obtain their macroscopic mechanical parameters, namely isotropic bulk ( $B$ ) and shear moduli ( $G$ ) in the Voigt (V) approximation as follows:

$$\nu = \frac{1}{2} \left[ \frac{B_X - (2/3)G_X}{B_X - (1/3)G_X} \right] \quad 2.31.$$

$$\Delta_P = \frac{C_{33}}{C_{11}}; \Delta_{S1} = \frac{C_{11} - C_{13}}{2C_{44}}; \Delta_{S2} = \frac{2C_{44}}{C_{11} - C_{12}}; \quad 2.32.$$

$$B_V = \frac{1}{9}(C_{11} + C_{22} + C_{33}) + \frac{2}{9}(C_{12} + C_{23} + C_{13}),$$

$$G_V = \frac{1}{15}(C_{11} + C_{22} + C_{33}) - \frac{1}{15}(C_{12} + C_{23} + C_{13}) + \frac{1}{5}(C_{44} + C_{55} + C_{66}) \quad 2.33.$$

$$\frac{1}{B_R} = (S_{11} + S_{22} + S_{33}) + 2(S_{12} + S_{23} + S_{13});$$

$$\frac{1}{G_R} = \frac{4}{15}(S_{11} + S_{22} + S_{33}) - \frac{4}{15}(S_{12} + S_{23} + S_{13}) + \frac{1}{5}(S_{44} + S_{55} + S_{55})$$

$$B_H = \frac{1}{2}(B_R + B_V), \quad G_H = \frac{1}{2}(G_R + G_V) \quad 2.34.$$



For an elastically isotropic monoclinic crystal, the three anisotropy ratios ( $A_1$ ,  $A_2$  and  $A_3$ ) must be simultaneously equal to unity [77]. As given in equation 8 above,  $E_x$  represents the Young's modulus along the [100] and [010] directions, whereas  $E_z$  on the other hand represents Young's modulus along the [001] direction. The Young's modulus  $E$  is defined as the ratio between stress and strain and is used to provide a measure of the stiffness of the solid, i.e. the larger the value of  $E$ , the stiffer the material. Poisson's ratio ( $\nu$ ) refers to the ratio of transverse contraction strain to longitudinal extension strain during stretching, thus reflecting the stability of the crystal against shear. Hence, the higher the Poisson's ratio is, the better ductility the crystalline metal has at low temperatures. It is acknowledged that the bulk modulus  $B_0$  is a measure of resistance to volume changed by applied pressure. The elastic anisotropy  $A$  has an important implication in engineering science since it is highly correlated with the possibility of inducing microcracks in materials [78]. If the material is completely isotropic, the value of  $A$  will be equal to unity, whereas values smaller or larger than 1 measure the degree of elastic anisotropy. Thus the macroscopically measurable quantities obtained for materials are the shear modulus  $G$ , which represents the isotropic response for shearing, Young's modulus  $E$  corresponding to the stress–strain ratio in the case of tensile forces, bulk modulus  $B_0$ , Poisson's ratio  $\nu$  and the anisotropy constant  $A$ , which are all important for technological and engineering applications.

## 2.9. Density of states

The density of states (DOS) is a useful mathematical concept allowing integration with respect to the electron energy to be used instead of the integration over the Brillouin zone. In addition, the DOS is often used for quick visual analysis of the electronic structure. Characteristics such as the width of the valence band, the energy gap in insulators and the number and intensity of the main features are helpful in qualitatively interpreting experimental spectroscopic data. DOS analysis can also help to understand the changes in electronic structure caused by, for example, external pressure. More accurate methods are based on linear or quadratic interpolations of band energies between the reference points in the Brillouin zone. The most popular and reliable technique, which is based on the tetrahedron interpolation, is unfortunately ill suited to the Monkhorst-Pack grid of special points. Therefore CASTEP uses a simplified linear interpolation scheme [120]. This method

is based on the linear interpolation in parallelepiped formed by the points of the Monkhorst-Pack set, followed by the histogram sampling of the resultant set of band energies.

### 2.10. Calculation Steps of the Work

All of our calculations for the chemical problems mentioned in this thesis have been made by means of state of art DFT using the code CASTEP. Various lateral sizes of VCA cells were chosen for studying  $\text{ZrO}_{2-x}\text{S}_x$  for different  $x$ . The  $x$  values were ranging from 0 to 2 for each calculation. In the present work, to account for exchange and correlation functional the generalized gradient approximation as proposed by Wu and Cohen (WC) has been applied as it is established that this approximation for the functional gives accurate description of solids processes. In all the calculations, k-points spacing was set to 0.05 Å within the Brillouin zone as generated by Monkhorst-Pack scheme. The plane wave pseudopotential approach combined with k-point sampling results in time saving and accurate calculations. Geometry optimization was conducted using the Broyden-Fletcher-Goldfarb-Shanno (BFGS) method [71]. We employed a convergence criterion of less than  $5 \times 10^{-6}$  eV on the total energy per atom, maximum displacement of  $5 \times 10^{-4}$  Å, residual forces of  $3 \times 10^{-2}$  eV Å<sup>-1</sup> and 0.02 GPa on the residual bulk stress. For each crystal structure, a geometry optimization was performed to obtain the equilibrium structural properties, from which the elastic constant were computed as described below. All the parameters are checked for their sensitivity and the variation in measured quantity like lattice parameters.

## CHAPTER 3

### RESULTS AND DISCUSSIONS

#### 3. Results and discussions

The results we present in this work pertain to electronic, structural and elastic properties of the solid solution zirconium oxide/sulphide ( $\text{ZrO}_{2-x}\text{S}_x$ ), which was previously investigated theoretically for certain sulphate  $\text{ZrO}_2$ , particularly for *c*- $\text{ZrO}_2$ . We verify the validation of improved VCA method through comparison with previous experimental and theoretical studies. Moreover, we predict additional properties of  $\text{ZrO}_{2-x}\text{S}_x$  which were not mentioned before [51, 52].

#### 3.1. Cut-off energy and k-points convergence of $\text{ZrO}_{2-x}\text{S}_x$

For total energy calculations providing electronic, structural and elastic properties in CASTEP, there are two computational parameters, namely the number of basis functions (plane wave cut-off) and the number of k-points (k spacing) that need to be checked. Different cut-off energies and k-points have been tested for different functionals.

##### 3.1.1. Cut-off energy

In order to determine the appropriate cut-off energy for  $\text{ZrO}_2$ , geometry optimisation calculations were performed for different kinetic energy cut-offs at a default number of *k*-points for each system within GGA-PBE, LDA and GGA-WC. We used ultrasoft pseudopotentials [121], which require significantly less computational resources than the norm-conserving potentials [122]. In figure 5 we show the curves of total energy per atom against the cut-off energy for *c*- $\text{ZrO}_2$ . An energy cut-off of 400eV was chosen for  $\text{ZrO}_2$ . Higher cut-off energies give less energies than that given by 400eV. beyond this value, total energy differences is less than 1meV/atom. We choose this cut-off energy to reduce computational cost.

##### 3.1.2. k-points

We show the convergence of the total energies with respect to the *k*-point sampling set size, as illustrated in figure 5. We have carried out a total energy calculation at fixed cut-off energy for a structure (determined above) while the number of k-points was varied for GGA-PBE, LDA and GGA-WC functionals. The total energy with respect to the number of k-points was considered converged when the energy

change per atom (between two consecutive points) was within 1meV per atom. Although 2x2x2 gives lowest energy, we found that this setting can affect cell parameters and does not provide converged results for other calculations.

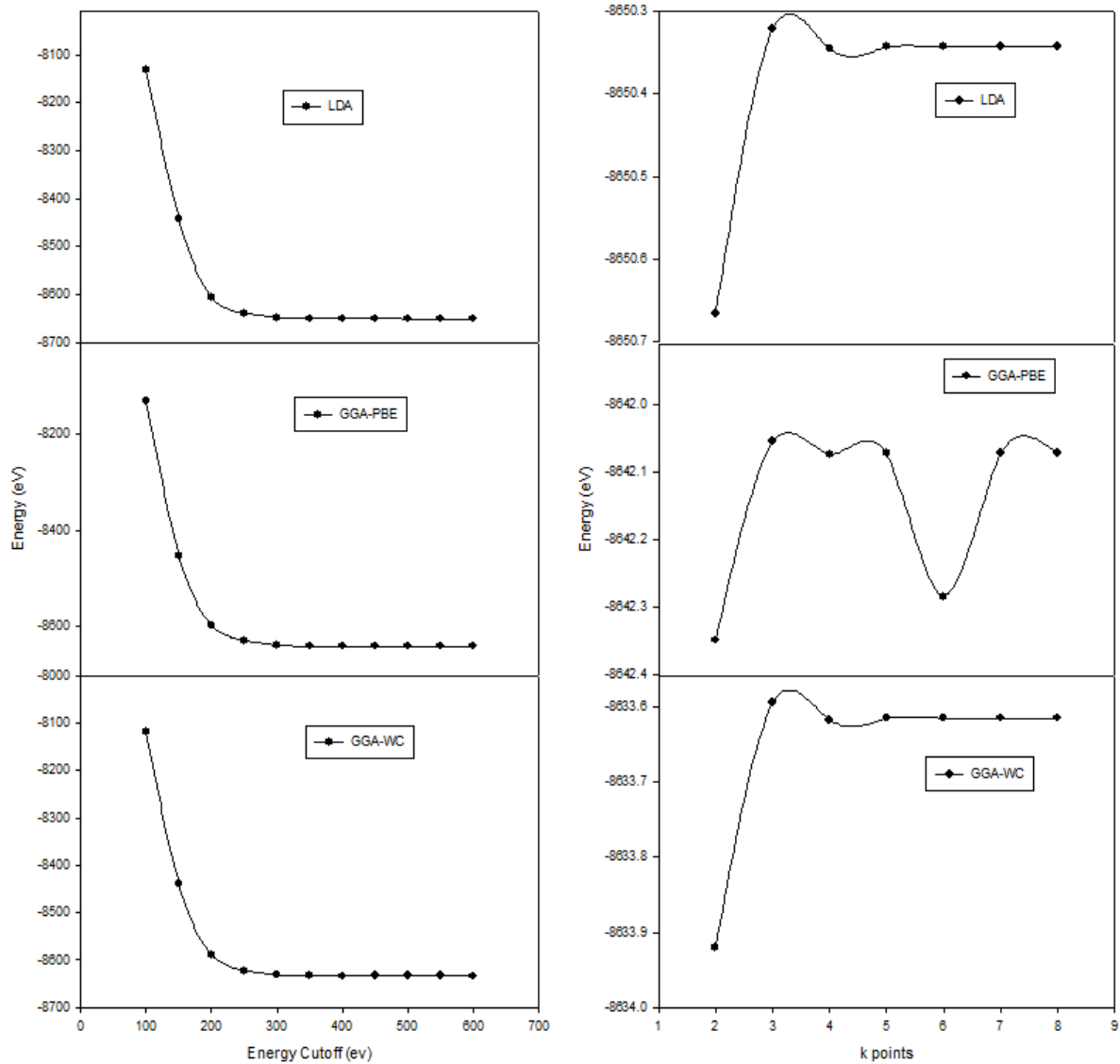


**Figure 5** The graphs of total energy (eV/atom) against energy cut-off and total energy (eV/atom) against number of k -points for the c-ZrO<sub>2</sub>

The  $k$ -points were chosen to be 6x6x6, as shown in figure 5 and they are set according to Monkhorst-Pack scheme. It gives good convergence at reasonable computational cost. The exchange correlation potential used in this work is the GGA-WC since it gives good lattice constants of c-ZrO<sub>2</sub>. Analysis of calculated lattice parameters (see table 4) shows that the lowest deviation from the experimental data

(lowest relative volume changes) are obtained by using Wu-Cohen (WC) GGA functional. The deviation of lattice parameter for  $c\text{-ZrO}_2$  is less than 1%, while for PBE-GGA functional and LDA is 2.5% and 3.5% respectively.

### 3.1.3. Summary of cut-off energies and $k$ -points

Cut-off energy and equivalent number of  $k$ -points were used for the other structures considered in the current study. The same cut-off energy and  $k$ -points were used for all  $c\text{-ZrO}_{2-x}\text{S}_x$  structures for  $x > 0$ . The GGA-WC gives the lattice parameters that are closest to experimental ones and to other first principle calculations, as seen in Table 2 the percentage difference between the calculated tetragonal structure  $t\text{-ZrO}_2$  lattice parameters and the experimental is 0.3% for  $a$  and 0.8% for  $c$ , while for monoclinic  $m\text{-ZrO}_{2-x}\text{S}_x$  it is 0.7% for  $a$ , 0.9% for  $b$  and 0.6% for  $c$  and for ZrOS the lattice parameter is 2.8%. Since all lattice parameters are in good agreement with those obtained from experiments, we used the same cut-off energy for the structure studied in this thesis. Our cut-off energy and  $k$ -point values correspond to other values that were used by previous studies for all phases of unsulphated  $\text{ZrO}_2$

## 3.2. Structural properties

Beginning with experimental structural parameters, the 12-atom cell of  $c\text{-ZrO}_2$ ,  $t\text{-ZrO}_2$ ,  $m\text{-ZrO}_2$ , ZrOS and  $\text{ZrS}_2$  were optimized (cell shape and size, atomic positions). The geometric optimisation parameters corresponding to this fully optimised geometry are shown on Tables 4, 5, 6 and 7, and other available first principle calculated values are also displayed. The results from earlier studies are quoted for comparison.

### 3.2.1. Crystal structure

Present results agree well with previous theoretical and experimental results for  $\text{ZrO}_{2-x}\text{S}_x$  at  $x = 0$  for all three zirconium dioxide polymorphs and at  $x = 0.5$  which was previously investigated for cubic zirconia. VCA simulations were used to study a series of disordered  $\text{ZrO}_{2-x}\text{S}_x$  compounds. The calculated lattice constants and the corresponding cell volumes expansions for  $\text{ZrO}_2$  and  $\text{ZrO}_{2-x}\text{S}_x$  (cubic, tetragonal and monoclinic for  $x$  ranging from 0 to 2) are all plotted against  $S$  atomic compositions as presented in figures 6, 9 and 10 respectively.

The volume expansion rate is given by the formula

$$\alpha = \frac{V_x - V_0}{V_0},$$

Where  $V_x$  represents the volume of the doped compound with  $S_x$  and  $V_0$  represents the volume of pure  $ZrO_2$ . The results show that the expansion rates of  $ZrO_{2-x}S_x$  differ considerably for different  $x$  values.

From Table 4 we obtained the lattice constant 5.082Å which is slightly smaller than the experimental lattice constant of 5.086 Å by 0.08%., other available first principle calculations agree well with our calculations. The lattice parameters for sulphated  $c$ - $ZrO_2$  in Table 5 also showed good agreement with the available results of sulphated structures,  $a$  is 0.37% different for  $ZrO_{1.5}S_{0.5}$ , 0.4% different for  $ZrOS$  and for  $ZrS_2$  0.71% difference for  $a$  and 0.17% for  $b$ . The distance between atoms of  $ZrO_{2-x}S_x$  is slightly increasing as sulphur increases.

**Table 4** Calculated structural parameters  $c$ - $ZrO_2$  and of corresponding available theoretical calculations.

parameter	Expt [123]	WC	LDA [124]	LDA [125]	PW91 [126]	TB [127]	LD [128]	GGA [129]
a(Å)	5.086	5.082	5.037	5.037	5.164	5.20	5.023	5.128

**Table 5** The optimised structural parameters of  $ZrOS$ ,  $ZrO_{1.5}S_{0.5}$  and  $ZrS_2$

Structures	$c$ - $ZrO_{1.5}S_{0.5}$		$ZrOS$		$ZrS_2$	
	WC	Exp [51]	WC	Exp [50]	WC	Exp [130]
a	5.441	(5.421)	5.691	(5.692)	3.662	(3.636)
b					5.810	(5.820)

#### $c$ - $ZrO_{2-x}S_x$

The dependence of the lattice constant of  $c$ - $ZrO_{2-x}S_x$  solid solutions on S content is observed in figure 6. As S increases the lattice constants changes and the cell

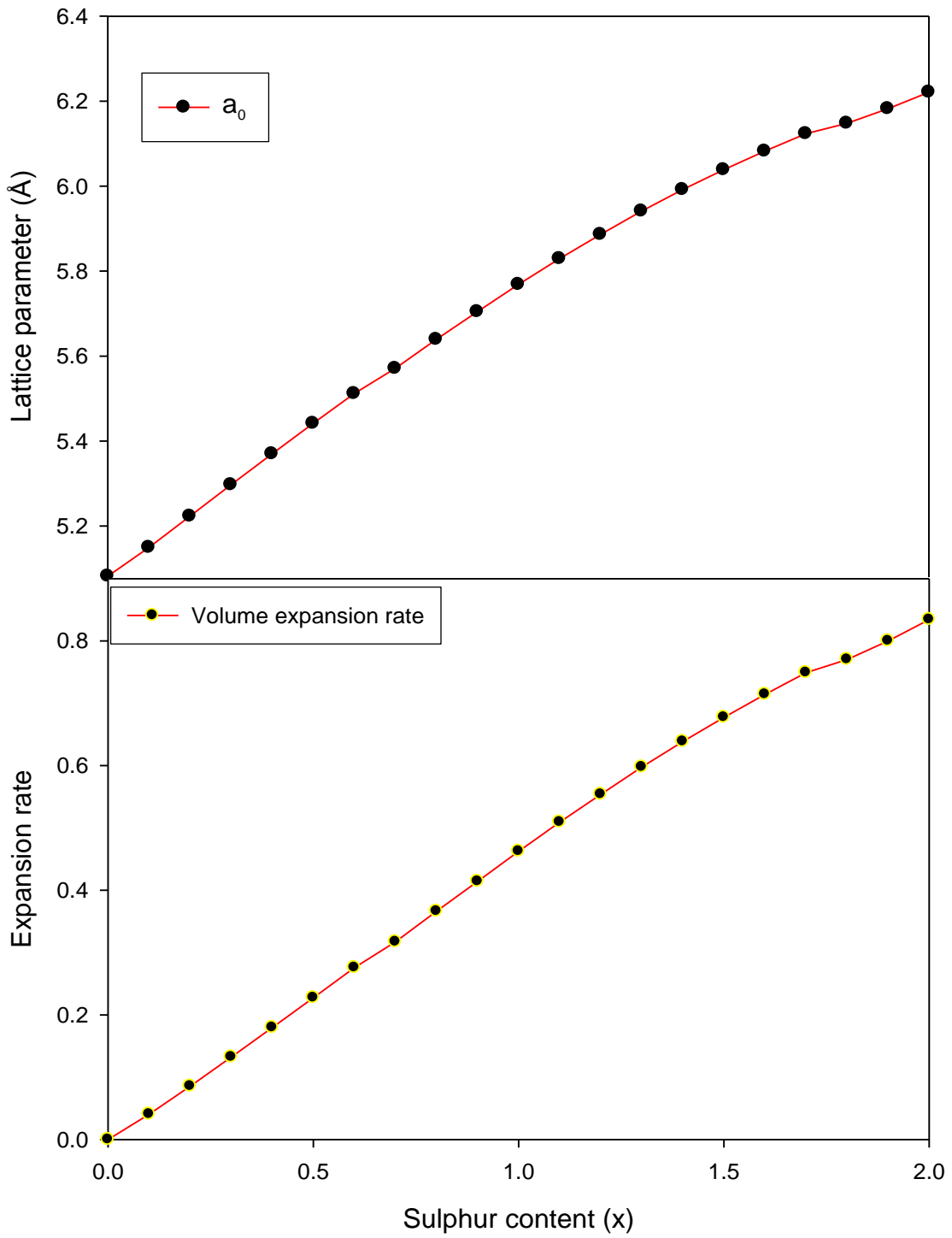
volume expands near linearly, from  $x = 0$  to  $x = 1.4$  but above 1.4 the increasing rate decreases slightly until  $x = 2.0$ . The reason why the lattice constant (a,b and c) of S-doped  $ZrO_2$  is greater than that of undoped  $ZrO_2$ , is that the lattice constant are closely related to the radius of the doping atoms, as the radius of S is larger than that of O.

In the same figure we also showed volume expansion rate which is positive. The volume increase has the effect of increasing the average Zr-OS distance, normally found in either high temperature or stabilised phase of  $c-ZrO_2$ . This bond lengthening is expected to increase the ionicity of Zr-OS, and such results can be accounted for considering the bonding characteristics and properties of O and S atoms. The larger size of the S atom forces the system to have a larger lattice constant, this will introduce longer bond length in the system.

Since  $B \propto V^{-1}$ , where  $V$  is the unit cell volume, it can be deduced that, a larger lattice constant leads to a small bulk modulus. This has also been demonstrated for various perovskite and other material [131], consequently an increase in sulphur decrease the bulk modulus.

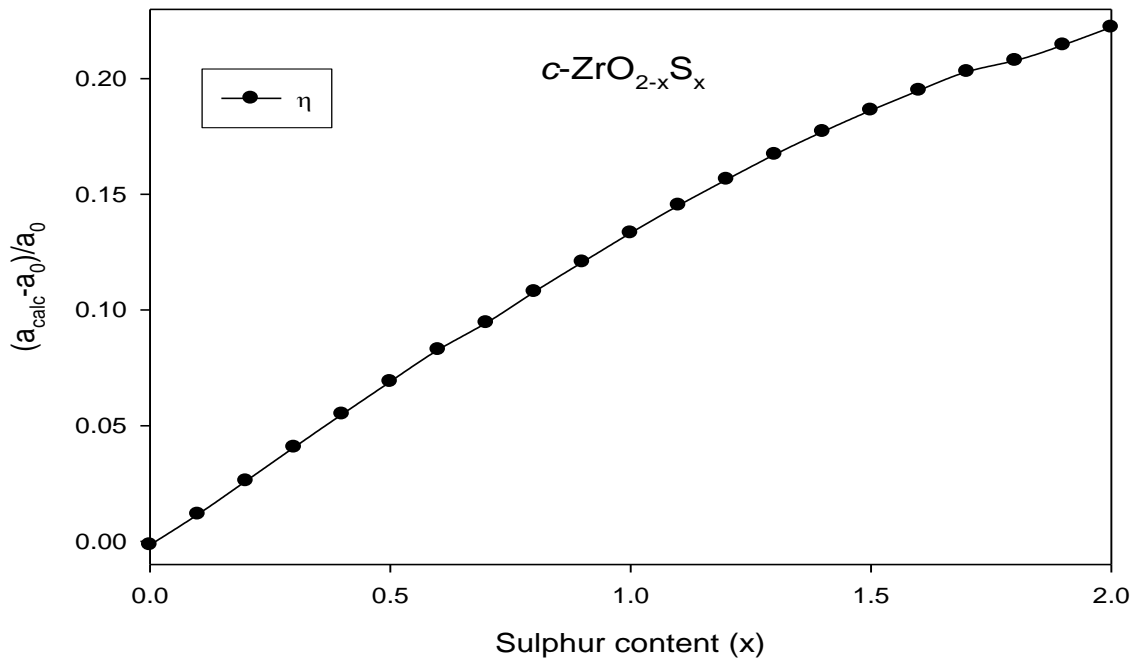
A parameter  $\eta$  defined as  $(a_{calc} - a_0) / a_0$ , is used to represent lattice-constant dilation or shrinkage relative to pure  $c-ZrO_{2-x}S_x$ , where  $a_0$  is the lattice constant of pure  $c-ZrO_2$  and  $a_{calc}$  is the calculated lattice constant for  $ZrO_2$  and the solid solution  $ZrO_{2-x}S_x$  for  $0 < x \leq 2$ .  $\eta > 0$  represents lattice constant dilation and  $\eta < 0$  represents the shrinkage, in our case sulphur content increases the  $c-ZrO_2$  lattice constant by 1.1%-20%. In material strengthening, the strain field and atomic-size misfit due to partial replacement-induced  $\eta$  are responsible for solute-solution strengthening through solute-dislocation interactions [132]. Thus the information on dilation of the lattice constant, represented by  $\eta > 0$  is useful for further studies of solid solution strengthening of  $ZrO_{2-x}S_x$ .

Figure 8 presents a variation of bond length of  $c-ZrO_{2-x}S_x$  as a function of sulphur content, this change in bond length is almost linear below  $x = 1.4$ , the bond length showed a similar trend as the lattice constant and cell volume expansion rate with sulphur content. Our calculations of bond length have been done using VCA model.



**Figure 6** Variation of the lattice parameter and volume expansion rate with S mole fraction  $x$ , in  $c\text{-ZrO}_{2-x}\text{S}_x$  solid solution.





**Figure 7** Variation of the lattice constant dilation or shrinkage with S mole fraction  $x$ . for  $c\text{-ZrO}_{2-x}\text{S}_x$  solid solution.

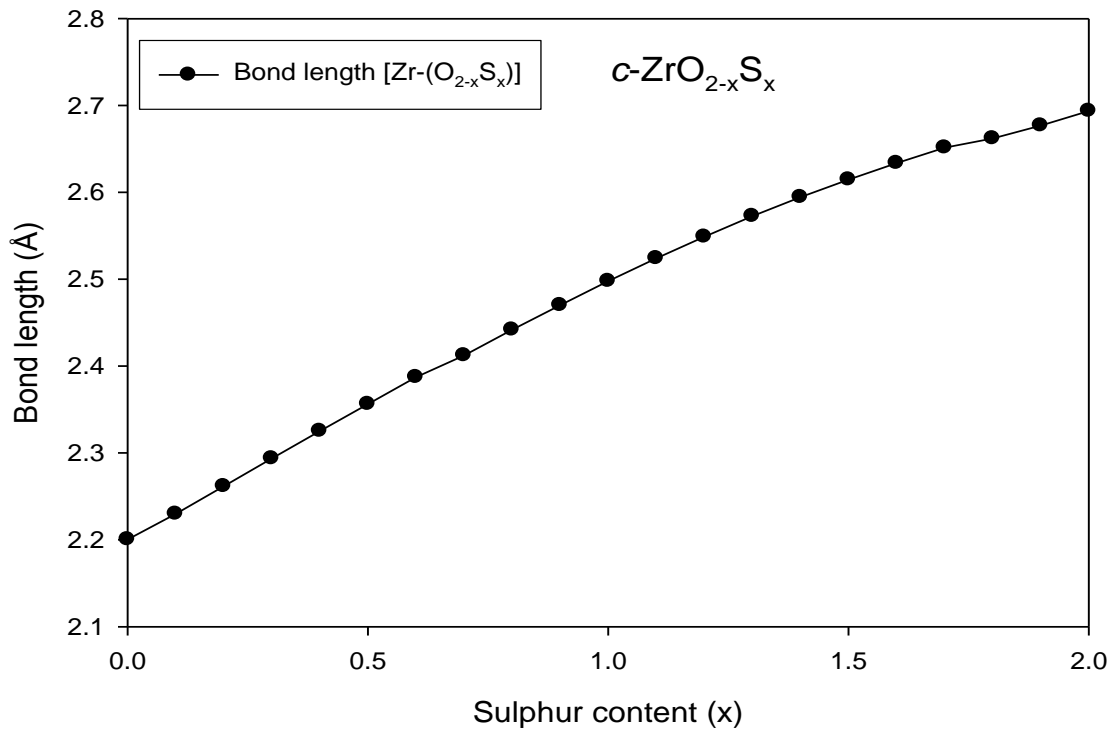


**Figure 8** Variation of bond length (Å) with S mole fraction  $x$  in  $c\text{-ZrO}_{2-x}\text{S}_x$  solid solution.

### ***t*-ZrO<sub>2-x</sub>S<sub>x</sub> and *m*-ZrO<sub>2-x</sub>S<sub>x</sub>**

Presently evaluated lattice parameters  $a = 3.589 \text{ \AA}$  and  $c = 5.21 \text{ \AA}$  for *t*-ZrO<sub>2</sub> and  $a = 5.140 \text{ \AA}$ ,  $b = 5.22 \text{ \AA}$ ,  $c = 5.32 \text{ \AA}$  and  $\beta = 99.1^\circ$  agree well with experimental and other theoretical data in Table 6 and Table 7 respectively. The percentage difference between  $a$  and  $b$  lattice parameters for *t*-ZrO<sub>2</sub> and their respective experimental values is approximately 0.5%, and for *m*-ZrO<sub>2</sub> the difference is approximately 0.5% for  $a, b, c$  and angle  $\beta$ . The tetragonal and the monoclinic structures also form a series of *t*-ZrO<sub>2-x</sub>S<sub>x</sub> and *m*-ZrO<sub>2-x</sub>S<sub>x</sub> mixed solid solution respectively with no restriction on the concentration of the component ; $0 < x < 2$ : the variation of lattice parameters  $a, b$  and  $c$  for *t*-ZrO<sub>2-x</sub>S<sub>x</sub> and  $a, b, c$  and  $\beta$  for *m*-ZrO<sub>2-x</sub>S<sub>x</sub> as a function of their composition are plotted in figure 9 and 10, respectively.

In figure 9 the lattice parameters  $a$  and  $c$  for tetragonal structure increase at the substitution of oxygen concentration by sulphur atomic concentration. In figure 10  $a, b$  and  $c$  also increase as a function of sulphur concentration. This observation may be accounted for by replacing an atom of covalent radius  $0.65 \text{ \AA}$  for the host atom oxygen by that of  $1.09 \text{ \AA}$  for sulphur. The larger atom replacing the smaller ones causes the observed lattice parameters to expand in the solid solution. The volume expansion rate could be attributed for by similar cause.

Figure 11( shows variation of the axial ratio  $c/a$  for *t*-ZrO<sub>2-x</sub>S<sub>x</sub>, lattice anisotropy  $c/b$ , and angle  $\beta$  for *m*-ZrO<sub>2-x</sub>S<sub>x</sub> as the function of their composition. The axial ratio of *t*-ZrO<sub>2-x</sub>S<sub>x</sub> generally increases from  $x = 0$  to  $1.1$  and it also increases from  $1.8$  to  $2.0$ , and it decreases from  $1.1$  to  $1.8$ . The change in  $c/a$  with sulphur content is important, because it has a direct influence on elastic anisotropy. The *t*-ZrO<sub>2-x</sub>S<sub>x</sub> displays a common behaviour with a saturation of the axial ratio at limiting value. The axial ratio has a minimum value at  $x = 0$  and the maximum value at  $x = 1.1$ .

In figure 11(b) The variation of lattice anisotropy, with composition of mixed crystal shows quite a different behaviour, noticeably decreases at first from  $x = 0$  to  $x = 0.9$  and shows a slight increase from  $x = 0.9$  to  $x = 1.3$ . And then increases from  $x = 1.3$  to  $x = 2$ , with the substitution of oxygen by sulphur. Thus when sulphur atoms replace oxygen atoms the unit cell becomes less or more anisotropic depending on

the concentration of sulphur in  $m\text{-ZrO}_{2-x}\text{S}_x$ ; on the other hand, when  $x = 1.3$  the unit cell is least anisotropic.

In figure 11(c) the monoclinic angle  $\beta$  also increase with  $x$  up to  $x < 1.2$ , but start decreasing for  $x \geq 1.2$ , and the value of  $\beta$  is highest for  $x = 1.2$ . There is not much change on the angle and the structure seems to maintain the monoclinic cell, as a function of sulphur content.

**Table 6** Experimental, calculated and other first principle lattice parameters for  $t\text{-ZrO}_2$

PARAMETER	Exp [123]	WC	LDA [124]	LDA [125]	PW91 [126]	TB [133]	LD [128]	GGA [129]
a(Å)	3.606	3.589	3.557	3.565	3.654	3.571	3.637	3.629
c(Å)	5.180	5.12	5.100	5.126	5.364	5.184	5.269	5.207

**Table 7** Experimental, calculated and other first principle lattice parameters and angle  $\beta$  for  $m\text{-ZrO}_2$

parameter	Exp [18]	Exp [134]	Exp [123]	WC	LDA [124]	LDA [125]	PW91 [126]	TB [133]	GGA [129]
a (Å)	5.169	5.1450	5.1505	5.140	5.108	5.102	5.192	5.076	5.1974
b (Å)	5.232	5.2075	5.2116	5.222	5.170	5.181	5.254	5.081	5.2798
c (Å)	5.341	5.3107	5.3173	5.320	5.272	5.264	5.358	5.172	5.3498
$\beta$	99.25	99.23	99.230	99.77	99.21	99.65	99.65	98.0	99.53

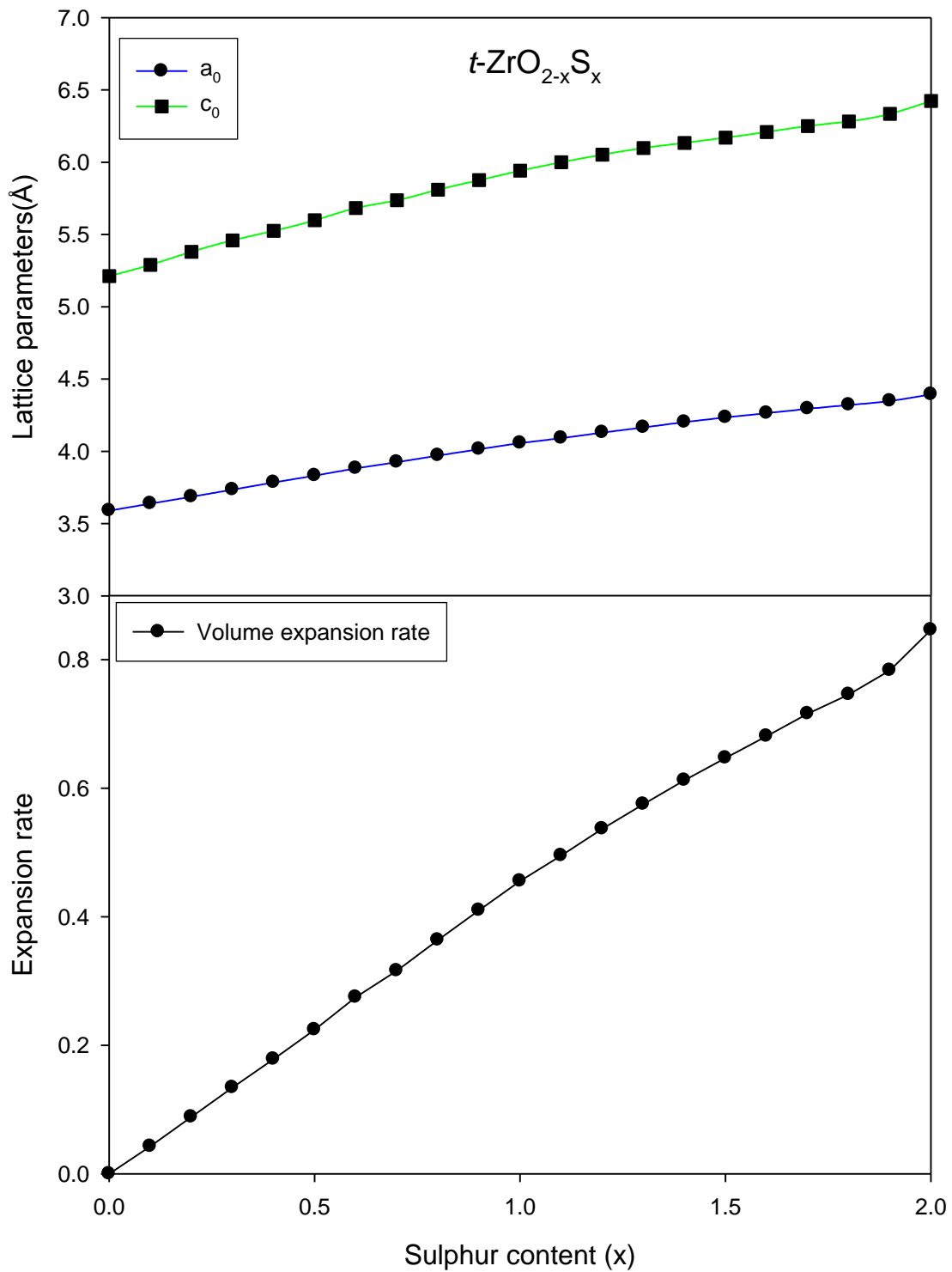


**Figure 9** Variation of the lattice parameters and volume expansion rate with S mole fraction x for  $t\text{-ZrO}_{2-x}\text{S}_x$  solid solution.

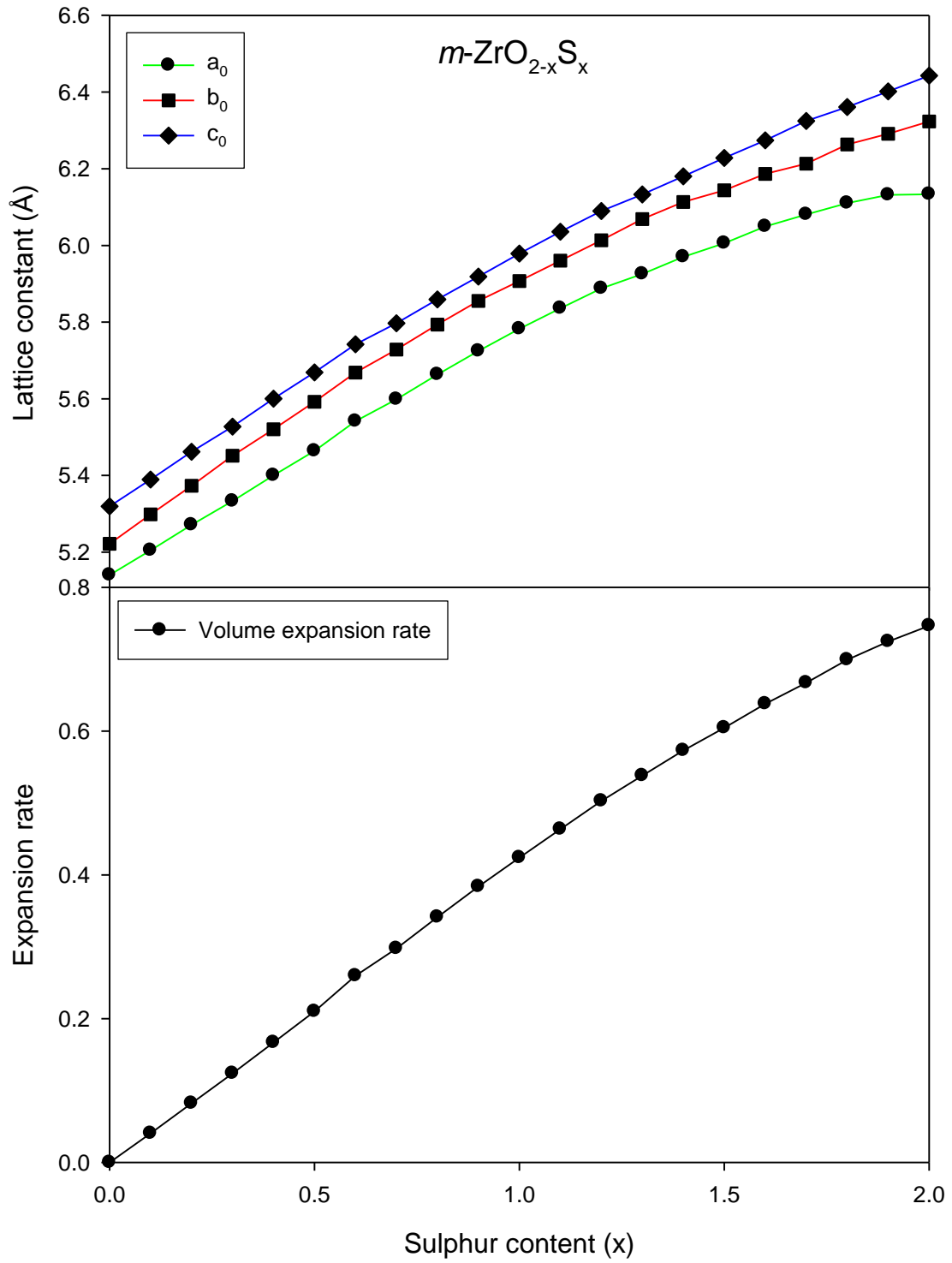


**Figure 10** Variation of the lattice parameters and volume expansion rate with S mole fraction x for  $m\text{-ZrO}_{2-x}\text{S}_x$  solid solution.

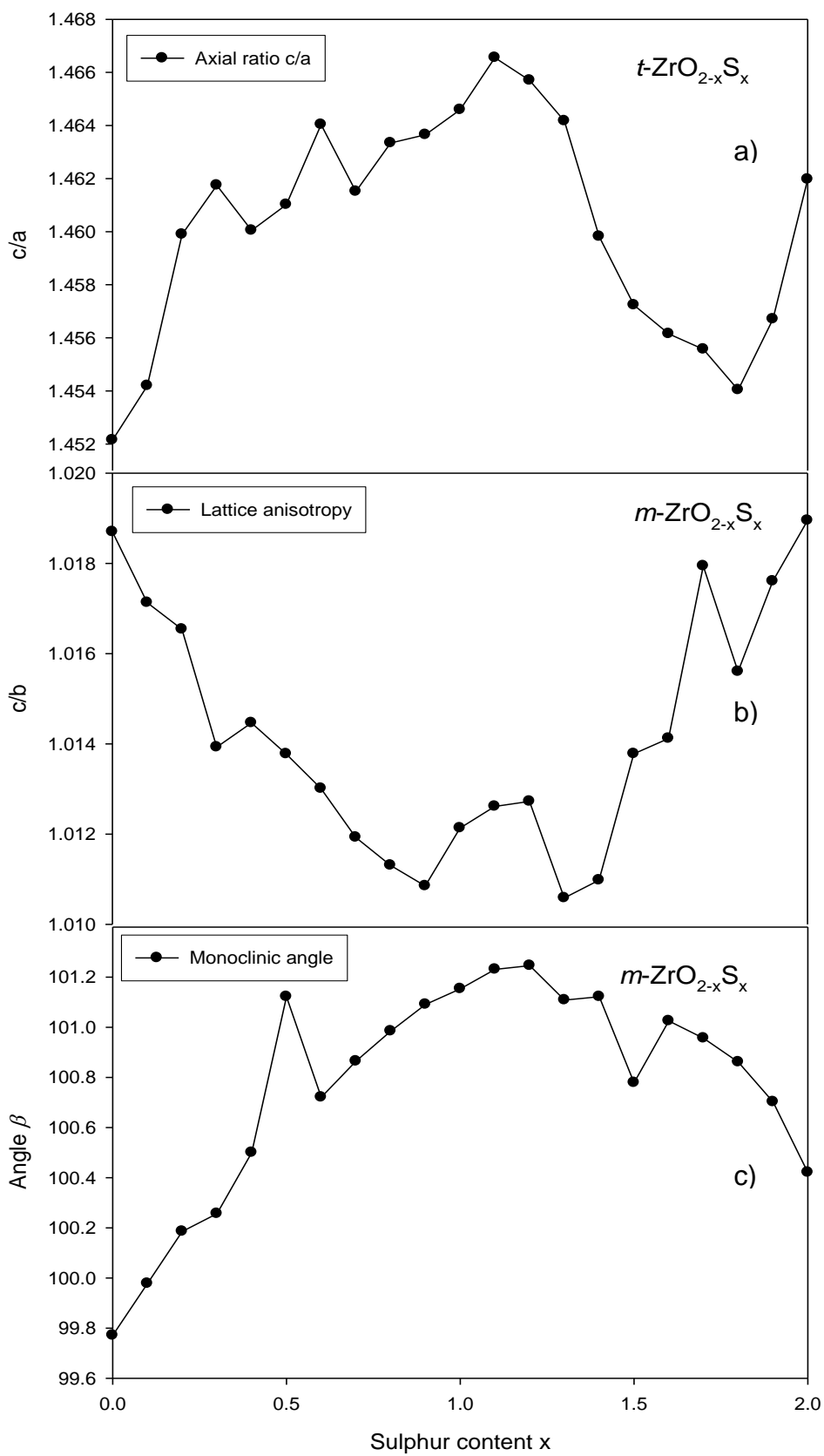


**Figure 11** Variation of a) axial ratio ( $c/a$ ) of  $t\text{-ZrO}_{2-x}\text{S}_x$ , b) lattice anisotropy ( $c/b$ ) and c) monoclinic angle  $\beta$  of  $m\text{-ZrO}_{2-x}\text{S}_x$  solid solutions with S mole fraction  $x$ .

### 3.2.2. Formation energies and cohesive energies.

For the better understanding of the stability of  $ZrO_{2-x}S_x$  solid solution, the calculations of formation energy and cohesive energy were performed, the average formation energy of  $ZrO_{2-x}S_x$  solid solution is defined as;

$$\Delta H = E_{ZrO_{2-x}S_x} - E_{Zr(crystal)} - (2-x)E_{O(crystal)} - xE_{S(crystal)}$$

where  $E_{ZrO_{2-x}S_x}$ ,  $E_{Zr(crystal)}$ ,  $E_{O(crystal)}$  and  $E_{S(crystal)}$  are the total energies of  $ZrO_{2-x}S_x$ , Zr, O and S at their most stable states, respectively. The obtained formation energy of  $ZrO_{2-x}S_x$  is shown in figures 12, 13 and 14, for *c*- $ZrO_{2-x}S_x$ , *t*- $ZrO_{2-x}S_x$  and *m*- $ZrO_{2-x}S_x$ , respectively.

Table 8, summarises values of cohesive and formation energies for *m*- $ZrO_{2-x}S_x$ , *t*- $ZrO_{2-x}S_x$ , *c*- $ZrO_{2-x}S_x$  and ZrOS. The calculated cohesive energies for pure structures of  $ZrO_2$  are in agreement with other first principle calculations within a maximum error of 16%. Whereas, for ZrOS the error is less than 1%. The formation energies for *c*- $ZrO_2$  and ZrOS also showed good agreement with the available experimental results, 3.2% difference for  $ZrO_2$ , 4.7% difference for ZrOS.

From figure 12, for cubic structure, the formation energy of  $ZrO_{2-x}S_x$  becomes larger when *x* increases from 0 to 0.7, between 0.77 and 1.35 it is positive and above 1.3 it is negative again, indicating that the addition of S to the cubic structure does not increase the stability of the *c*- $ZrO_2$ , it should be noted that when *x* equal to 0 or 2 the heat of formation is more negative than for any other sulphated *c*- $ZrO_2$ , the stability of the structure is also correlated to its cohesive energy; and the cohesive energy is often defined as energy needed when the crystal is decomposed into the single atoms, so in general the more negative the cohesive energy is, the more stable is the crystal. In this work the cohesive energy is calculated using this formula:

$$\Delta H = E_{ZrO_{2-x}S_x} - E_{Zr(atom)} - (2-x)E_{O(atom)} - xE_{S(atom)}$$

where  $E_{ZrO_{2-x}S_x}$  is the total electronic energy of  $ZrO_{2-x}S_x$  and  $E_{Zr(atom)}$ ,  $E_{O(atom)}$  and  $E_{S(atom)}$  are the electronic total energies of a single Zr, O and S atom in their free states, respectively. The obtained cohesive energy of  $ZrO_{2-x}S_x$  is shown in figures 12, 13 and 14, for  $c$ - $ZrO_{2-x}S_x$ ,  $t$ - $ZrO_{2-x}S_x$  and  $m$ - $ZrO_{2-x}S_x$  respectively.

The calculated cohesive energy of  $c$ - $ZrO_{2-x}S_x$ , increases from 0 to 1.2 and starts to decrease from 1.3 to 2 and it is positive from 0.23 to 1.93, hence, this structure can be considered energetically unstable for a wide range of S concentrations. The cohesive energy of  $ZrO_{2-x}S_x$ , with an increase in S, exhibits a similar variation tendency as seen in the graph of formation energy.

Hence from results of formation energy and cohesive energies it can be expected that with the increase of x,  $ZrO_2$  possess transformation tendency from one symmetry to the other by substitution of O with S in  $ZrO_2$ . This can further degrade the mechanical properties of  $ZrO_2$  compound, which confirms the analysis by Oleskar et al. [51]. The results show not only the extension of the zirconia structure but also the small atomic displacements from equilibrium positions. Since it is the main causes of stabilisation in  $ZrO_2$ , it is expected that sulphur dope zirconium (SDZ) can be stable at room temperature, however the calculated cohesive and formation energies for doped structures are higher compared to pure  $ZrO_2$ . This may be attributed to addition of S with higher e/atom (electron per atom) than O, increasing the overall e/atom of solid solution to an inappropriate value.

**Table 8** Calculated cohesive energy (eV) and formation energies (eV) for undoped and Sulphur-doped zirconia. Bracketed values are from other theoretical work.

structures	$m$ - $ZrO_2$	$t$ - $ZrO_2$	$c$ - $ZrO_2$	ZrOS	Refs
$E_{coh}$ (eV)	-28.377	-28.287	-28.283	-21.200	WC
	(-24.478)	(-24.050)	(-24.354)	(-21.355)	[51]
$E_{form}$ (eV)	-10.854	-10.764	-10.760	-8.276	WC
			(-11.12)	(-7.88)	[135]



For  $c\text{-ZrO}_{2-x}\text{S}_x$ ,  $t\text{-ZrO}_{2-x}\text{S}_x$  and  $m\text{-ZrO}_{2-x}\text{S}_x$  the cohesive energy is positive for  $0.74 < x < 1.54$  while the formation energy is positive for  $0.2 < x < 1.93$ . which implies that at this range the solid solution is not stable or it decomposes in other structures.

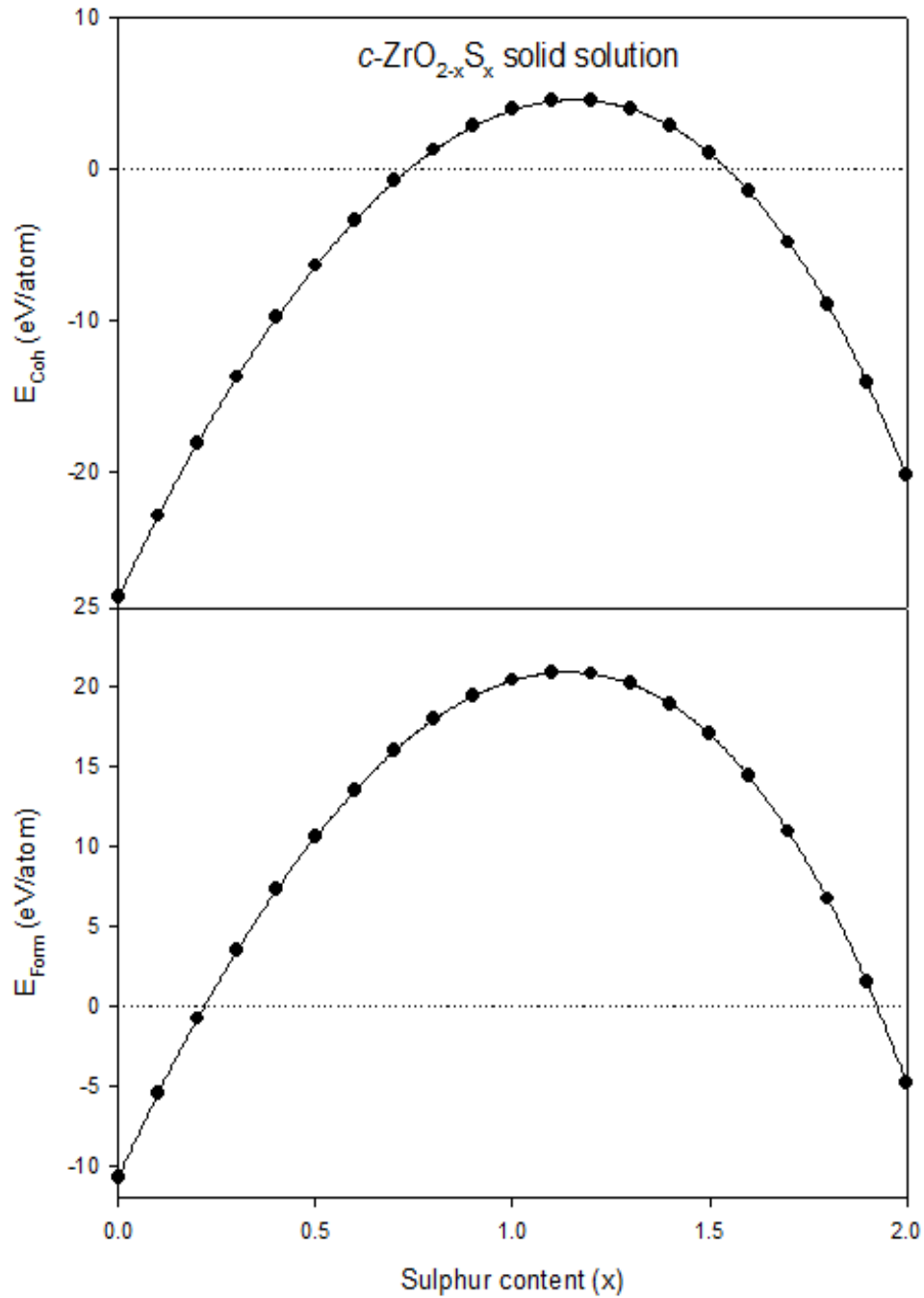


**Figure 12** Variation of the formation energy and cohesive energy with S mole fraction for  $c\text{-ZrO}_{2-x}\text{S}_x$  solid solution.

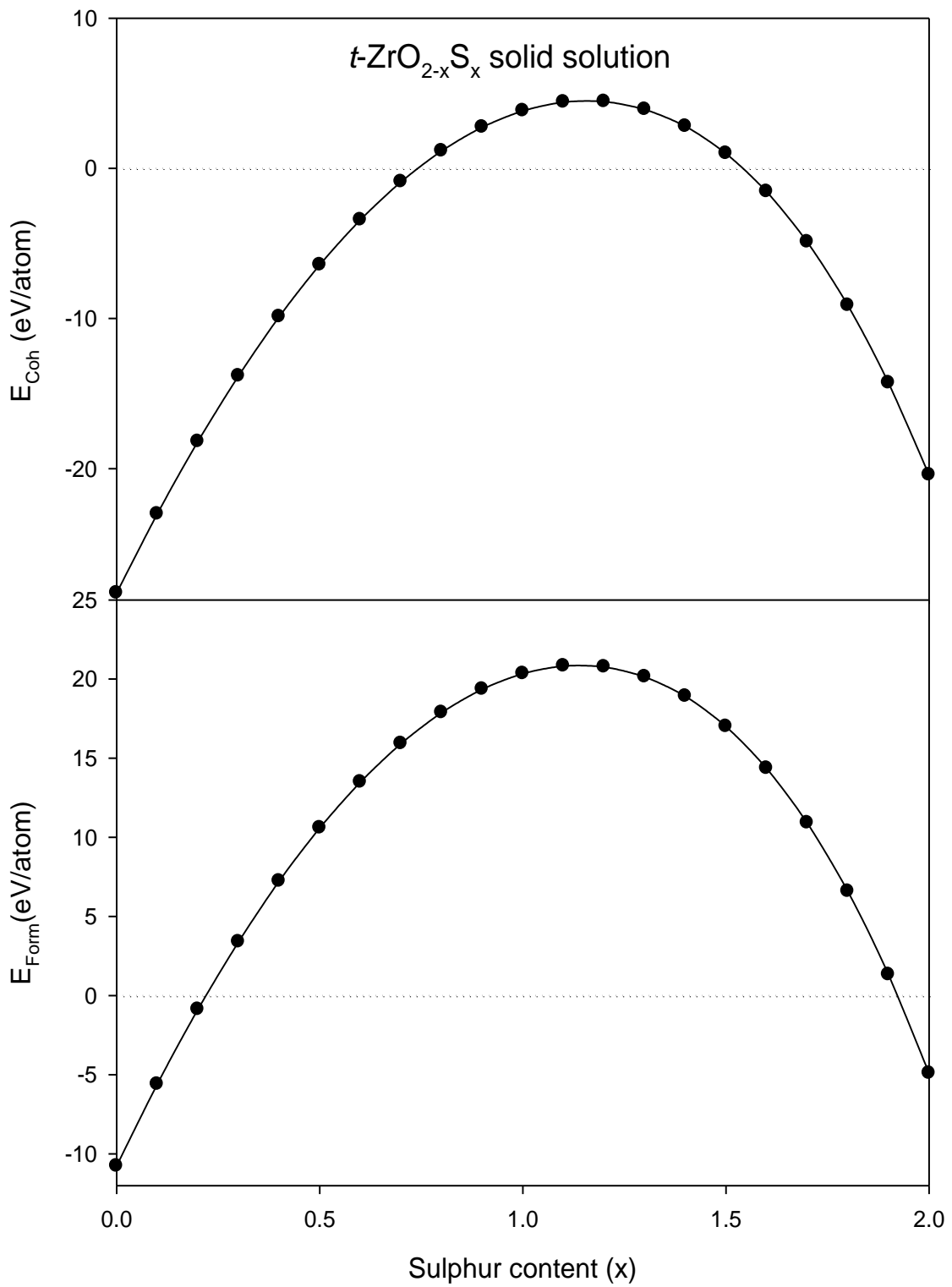


**Figure 13** Variation of the formation energy and cohesive energy with S mole fraction for  $t\text{-ZrO}_{2-x}\text{S}_x$  solid solution

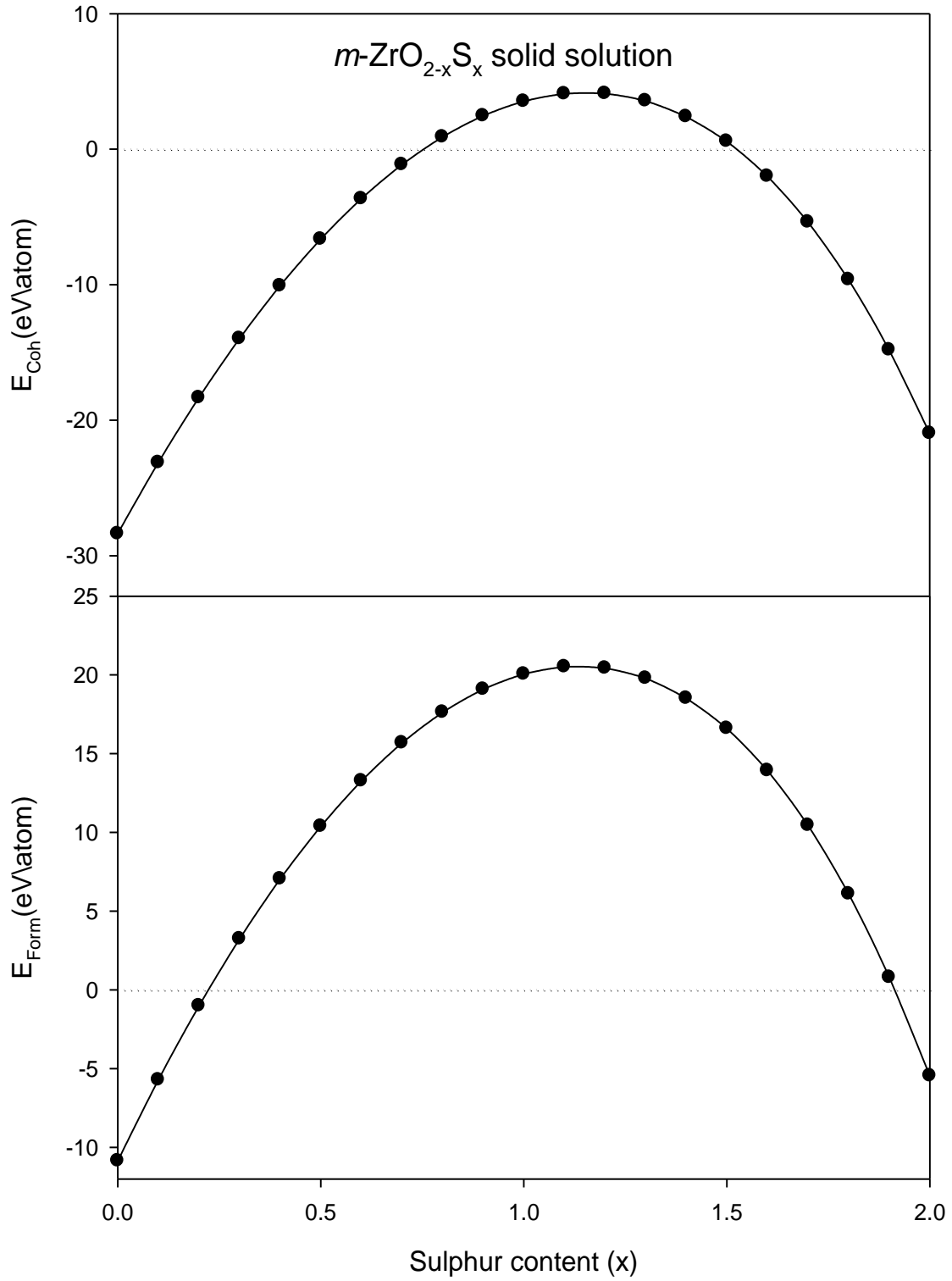


**Figure 14** Variation of the formation energy and cohesive energy with S mole fraction for  $m\text{-ZrO}_{2-x}\text{S}_x$  solid solution

### 3.2.3. Summary of structural properties

The main difference between  $ZrO_{2-x}S_x$  crystals is the fact that,  $t-ZrO_{2-x}S_x$  and  $c-ZrO_{2-x}S_x$  both have one type of O unlike  $m-ZrO_{2-x}S_x$  structure that has two types of oxygen. A rational explanation of increasing difference between monoclinic, tetragonal and cubic phase with an increase of amount of S lies in a specific role the size factor plays of the ions participating in the construction of crystal structure. (i) The change in lattice parameter is proportional to the radius of substituting atom and similar trends were observed for all zirconium dioxide polymorphs as a function of sulphur (ii) The volume expansion rate values for cubic and tetragonal are higher than those of monoclinic structure. (iii) The lattice parameters a and c of  $t-ZrO_2$  tend to increase on addition of sulphur, while its c/a ratio is increasing and decreasing for different concentration. Both lattice parameters as well as c/a are larger than in pure  $t-ZrO_2$ . The axial ratio c/a for tetragonal structure shows the highest value at  $x = 1.1$  and a sudden decrease of c/a values from  $x = 1.1$  is due to a difference in rate at which a and c are increasing. (iv) The anisotropy and the monoclinic angle also showed that b and c of  $m-ZrO_2$  are increasing at different rates. (v) There are significant changes in c/a for  $t-ZrO_2$  and lattice anisotropy (c/b) and monoclinic angle for  $m-ZrO_2$  as a function sulphur. (vi) The cohesive energy, for all three  $ZrO_2$  phases, increases with sulphur content and both cubic and tetragonal become positive in the x ranges from  $x=0.72-1.53$  which suggest phase instabilities in this concentration range. However, they becomes negative again at x ranges from 1.56 to 2.0, which shows a phase stability at this range. Additionally, the highest value of cohesive energy for all three polymorphs as a function of sulphur content is at  $x = 1.1$ . Furthermore, the monoclinic structure showed different behaviour, the energy is positive at  $x = 0.6$  and x ranges from 0.8 to 1.51 which shows phase instability. (vii) The formation energy for all three phases are positive for x ranges from  $x = 0.21$  to  $x = 1.93$  which shows that S has a similar effect on the formation of all three polymorphs. (viii) The highest values of  $t-ZrO_{2-x}S_x$  axial ratio corresponds to the highest values of both it's cohesive and formation energies at  $x = 1.1$  and  $x = 1.2$ . (ix) The highest values of  $m-ZrO_{2-x}S_x$  structure formation and cohesive energies correspond to lowest values of lattice anisotropy and highest values of monoclinic angle.

### 3.3. Density of states

In this chapter, we will theoretically investigate the electronic structure of  $ZrO_{2-x}S_x$  compounds. We calculated the band structures and density of states of the cubic, tetragonal and monoclinic structures, where the lattice constants optimised in this work are used, through the analysis of band structures and density of states, we can find the fundamental role of the individual atoms in the structural instabilities.

The calculated band structures, total density of states (TDOS) and partial density of state (PDOS) for  $m$ - $ZrO_{2-x}S_x$ ,  $t$ - $ZrO_{2-x}S_x$  and  $c$ - $ZrO_{2-x}S_x$  for  $x$  ranges (0 to 0.5), ZrOS and for  $ZrS_2$  structure, were evaluated by interpolation integration method.

#### 3.3.1. Electronic properties

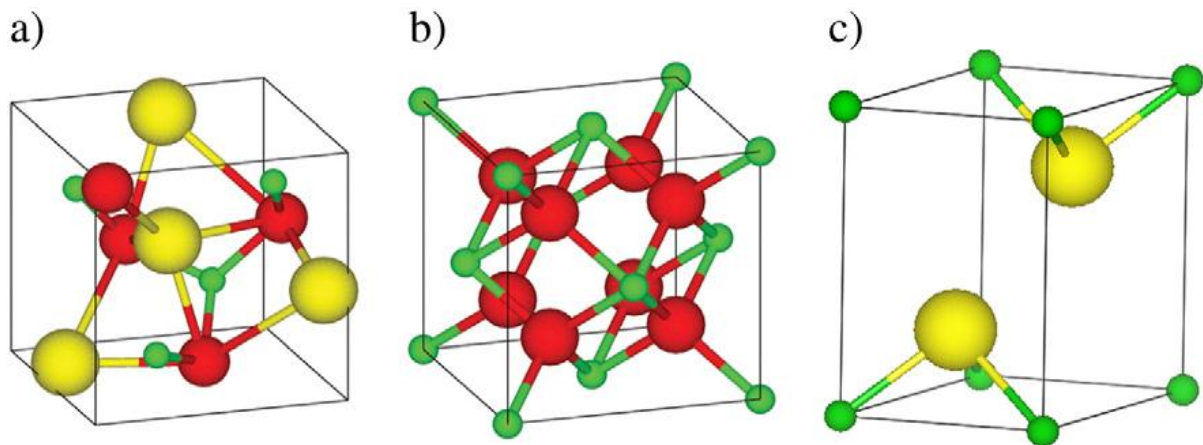


**Figure 15** Crystal structures of (a) ZrOS (b)  $c$ - $ZrO_2$  and (c)  $ZrS_2$

States below the Fermi energy were considered as valence states. Assuming that the 3d and 4s states of Zr can be treated as band states, the 3p states are treated as semi-core states, and all other states with energy lower than 3p states are treated as core states.

It has been observed that the total DOS of all structures displays mostly p like components. In the bottom of the valence band, the DOS is formed by superimposed s and p states. In our case we will only concentrate on the upper valence bands and conduction band for all structures.

**Table 9** Comparison of the band gap values obtained in this work with previous calculations and experiment. Energy values are given in eV

ZrO <sub>2</sub>			
Method	<i>c</i> -ZrO <sub>2</sub>	<i>t</i> -ZrO <sub>2</sub>	<i>m</i> -ZrO <sub>2</sub>
This work			
GGA-WC	3.319	4.019	3.58
Experimental and other theoretical work			
LDA [136]	3.26	4.07	3.58
PP-LDA [137]	3.25	4.10	3.12
PP-GW <sub>0</sub> [137]	5.55	6.40	5.42
Experimental [26]	6.1 - 7.08	5.8 - 6.6	5.83

### ***c*-ZrO<sub>2-x</sub>S<sub>x</sub>**

We have predicted the band gap structures for ZrO<sub>2-x</sub>S<sub>x</sub> along the high symmetry directions in the first Brillouin zone and corresponding density of states from calculated equilibrium lattice constant, calculated energy band structure of *c*-ZrO<sub>2-x</sub>S<sub>x</sub> compounds along X, R, M, G and R which are the high symmetry lines in the first Brillouin zones of *c*-ZrO<sub>2-x</sub>S<sub>x</sub> for all compositions of (x). Both the bottom of the conduction band and the valence band maximum are located at the gamma (g) point in the Brillouin zone which implies that, undoped *c*-ZrO<sub>2</sub> or *c*-ZrO<sub>2-x</sub>S<sub>x</sub> (at x=0) is a direct band insulator. It is seen that the valence band and conduction band do not overlap at E<sub>F</sub> and as a result there is a band gap of 3.319eV, which is in consistent with other theoretical work as seen in Table 9. The calculated band structure and total DOS are compatible with each other. All these mixed crystals have direct band gaps along the gamma direction. The Fermi levels E<sub>F</sub> are chosen to locate at 0 eV and coincide with the upper part of valence band.

We found that calculated band gaps depend strongly on distributions of S electrons in the virtual atom, since sulphur perturbs the conduction band structure. A small percentage of oxygen replacement by sulphur in *c*-ZrO<sub>2</sub> strongly affects the

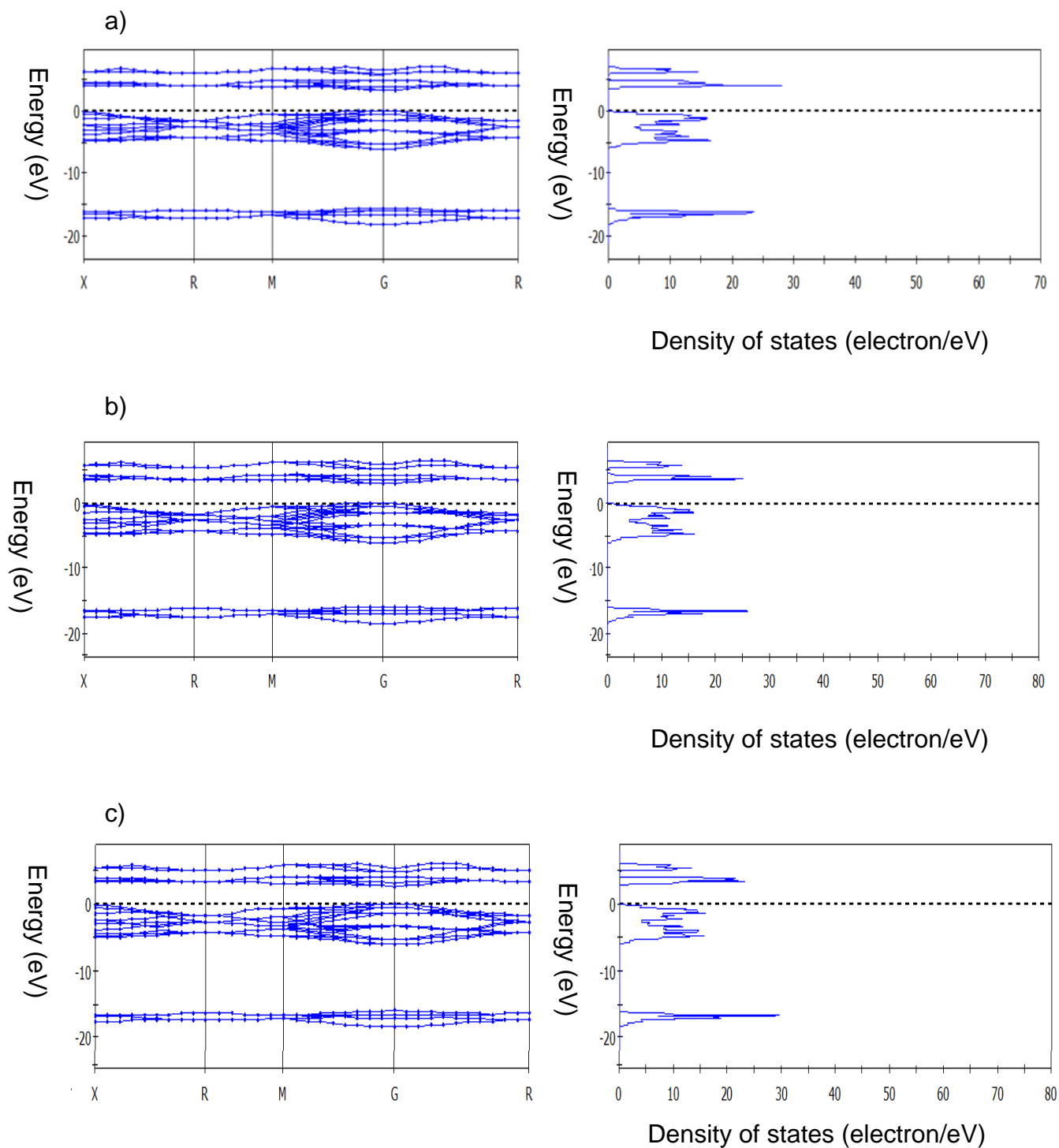


**Figure 16** Total BS and DOSs of the a) unsulphated  $c\text{-ZrO}_2$  and sulphated  $c\text{-ZrO}_2$ , b)  $c\text{-ZrO}_{1.9}\text{S}_{0.1}$  and c)  $c\text{-ZrO}_{1.8}\text{S}_{0.2}$  structures.

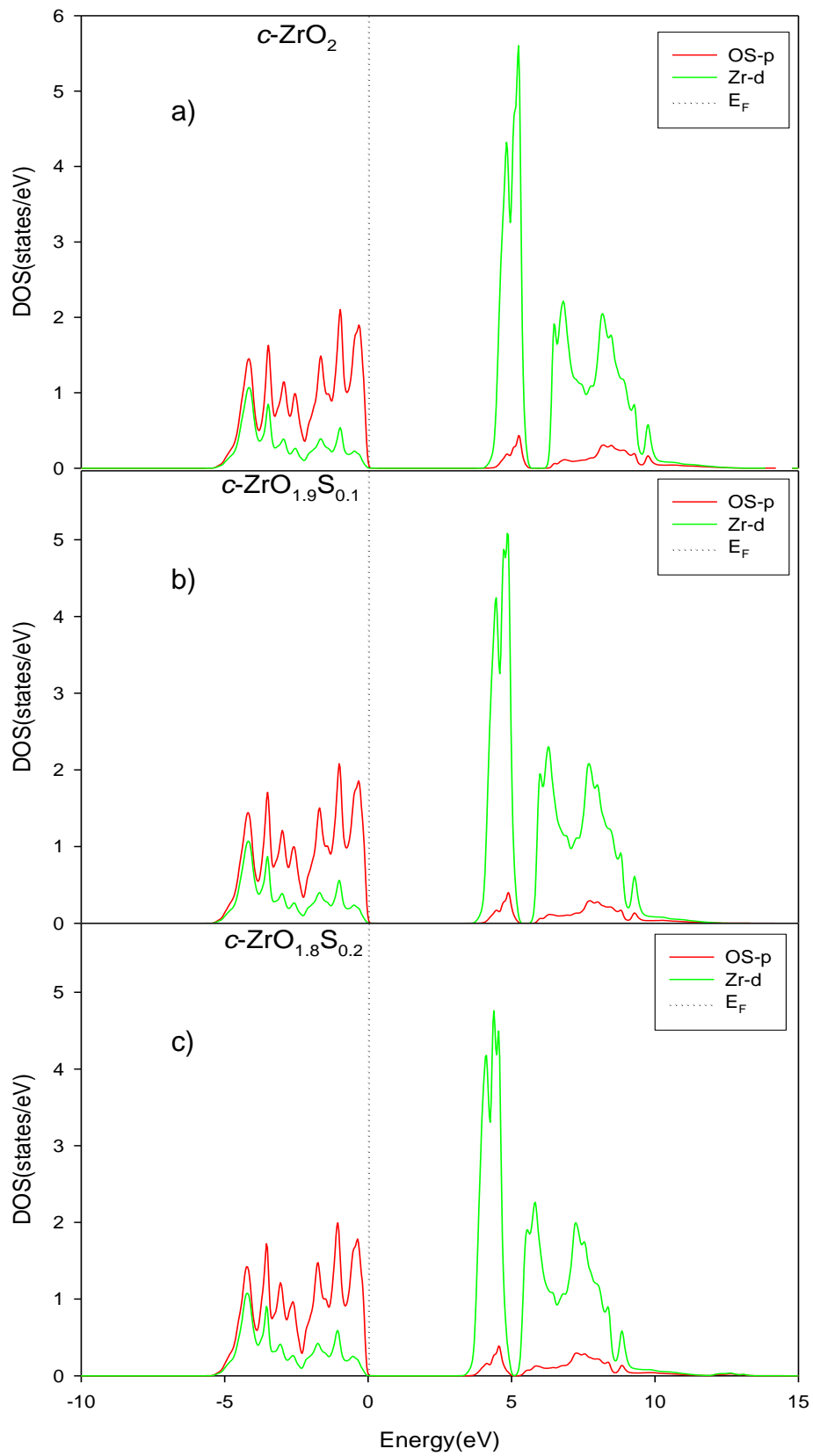


**Figure 17** Partial DOSs of the a) unsulphated  $c\text{-ZrO}_2$ , and sulphated  $c\text{-ZrO}_2$ , b)  $c\text{-ZrO}_{1.9}\text{S}_{0.1}$  and c)  $c\text{-ZrO}_{1.8}\text{S}_{0.2}$  structures.



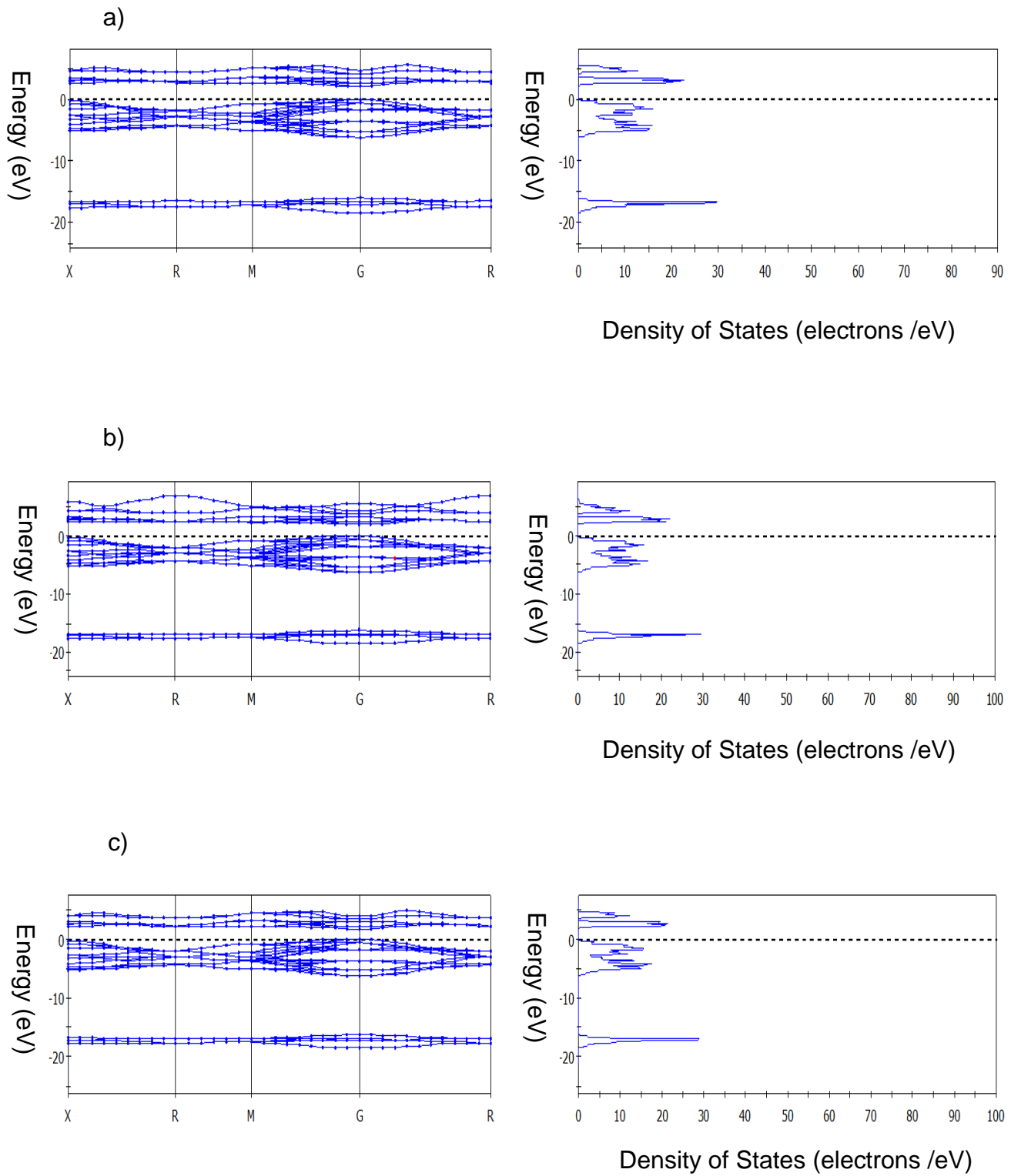


**Figure 18** Total BS and DOSs of the sulphated  $c$ -ZrO<sub>2</sub>, a)  $c$ -ZrO<sub>1.7</sub>S<sub>0.3</sub>, b)  $c$ -ZrO<sub>1.6</sub>S<sub>0.4</sub> and c)  $c$ -ZrO<sub>1.5</sub>S<sub>0.5</sub> structures.

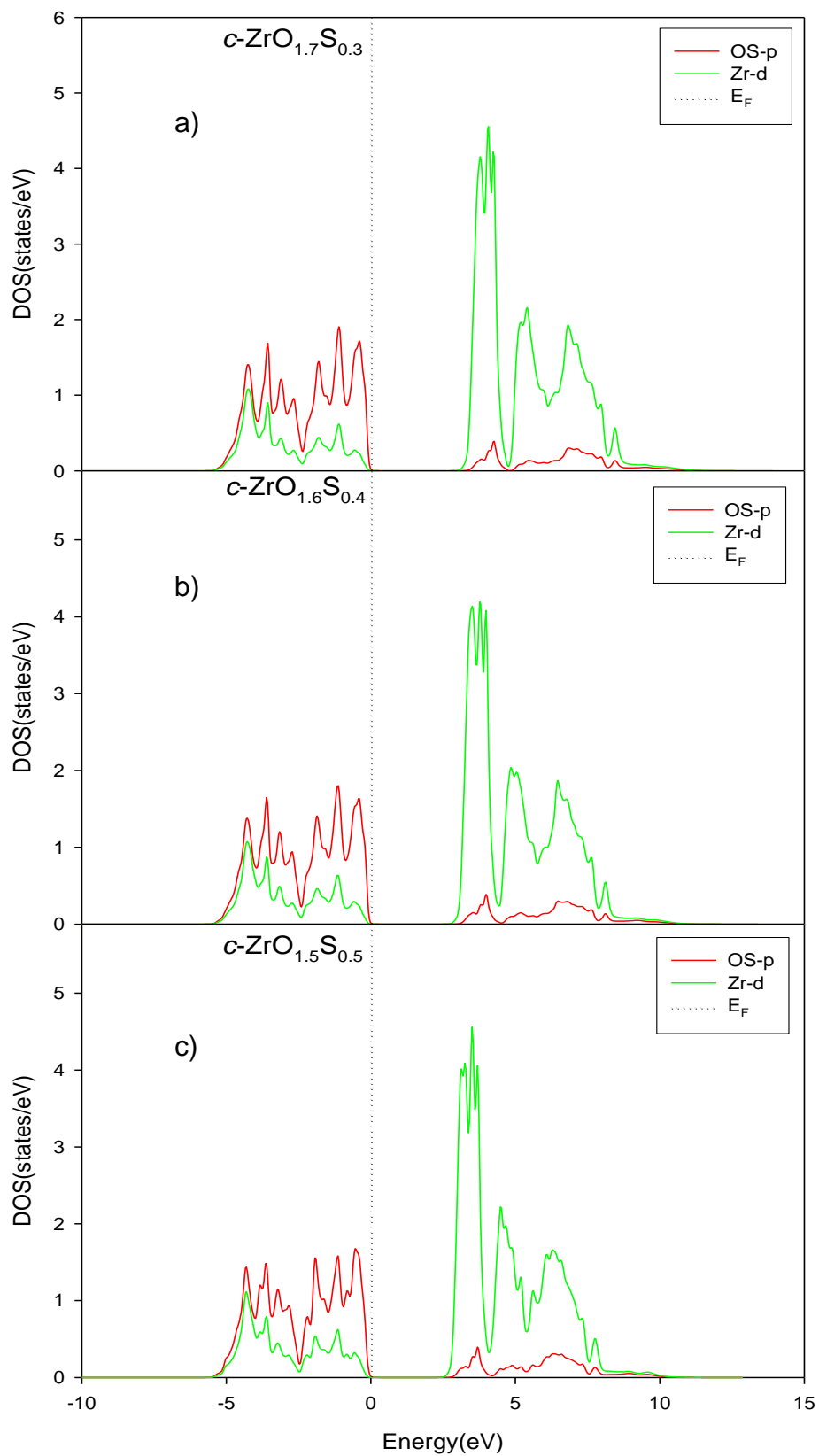


**Figure 19** Partial DOSs of the sulphated  $c\text{-ZrO}_2$ , a)  $c\text{-ZrO}_{1.7}\text{S}_{0.3}$ , b)  $c\text{-ZrO}_{1.6}\text{S}_{0.4}$  and c)  $c\text{-ZrO}_{1.5}\text{S}_{0.5}$  structures.

electronic properties and the increase of S composition leads to a giant band gap reduction due to different atomic properties of  $c\text{-ZrO}_2$  and  $\text{ZrS}_2$  or S and O.

The highly directional coupling between metal d and non-metal p electrons results in a shear-resistive covalent bonding and such bonding gives positive contribution to hardness. Thus, the region which is composed of the strongly hybridized Zr d and O+S p (forming a strong p-d covalent bond), gives a strong positive contribution to hardness and a region above the Fermi level mainly consists of metal-metal bonding which gives negative contribution to the hardness. Figure 16-19 expresses that there is a larger DOS at Fermi for  $\text{ZrO}_2$  than for the other sulphated  $c\text{-ZrO}_2$ , there is maximum shape near Fermi level for each structure.

The states from -5.5eV up to the Fermi level are mainly a mixture of Zr 4d, O and S mixed p states. A significantly strong peak just below the Fermi level shows a large density of states and this result in a large seeback coefficient value, which is related to the fact that electrons are carrier of both electricity and heat. Further insights on the electronic structure of  $c\text{-ZrO}_{2-x}\text{S}_x$  can be gained by analysing the PDOSs near the Fermi level, which are plotted in figure 17 and 19.

Similar features in PDOS are observed for  $c\text{-ZrO}_2$  and  $c\text{-ZrO}_{2-x}\text{S}_x$  (0-0.5) indicating that replacement of O by S will not change the electronic structure, especially the Zr 4d states at Fermi level.

### **ZrOS**

The calculated energy band structure of ZrOS compound along the high symmetry lines in the first Brillouin zone are shown in figure 20. X, R, M, G and R are symmetric points for the Brillouin zone of the ZrOS compound crystal. The Fermi level was chosen to be 0. The valence band of ZrOS is fully occupied and mainly attributed to O 2p and S 3p orbitals, conversely, the empty conduction band formed by antibonding orbitals has mainly by Zr 4d character. The sulphur impurity induces reduction of the band gap to 2.46 eV which correspond to the other reported first principle value of 2.46eV [51] for ZrOS. The reason for such change is the shift of Zr 4d. In order to further investigate contributions of different atom species to the energy level, the partial DOS of ZrOS is also displayed in full. The main difference in

electronic structure between  $ZrO_2$  and  $ZrOS$  is that the S3p valence state appears just above the O2p valence state in the former material. Such appearance will lead us to expectation that the band gap energy of  $ZrOS$  is smaller than the  $ZrO_2$ . This expectation agrees very well with the results that we get for the sulphated and unsulphated structures. A broad and intense structure of two peaks at the valence band near the Fermi energy may be assigned to the S3p - Zr4d.

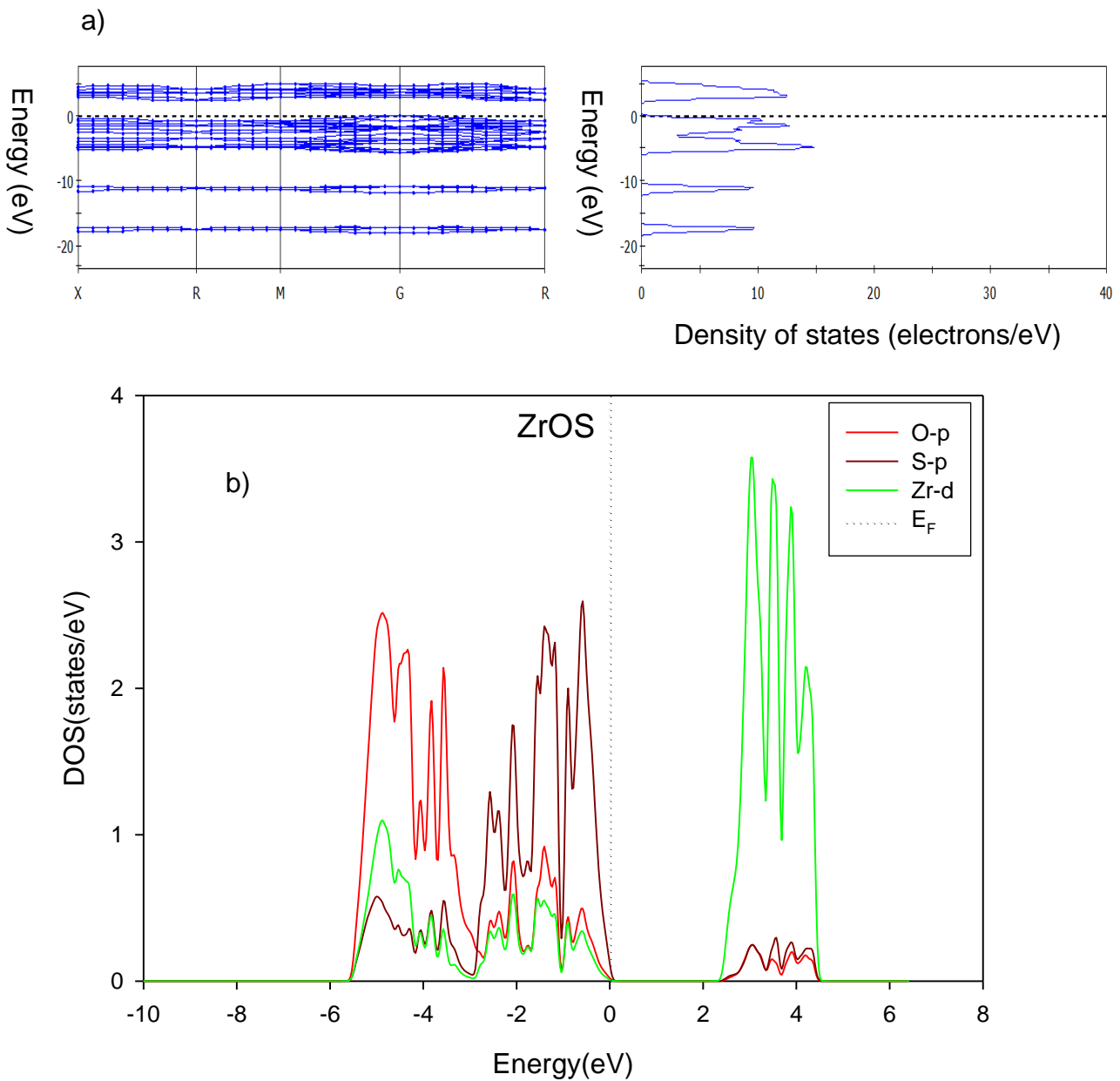


**Figure 20** a) Total BS and DOSs, and b) Partial DOSs of ZrOS.

### ***t-ZrO<sub>2-x</sub>S<sub>x</sub>***

The calculated equilibrium lattice constant  $Z$ ,  $A$ ,  $M$  and  $G$  are the symmetry points for the Brillouin zone of the  $t\text{-ZrO}_{2-x}\text{S}_x$  crystal. The bands and DOS graphs are given in figure 21 and 23. The Fermi level is chosen to be at 0 eV. The fundamental band gaps of  $t\text{-ZrO}_{2-x}\text{S}_x$  ( $x=0-0.5$ ) are indirect from  $Z$  to  $G$  direction. Again two other gaps  $G-G$  and  $A-G$  are close in energy. The highest valence band along  $M-G-Z$  line is nearly dispersionless and would also give to indirect transitions in this energy range. The band gap for pure  $t\text{-ZrO}_2$  ( $t\text{-ZrO}_{2-x}\text{S}_x$  at  $x = 0$ ) is compared with the experimental values and other theoretical work (Table 9). The calculated values in this work are smaller. The reason for this following on the one hand, the experimental values are often determined in  $Z-Z$  direction while our calculation is mainly focussed in directions that give small gaps compared to other directions; on the other hand, it is well known that GGA calculations often largely underestimate band gaps, our results are closer to the theoretical ones as seen from the table but have small differences. This may be attributed to the use of different calculation methods. From the energies of band gaps versus composition of  $t\text{-ZrO}_{2-x}\text{S}_x$ , ( $x=0-0.5$ ), it can be seen that the composition dependence of the band-gap exhibits decreasing trend and the band-gap becomes smaller as we increase the sulphur content. It means that the mixture of O% and S% cannot increase band-gap.

In order to get the nature of the change of the band gap, the total and partial density of  $t\text{-ZrO}_{2-x}\text{S}_x$  are discussed; we find that the character of the TDOS for  $t\text{-ZrO}_{2-x}\text{S}_x$  is quite similar for  $x = (0-0.5)$ .  $E_F$  is located above the minimum of the valley and two sharp peaks for all compounds. The corresponding partial density of  $t\text{-ZrO}_{2-x}\text{S}_x$  are also shown in figure 22 and figure 24, in the case of  $\text{ZrO}_{2-x}\text{S}_x$  at  $x = 0$  the band structures around the Fermi level are derived mainly from O2p and Zr4d orbitals. The contribution from Zr4d is noticeable but an order of magnitude smaller than the contribution of O2p orbitals. The density of states of the conduction band are also derived from O2p and Zr4d only that in the conduction band O2p contribute just a little as compared to Zr4d. The conduction bands are shifted toward the Fermi level with the increase of sulphur content with subsequent increase in conductivity due to the introduction of 3p.

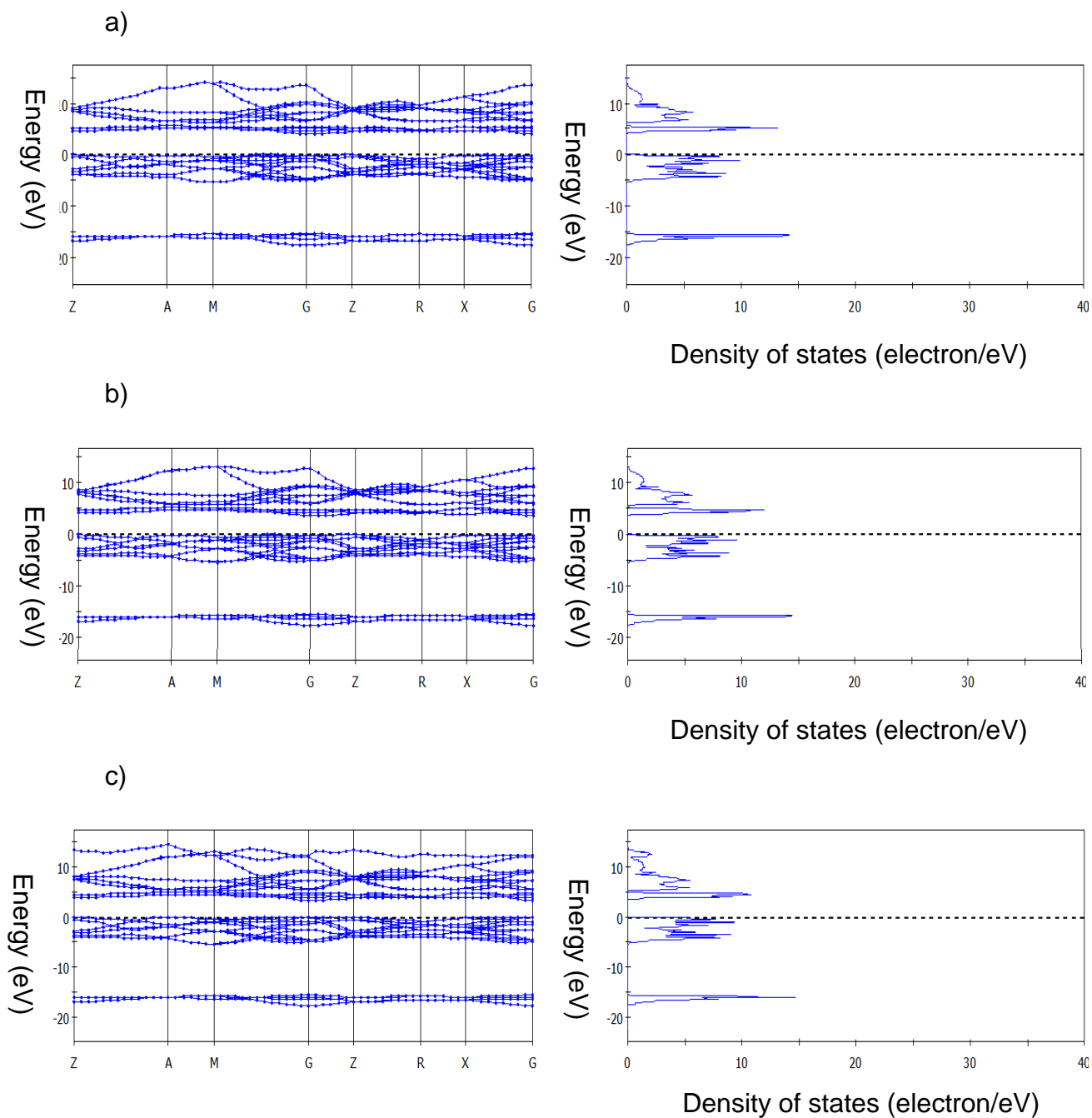


**Figure 21** Total BS and DOSs of the a) unsulphated  $t\text{-ZrO}_2$  and sulphated  $t\text{-ZrO}_2$ , b)  $t\text{-ZrO}_{1.9}\text{S}_{0.1}$  and c)  $t\text{-ZrO}_{1.8}\text{S}_{0.2}$  structures.

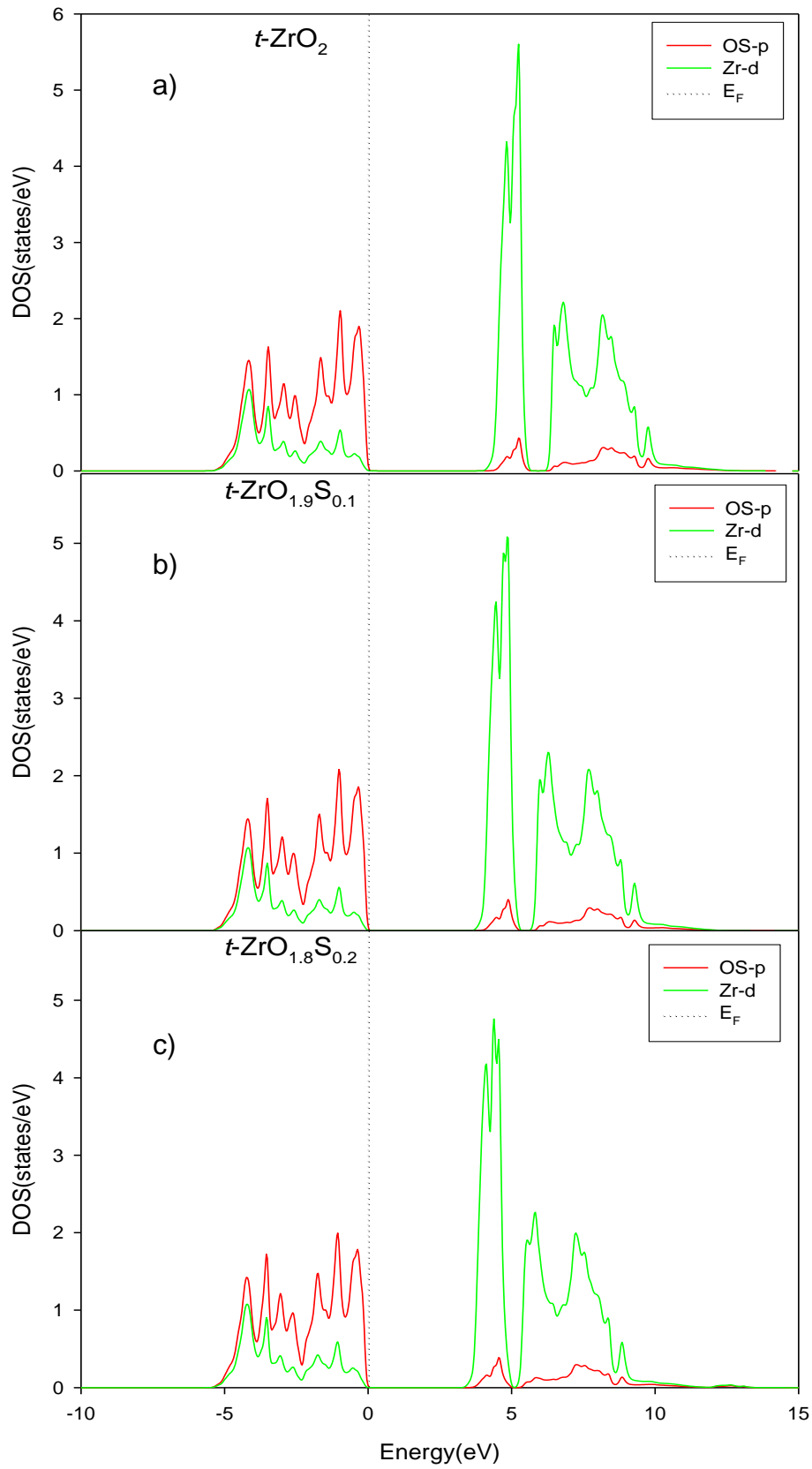


**Figure 22** Partial DOSs of the a) unsulphated  $t\text{-ZrO}_2$  and sulphated  $t\text{-ZrO}_2$ , b)  $t\text{-ZrO}_{1.9}\text{S}_{0.1}$  and c)  $t\text{-ZrO}_{1.8}\text{S}_{0.2}$  structures.

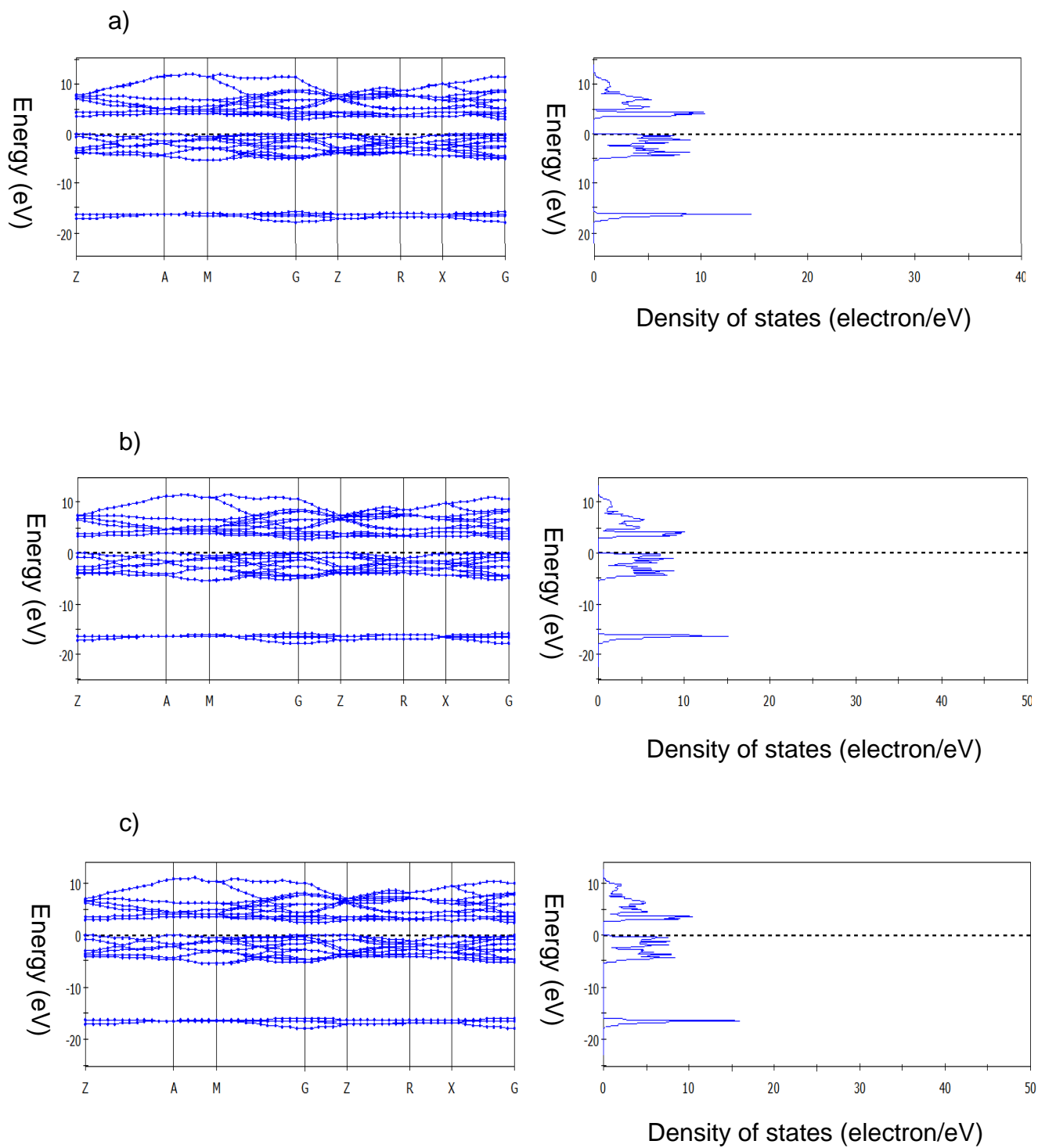


**Figure 23** Total BS and DOSs of the sulphated  $t\text{-ZrO}_2$ , a)  $t\text{-ZrO}_{1.7}\text{S}_{0.3}$ , b)  $t\text{-ZrO}_{1.6}\text{S}_{0.4}$  and c)  $t\text{-ZrO}_{1.5}\text{S}_{0.5}$  structures.



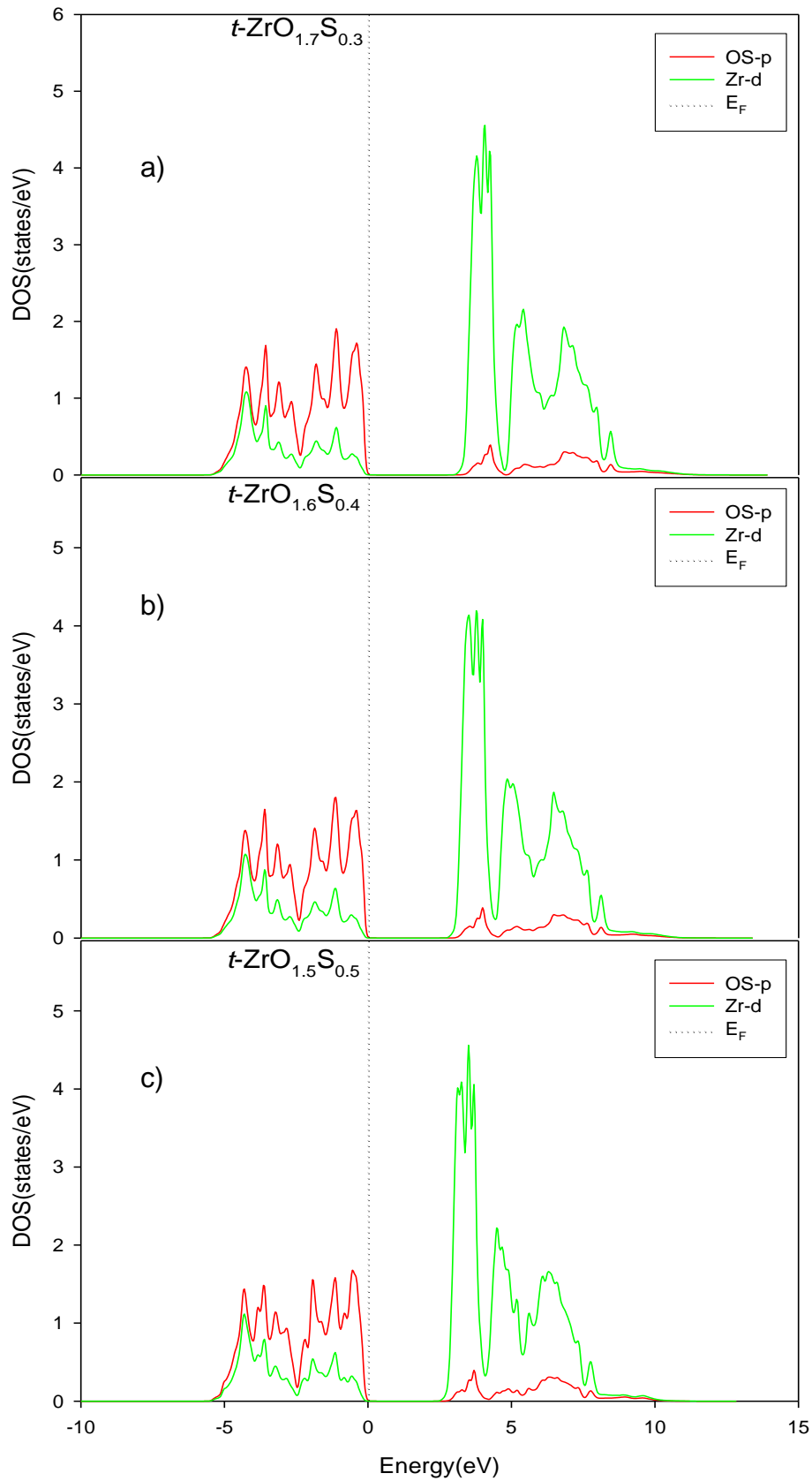


**Figure 24** Partial DOSs of sulphated  $t\text{-ZrO}_2$ , a)  $t\text{-ZrO}_{1.7}\text{S}_{0.3}$ , b)  $t\text{-ZrO}_{1.6}\text{S}_{0.4}$  and c)  $t\text{-ZrO}_{1.5}\text{S}_{0.5}$  structures.

### $m\text{-ZrO}_{2-x}\text{S}_x$

The energy band structures of  $m\text{-ZrO}_{2-x}\text{S}_x$  along with high-symmetry point of the Brillouin zone, are show in figure 25 and 27. The zero of the energy is arbitrary taken at Fermi level (dashed line).

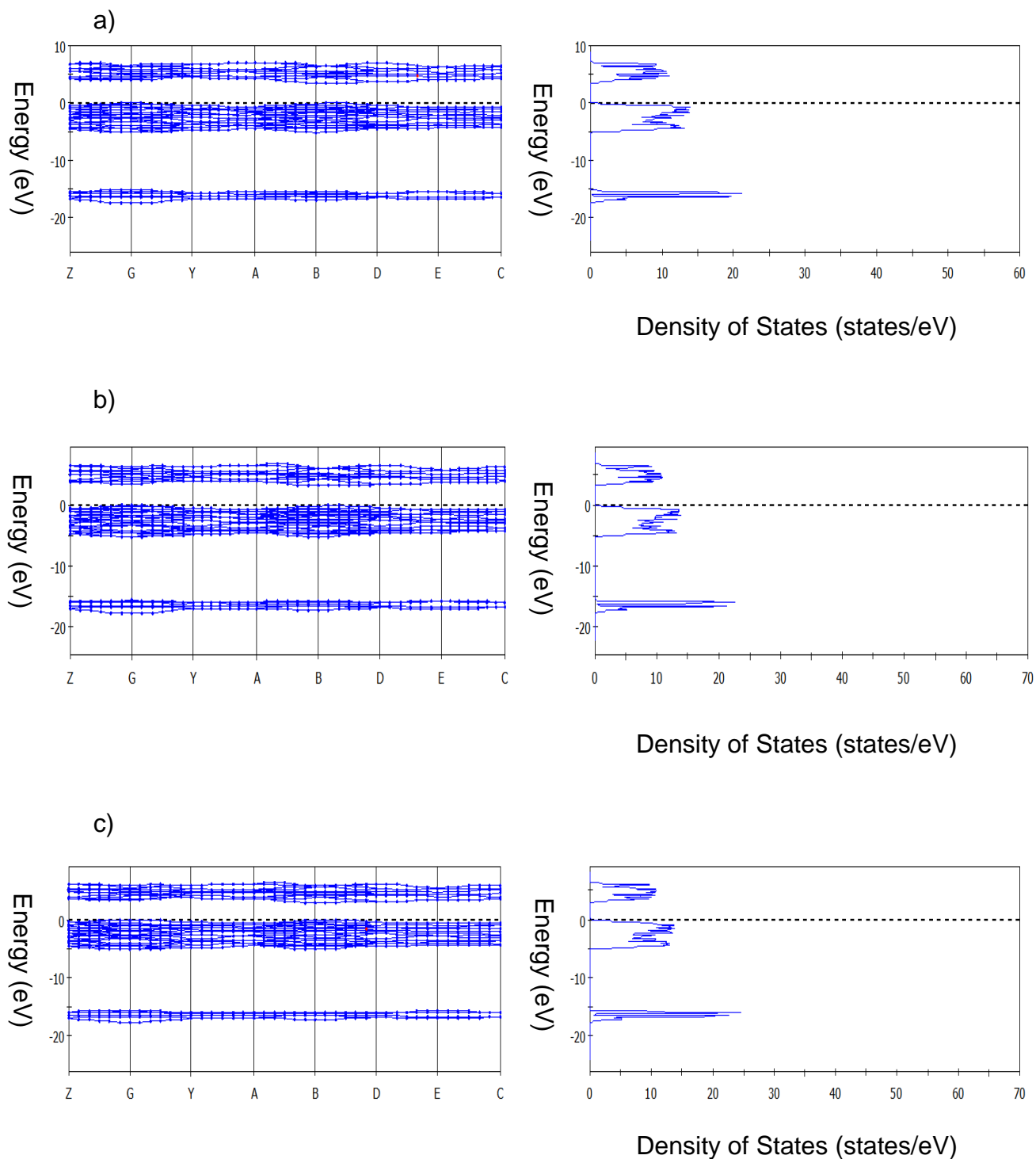


**Figure 25** Total BS and DOSs of the a) unsulphated  $m\text{-ZrO}_2$  and sulphated  $m\text{-ZrO}_2$ , b)  $m\text{-ZrO}_{1.9}\text{S}_{0.1}$  and c)  $m\text{-ZrO}_{1.8}\text{S}_{0.2}$  structures.

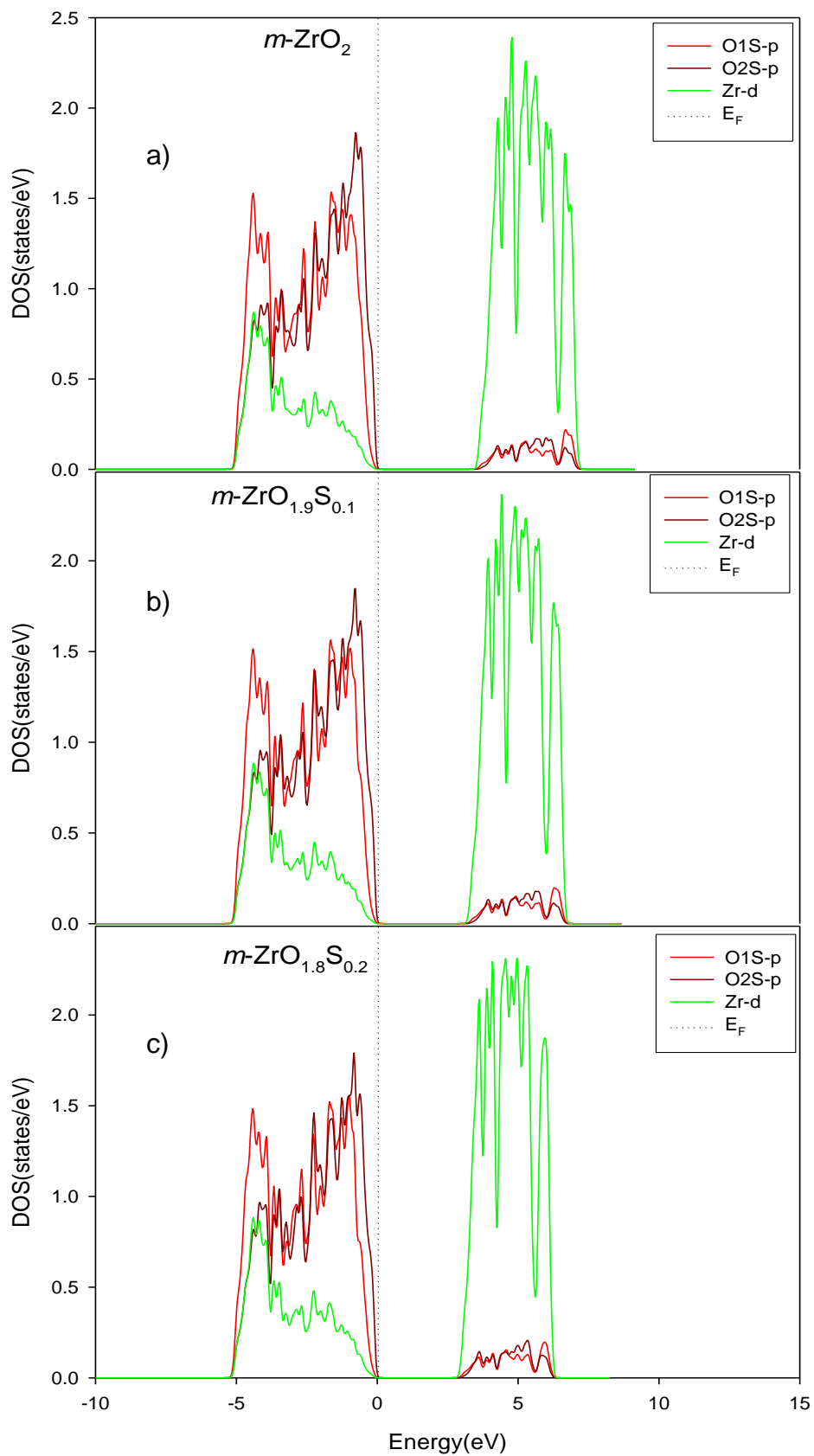


**Figure 26** Partial DOSs of the a) unsulphated  $m$ -ZrO<sub>2</sub> and sulphated  $m$ -ZrO<sub>2</sub>, b)  $m$ -ZrO<sub>1.9</sub>S<sub>0.1</sub> and c)  $m$ -ZrO<sub>1.8</sub>S<sub>0.2</sub> structures.

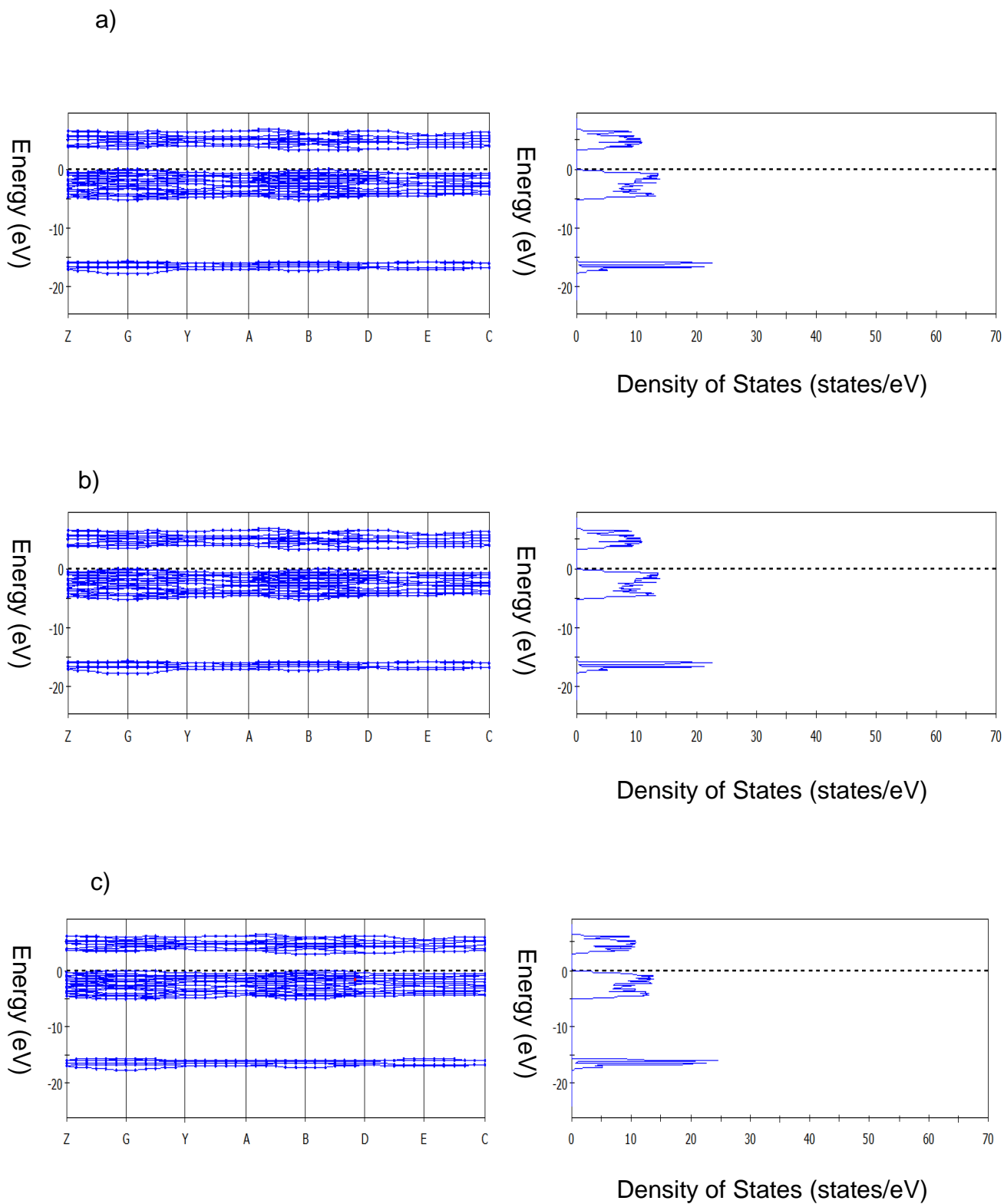


**Figure 27** Total BS and DOSs of the sulphated  $m$ - $\text{ZrO}_2$ , a)  $m$ - $\text{ZrO}_{1.7}\text{S}_{0.3}$ , b)  $m$ - $\text{ZrO}_{1.6}\text{S}_{0.4}$  and c)  $m$ - $\text{ZrO}_{1.5}\text{S}_{0.5}$  structures.

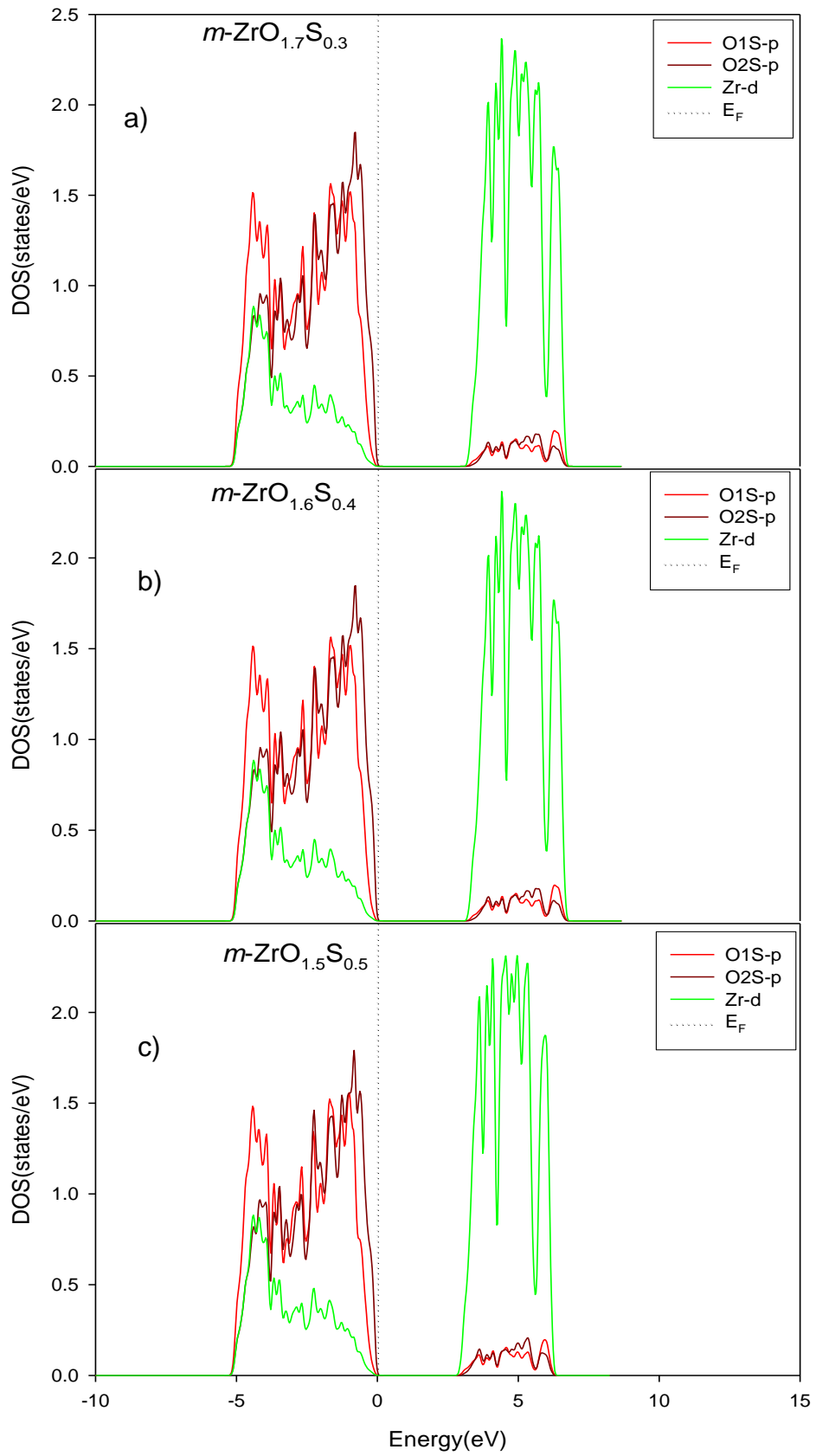


**Figure 28** Partial DOSs of the sulphated  $m\text{-ZrO}_2$ , a)  $m\text{-ZrO}_{1.7}\text{S}_{0.3}$ , b)  $m\text{-ZrO}_{1.6}\text{S}_{0.4}$  and c)  $m\text{-ZrO}_{1.5}\text{S}_{0.5}$  structures.

The top of the valence band and the bottom of the conduction are composed of O2p and Zr4d (figure 26 and 28) for  $m\text{-ZrO}_{2-x}\text{S}_x$  at  $x = 0$ , the calculated band structure shows that monoclinic  $\text{ZrO}_2$  has an indirect band structure because the valence band maxima and conduction band exhibit minima at G and B, respectively. In addition, the indirect band gap from G to B is calculated to be about 3.58 eV, which agrees very well with other theoretical values as seen in Table 9. The energy band -5.63 eV to 0 eV at figure 23 and figure 25 consists of O2p states that show two sharp peaks due to strong localised two O atoms in  $m\text{-ZrO}_2$ , with some admixture of Zr4d states. This shows that  $m\text{-ZrO}_2$  has some features of covalent bonding, comparing the  $m\text{-ZrO}_2$  and  $m\text{-ZrO}_{2-x}\text{S}_x$  for  $x > 0$  compounds. As we know that replacement of O by S adds the orbitals of S to the electronic structure, we note that S3p electrons substantially narrow the band gap, moreover there is a larger contribution of Zr4d in the conduction band than of the mixed O and Sp orbitals.

### **ZrS<sub>2</sub>**

The figure 29 shows the graphical presentation of band structure and density of states (DOS) of  $\text{ZrS}_2$ . The uppermost valence band is mainly constructed of sulphur 3p bands, however these states are mixed with components of zirconium 4d, 5s and 5p orbitals, which suggests that there are strong covalent interactions between sulphur atoms and zirconium atoms. The 4d band is mainly located in the conduction band which is above  $E_F$ . The conduction band as seen from the total density of states consists of two peaks which Yang et al. [138] indicated could be ascribed as  $t_{2e}$  and  $e_g$ -type bands, respectively. Moreover the first peak is almost divided into two peaks due to distortion of octahedral position where the zirconium atom resides. The zirconium 4d bands are mixed with a considerable number of sulphur 3p orbitals. This provides another piece of evidence of strong Zr-S covalent bonding. Wertheim et al. reported the valence band structure of  $\text{ZrS}_2$  by XPS measurement [139]. The three peaks in the valence band have also been explained by their measurement. Those experimental results are quite similar to our calculated results. In the present calculations the main component of bands from 0 to 6eV are sulphur 3p orbitals but the considerable number of zirconium orbitals are also involved in the same band. The lowest energy at about -5eV is attributed to the strong covalent interaction between sulphur 3p and zirconium 5sp. The middle energy peak is also of bonding states formed by mixture of zirconium 4d and 5sp and sulphur 3p. But the peak of

highest energy is of a non-bonding states; it is essentially composed of sulphur 3p orbitals. There is a strong admixture of zirconium 4d and 5sp and sulphur 3p orbitals i.e a strong covalent bonding between zirconium and sulphur atoms is characteristic of  $ZrS_2$ .

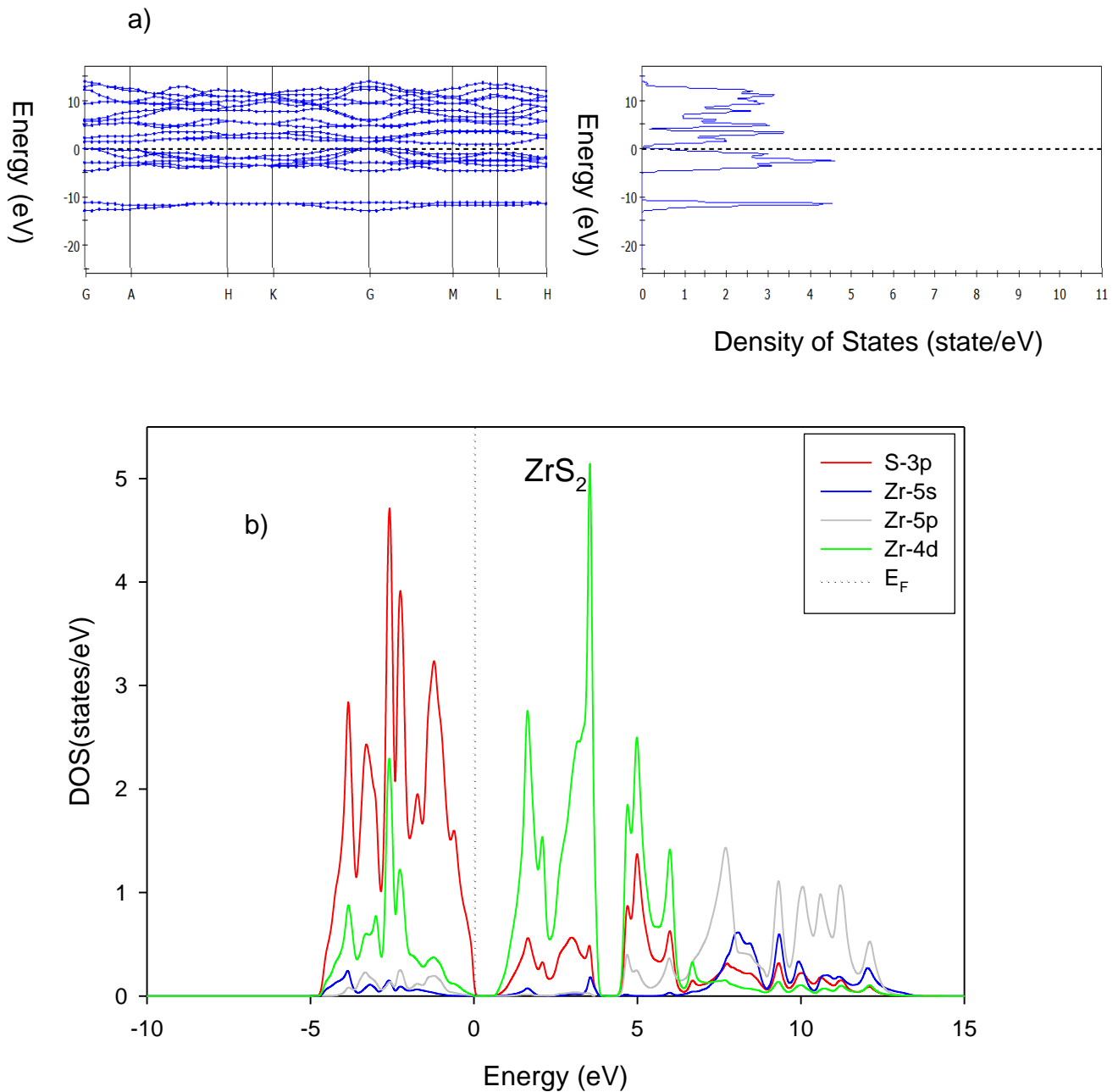


**Figure 29** a) Total BS and DOSs, and b) Partial DOSs and of the  $ZrS_2$  structures.

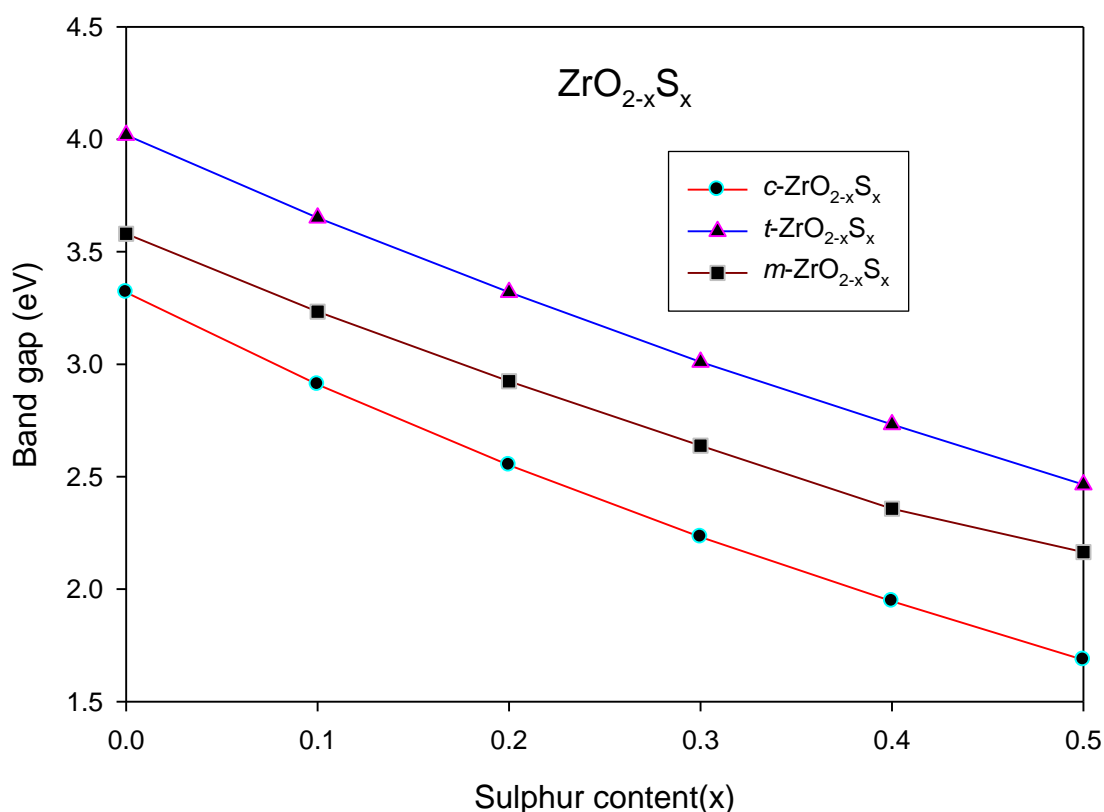


**Figure 30** Variation of bandgaps of (*ctm*)-ZrO<sub>2-x</sub>S<sub>x</sub> solid solution for x=(0-0.5)

### 3.3.2. Summary of electronic properties

The band structure, total DOS and PDOS of Zr states, O states and S states for the three oxides / sulphides at different sulphur contents are shown in figure 20 to figure 28. The main features can be summarized as follows: (i) at the low energy side of the DOS, the O2s S3s and Zr4p states contribute to the DOS peaks for the three oxides. As the sulphur contents increases, these peaks become more dispersive and have a tendency of shifting to the lower energy, (ii) some strong peaks occur at the same energy in the PDOS of a particular Zr atom, a particular O atom and a particular S atom, indicating that the Zr, O and S atoms are bonded. However, the predicted band gap is smaller than the experimental value of 5.2eV from table 9, which means that our results underestimate the real band gap value of *m*-ZrO<sub>2</sub>. The DOS peaks split into smaller peaks and become narrower as the addition of S increases. This shows that there is an increase of charge overlap and delocalization among the bonded atoms in the system, (iii) With the increment of S, there are some differences in the DOS of the O states for the three oxides. This is due to the



differences in their local molecular packing. The same is true of the DOS of the Zr states, (iv) in the conduction band region, the DOS peaks of the Zr and O states in  $m\text{-ZrO}_2$  shift to lower energy under compression. It may be inferred that the interactions between the O and Zr states become stronger as the sulphur contents increases. However, for  $t\text{-ZrO}_2$  and  $c\text{-ZrO}_2$ , the case is quite the contrary and (v) overall, the DOS shape of  $m\text{-ZrO}_2$  in the upper valence band is identical with that of its O states. The rigidity of the DOS of O states thus implies that the modifications in the DOS of the oxide are mainly due to the changes in the DOS of O states. The same is true of  $t\text{-ZrO}_2$  and  $c\text{-ZrO}_2$ . (vi) In all structures presented the energy band gap is complicated, mainly due to impurity inducing energy levels of hybrid orbital when forming S-Zr bonds or O-S bonds. (vii) The total electron density of states (DOS) for  $\text{ZrO}_2$  with different S concentration levels presented in figure16-figure 29 indicates detailed band structure variation with sulphur concentration. By close examination of bandwidth sequence we note that the band gaps are 3.319, 2.910, 2.551, 2.232, 1.946 and 1.686 for  $c\text{-ZrO}_{2-x}\text{S}_x$ , 4.019, 3.651, 3.320, 3.010, 2.732 and 2.465 for  $t\text{-ZrO}_{2-x}\text{S}_x$  and 3.580, 3.234, 2.924, 2.638, 2.358 and 2.165 eV for  $m\text{-ZrO}_{2-x}\text{S}_x$  at  $x=(0, 0.1, 0.2, 0.3, 0.4, 0.5)$ , this implies that weaker covalency in this order, the strength of covalency may be related to the calculation results of cohesive energies, which are -28.283, -22.94, -18.123, -13.753, -9.850 and -6.387 eV, -28.287, -23.017, -18.192, -13.825, -9.88 and -6.425 and -28.377, -23.133, -18.337, -13.979, -10.076 and -6.638 for  $c\text{-ZrO}_{2-x}\text{S}_x$ ,  $t\text{-ZrO}_{2-x}\text{S}_x$  and  $m\text{-ZrO}_{2-x}\text{S}_x$ , respectively.

### 3.4. Mechanical properties

In the present work, we performed systematic first principles calculations of elastic parameters of  $\text{ZrO}_{2-x}\text{S}_x$  single crystals, such as the elastic constants  $C_{ij}$ , the bulk moduli  $B$  and the shear moduli  $G$ . These are widely used for describing the elastic behaviour of materials. First  $C_{ij}$ 's are evaluated by calculating the stress tensors on different deformations applied to the equilibrium lattice of cubic, tetragonal and monoclinic unit cell. Then the dependence of the resulting energy change from the deformation is determined and the constants are evaluated in a standard way. Elastic constant  $C_{ij}$  could provide important information for mechanical stability, elastic moduli, and thus hardness of materials.

It is of vital importance to theoretically investigate the mechanical properties of  $\text{ZrO}_{2-x}\text{S}_x$  for the entire  $x$  range in order to search for optimum  $\text{ZrO}_{2-x}\text{S}_x$  structure. To

study the effect of S on mechanical properties of  $ZrO_2$  structure the elastic constants of various  $ZrO_{2-x}S_x$  structure are calculated in accordance to the method by Nye, the main idea is presented as follows; the elastic stiffness constants were calculated by stress-strain method. Both stress and strain have a tensile and three components, giving six components in total. The linear elastic constants form a 6 x 6 symmetric matrix, having 27 different components, such that  $\sigma_i = C_{ij}\varepsilon_j$  for small stress  $\sigma$  and strain  $\varepsilon$ . properties such as bulk modulus, Young modulus, and Poisson's ratio may be computed from the values of  $C_{ij}$ .

### 3.4.1. Single crystal elastic constants

#### **c-ZrO<sub>2</sub>**

Table 10 summarise the single crystal elastic constants of *c*-ZrO<sub>2</sub>. The elastic constants of *c*-ZrO<sub>2</sub> are compared with experimental and calculated values available from other reports. Since *c*-ZrO<sub>2</sub> belongs to the cubic system of space group *Fm3m*, the number of independent elastic constant can be as small as three. The derived elastic constant for *c*-ZrO<sub>2-x</sub>S<sub>x</sub> at  $x = 0$  or *c*-ZrO<sub>2</sub>, are  $C_{11}$ ,  $C_{12}$  and  $C_{44}$ . It could be seen clearly from Table 10 that the calculated elastic constant of the *c*-ZrO<sub>2</sub> phase from the present study are in better agreement with corresponding calculated values than experimental values in the literature for instant, the  $C_{11}$ ,  $C_{12}$  and  $C_{44}$  are calculated to be 541, 101 and 70 GPa, respectively, which match well with values from different literature results as seen in Table 10. The *c*-ZrO<sub>2</sub> is mechanically stable before we introduce S. Since all mechanical stability criteria for cubic structure are met,  $C_{11}$ ,  $C_{12}$  and  $C_{44}$  are found to be positive as seen in equation 2.38.

**Table 10** calculated, theoretical and experimental elastic constant for *c*-ZrO<sub>2</sub>.Exp.: experimental data; WC: present work; HF: Hartree-Fock; TB: tight binding; PIB: potential-induced breathing; LD: lattice dynamics

parameter	Exp [140]	WC	HF [141]	TB [133]	PIB [142]	LD [143]	LD [128]
$C_{11}$ (GPa)	417	541	628	543	548	455	409
$C_{12}$ (GPa)	82	101	19	193	158	64	53
$C_{44}$ (GPa)	47	70	82	57	180	63	60
$B_0$ (GPa)	194	248	222	310	288	194	171

Table 11 lists the predicted  $C_{ij}$   $c\text{-ZrO}_2$  as a function of sulphur content based on GGA-WC. Since the elastic constant  $C_{44}$  of  $c\text{-ZrO}_{2-x}\text{S}_x$  is directly linked to the mechanical stability of crystals, it will be presented on figure 30 along with  $E$  and  $C'$ .

**Table 11** Variation of lattice independent elastic constant for  $c\text{-ZrO}_{2-x}\text{S}_x$  for  $0 \leq x \leq 2$

x	$C_{11}$ (GPa)	$C_{44}$ (GPa)	$C_{12}$ (GPa)
0	541.3	69.5	101.5
0.1	487.9	60.9	89.9
0.2	452.7	47.5	83.2
0.3	419.8	37.4	77.2
0.4	394.1	29.6	71.6
0.5	372.3	18.6	68.4
0.6	483.8	15.7	74.6
0.7	320.3	38.1	60.0
0.8	296.9	5.9	56.9
0.9	283.6	2.2	56.4
1	266.6	2.4	49.0
1.1	260.0	0.9	51.0
1.2	244.3	-0.6	48.3
1.3	241.2	-1.1	48.0
1.4	238.7	-1.3	48.3
1.5	235.0	-1.2	48.0
1.6	231.1	-1.7	47.3
1.7	324.0	-2.6	54.6
1.8	337.8	-11.8	70.5
1.9	216.2	14.9	51.1
2	201.4	-4.5	53.0

As shown in Table 11, the trends of  $C_{11}$  and  $C_{12}$  elastic constants decrease with  $x$  composition ranging between 0 and 0.5, thus decreasing the mechanical stability of  $c\text{-ZrO}_{2-x}\text{S}_x$  ( $0 \leq x \leq 0.5$ ). However beyond  $x = 0.5$  there is no particular trend on relationship between an increase in  $x$  composition and  $C_{11}$  and  $C_{12}$  elastic constants. The  $C_{11}$  and  $C_{12}$  at  $x = 0.6$  gives higher values compared to  $x = 0.5$ , and from  $x = 0.7$

composition, they start to decrease. At  $x = 1.7$  and  $1.9$ .  $C_{11}$  is over 300 and  $C_{12}$  for  $x = 0.8$  is 70.5, which is higher compared to all other composition after  $x = 0.5$ . All the compositions predicts  $C_{11}$  is larger than  $C_{12}$  which means the mechanical stability criterion for cubic structure  $C_{11} + C_{12} > 0$  is met and all the values for  $C_{11}$  and  $2C_{12}$  are all positive as evident from the table.

### ***t*-ZrO<sub>2-x</sub>S<sub>x</sub>**

The *t*-ZrO<sub>2-x</sub>S<sub>x</sub> at  $x = 0$  results are summarised in Table 12 which list the values of elastic constants, some literature data are listed for  $C_{11}$ ,  $C_{33}$ ,  $C_{44}$ ,  $C_{66}$ ,  $C_{12}$ ,  $C_{13}$  and  $B_0$  [133, 142, 144, 145, 142, 143, 146]. The agreement with experiment is not as good as for the lattice parameters, but is in the range normally found in this comparison, averaging 10%-20%. Some comments on the effect of difference may be appropriate. The effect is small for  $C_{11}$ ,  $C_{33}$  and  $C_{13}$ , it is not that big as compared to other elastic constant as seen in Table 12.

Table 13 shows the variations of elastic constant *t*-ZrO<sub>2</sub> with S concentrations  $x$ . The constant  $C_{11}$  decreases from  $x = 0 - 0.6$  and increases from  $x = 0.6 - 0.8$  and then decreases until it becomes negative.

**Table 12** calculated, theoretical and experimental elastic constant for *t*-ZrO<sub>2</sub>; see key of table 11. (c) Indicates that the elastic constant is given in the cubic axes, (t) in primitive tetragonal axes, and no indication means chosen set of axes unknown.

parameter	Exp [144]	Exp [145]	WC	TB [133]	PIB [142]	LD [143]	LD [128]	LD [146]
$C_{11}$ (GPa)	340	327	366	366	465	395(c)	416(c)	263
$C_{33}$ (GPa)	325	264	342	286	326	326(c)	234(c)	262
$C_{44}$ (GPa)	66	59	22	78	101	42(c)	39(c)	55.9
$C_{66}$ (GPa)	95	64	163	88	156	56(c)	73(c)	44
$C_{12}$ (GPa)	33	100	219	180	83	26(c)	30(c)	15
$C_{13}$ (GPa)	160	62	64	80	49	105(c)	68(c)	72
$B_0$ (GPa)	183	149	193	190	179	148	134	122

$C_{33}$  decreases from  $x = 0 - 0.3$  and increases at 0.4,  $C_{33}$  is larger at 0.8 than  $C_{11}$ ,  $C_{44}$ ,  $C_{66}$ ,  $C_{12}$  and  $C_{13}$ .  $C_{44}$  is positive only for composition  $x = 0.2$  and 0.8.  $C_{12}$  decreases a

little from  $x = 0.4$  and increases a little and increases at  $x = 0.7$  to  $0.8$ .  $C_{13}$  and  $C_{66}$  both remain almost unchanged except at  $x = 0.8$ . The criteria as seen in equation 2.39 for  $t\text{-ZrO}_2$  as a function of S structure are not met for  $C_{11}-C_{12}$  from  $x>0.45$  and it has a minimum value at  $x = 1.0$ ,  $C_{11}+C_{33}-2C_{13}$  is negative at  $x = 1.0, 1.2, 1.3, 1.5, 1.6, 1.7, 1.8$  and  $1.9$ . The criterion is not met at this point and all values of the  $2(C_{11}+C_{33}+2C_{12}+4C_{13})$  criterion are positive and it has a maximum value at  $0.8$  as shown in figure 31.

**Table 13** Variation of independent lattice elastic constant for  $t\text{-ZrO}_{2-x}\text{S}_x$  for  $0 \leq x \leq 2$

x	$C_{11}$ (GPa)	$C_{33}$ (GPa)	$C_{44}$ (GPa)	$C_{66}$ (GPa)	$C_{12}$ (GPa)	$C_{13}$ (GPa)
0	365.5	341.9	22.2	163.9	219.5	64.5
0.1	333.6	271.2	26.0	149.3	216.5	74.7
0.2	320.3	259.7	-4.8	133.6	199.0	36.9
0.3	282.3	220.4	-51.7	122.4	183.5	58.2
0.4	232.7	309.0	-117.3	114.5	171.5	41.1
0.5	200.7	203.8	-154.6	105.9	233.6	55.5
0.6	138.7	226.1	-1.5	97.2	248.5	63.8
0.7	156.8	178.2	6.5	92.8	195.3	38.8
0.8	369.1	512.0	-45.8	165.0	468.3	232.6
0.9	-32.2	187.8	-298.4	82.6	377.4	55.4
1	-123.7	145.3	-169.3	77.9	483.9	56.8
1.1	-36.4	147.4	-293.6	74.8	380.7	47.0
1.2	-101.1	138.9	-149.8	71.5	347.2	42.3
1.3	-87.4	154.3	-352.1	69.7	403.8	58.0
1.4	-80.5	287.5	-329.8	68.0	383.4	71.1
1.5	-31.5	140.6	-272.7	66.1	343.7	60.3
1.6	-76.1	159.1	-378.9	64.5	406.0	67.2
1.7	-66.1	141.7	-343.3	63.0	366.7	52.1
1.8	-72.1	142.2	-394.3	61.6	393.9	57.2
1.9	-51.6	140.6	-199.9	59.1	413.3	62.5
2	-72.1	150.7	-359.3	57.4	377.4	35.4

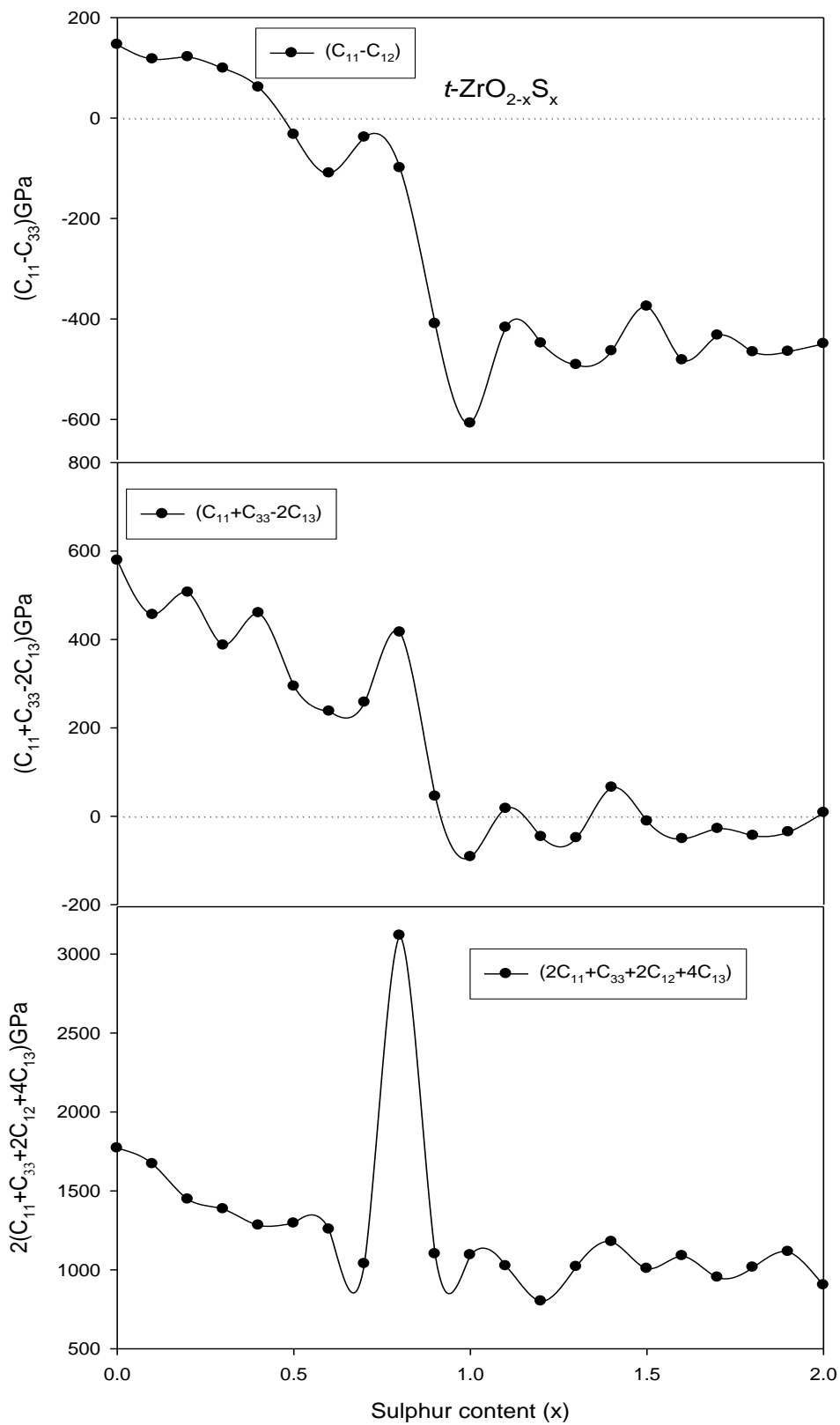


**Figure 31** Variation of the tetragonal structure mechanical stability criterion with S mole fraction for  $t\text{-ZrO}_{2-x}\text{S}_x$  solid solution

### *m*-ZrO<sub>2-x</sub>S<sub>x</sub>

The calculation of elastic constants of the *m*-ZrO<sub>2-x</sub>S<sub>x</sub> phase became complicated. It belongs to a monoclinic system of space group *P*2<sub>1</sub>/*c*. The number of independent elastic constants can be as large as thirteen. The elastic constants are computed in basis indicated in chapter 2, they are in fair agreement with experimental data for diagonal part. Off-diagonal terms are less accurate, in particular *C*<sub>13</sub>, and the *C*<sub>15</sub>=1, 2, 3 (wrong signs or magnitudes or both); however this is still in line with other published results by other researchers. From the Table 14 since *C*<sub>11</sub>(*C*<sub>12</sub>,*C*<sub>33</sub>) of *m*-ZrO<sub>2-x</sub>S<sub>x</sub> are slightly larger than the other elastic constant, it has a pronounced elastic anisotropy.

As the sulphur molar fraction increases from 0.0 to 2.0, we note from Table 15 that the *C*<sub>11</sub>,*C*<sub>22</sub> and *C*<sub>33</sub> elastic constants change by larger amount, while *C*<sub>13</sub> changes by a smaller amount, from 82GPa at *x* = 0.0 to 78GPa for *x* = 0.6, *C*<sub>44</sub> start at 87GPa (*x* = 0.0), decreases to 41.99GPa and increases to 49.56GPa (*x* = 2).

**Table 14** calculated, theoretical and experimental independent elastic constant for *m*-ZrO<sub>2</sub>. PAW: projected augmented wave. See key of Table 11

parameter	Exp [144]	Exp [147]	WC	paw [148]	PIB [142]	LD [143]
<i>C</i> <sub>11</sub> (GPa)	361	358	335	337	353	347
<i>C</i> <sub>22</sub> (GPa)	408	426	378	351	434	364
<i>C</i> <sub>33</sub> (GPa)	258	240	244	268	272	274
<i>C</i> <sub>44</sub> (GPa)	99.9	99.1	87	79.1	156	88
<i>C</i> <sub>55</sub> (GPa)	81.2	78.7	76	70.3	123	108
<i>C</i> <sub>66</sub> (GPa)	126	130	125	114	192	122
<i>C</i> <sub>12</sub> (GPa)	142	144	162	155	233	164
<i>C</i> <sub>13</sub> (GPa)	55.0	67.0	82.5	84.3	138	102
<i>C</i> <sub>15</sub> (GPa)	-21.3	-25.9	31.6	25.9	61	28
<i>C</i> <sub>23</sub> (GPa)	196	127	146	153	191	156
<i>C</i> <sub>25</sub> (GPa)	31.2	38.3	-6.91	-4.28	-44	-17
<i>C</i> <sub>35</sub> (GPa)	-18.2	-23.3	6.77	1.91	59	11
<i>C</i> <sub>46</sub> (GPa)	-22.7	-38.8	-15.0	-14.6	-35	-44
<i>B</i> <sub>0</sub> (GPa)	201	189	184	193	182	194

**Table 15** Variation of calculated independent elastic constant for  $m\text{-ZrO}_{2-x}\text{S}_x$  for  $0 \leq x \leq 2$

S (x)	$C_{11}$ (GPa)	$C_{22}$ (GPa)	$C_{33}$ (GPa)	$C_{44}$ (GPa)	$C_{55}$ (GPa)	$C_{66}$ (GPa)	$C_{12}$ (GPa)	$C_{13}$ (GPa)	$C_{15}$ (GPa)	$C_{23}$ (GPa)	$C_{25}$ (GPa)	$C_{35}$ (GPa)	$C_{46}$ (GPa)
0	335.9	377.8	244.0	87.1	75.5	125.1	162.6	82.5	31.6	146.1	-6.9	6.8	-15.0
0.1	307.9	356.7	256.2	76.4	65.6	117.8	136.8	86.8	37.9	107.1	-3.4	16.3	-13.6
0.2	293.9	324.7	272.5	71.0	63.9	114.5	119.3	88.9	29.5	108.7	-3.6	3.3	-14.4
0.3	270.3	295.4	275.4	68.2	57.0	67.3	118.8	83.9	36.6	110.2	-3.8	14.5	-2.9
0.4	251.9	313.2	218.3	63.3	52.9	92.0	111.8	76.1	25.1	125.1	-6.2	0.3	-14.0
0.5	230.3	259.7	214.2	59.1	45.5	84.6	92.9	72.6	23.5	97.1	-6.2	-2.3	-11.9
0.6	227.2	243.9	237.8	56.0	47.8	80.7	90.3	78.3	22.8	93.2	-2.2	3.4	-11.0
0.7	195.2	244.1	211.8	51.0	48.6	79.4	89.8	63.8	20.9	86.3	-1.2	2.1	-9.8
0.8	69.7	219.1	192.6	48.2	37.7	71.8	77.6	58.3	19.0	83.6	-3.3	-2.0	-8.9
0.9	177.6	208.1	182.6	45.1	32.7	66.2	72.3	56.3	20.2	77.8	-1.6	-1.2	-7.1
1	173.4	199.2	178.7	43.3	30.1	65.8	71.5	57.2	16.2	77.2	-3.5	-2.3	-7.1
1.1	173.6	194.9	159.0	42.6	29.0	62.3	71.0	54.4	15.8	76.6	-4.4	-1.7	-7.7
1.2	166.1	186.7	162.6	42.0	28.9	61.9	66.0	50.9	16.6	72.3	-2.1	-0.2	-7.1
1.3	168.8	180.2	262.5	40.0	24.8	60.4	59.6	85.2	13.8	74.9	2.2	-8.1	-7.9
1.4	144.0	178.4	109.6	41.5	27.0	60.7	66.6	26.9	11.5	78.8	0.9	-19.7	-7.9
1.5	138.2	211.7	87.9	34.9	27.9	43.8	90.8	20.0	30.3	114.2	-11.6	29.0	3.0
1.6	150.5	154.1	112.4	37.5	30.9	54.9	64.6	39.0	6.8	78.4	0.5	-16.9	3.8
1.7	151.9	156.0	100.0	34.0	28.0	57.1	64.7	37.6	17.1	78.8	-2.0	6.5	-2.7
1.8	145.8	153.7	113.4	39.0	27.5	58.0	65.7	32.5	16.1	76.7	-1.0	-0.2	-5.0
1.9	298.4	170.3	180.1	47.3	49.1	65.8	89.7	111.6	-61.8	86.1	-25.6	-0.4	-9.8
2	300.1	169.6	179.6	49.6	51.1	69.1	92.2	60.9	-44.0	72.6	-20.6	10.2	-10.9

$C_{55}$  on the other hand, decreases from 75.5GPa ( $x = 0.0$ ) to 24.5GPa ( $x = 1.3$ ) and increases to 51.102GPa. While  $C_{66}$  has a minimum at  $x = 1.5$  (43.8GPa).  $C_{12}$  varies from 162.55GPa down to 59.58GPa ( $x = 1.3$ ) and then up 92.70GPa ( $x = 2.0$ ).  $C_{13}(C_{23})$  oscillates with minimum value of 19.92GPa(72.34GPa) at  $x = 1.5$  ( $x = 1.2$ ).  $C_{25}(C_{35}, C_{46})$  also oscillates with the maximum values 2.227( 28.97, 3.789)GPa at  $x = 1.3$  ( $x = 1.5$ ,  $x = 1.6$ ) as seen in figure 32 and 33.



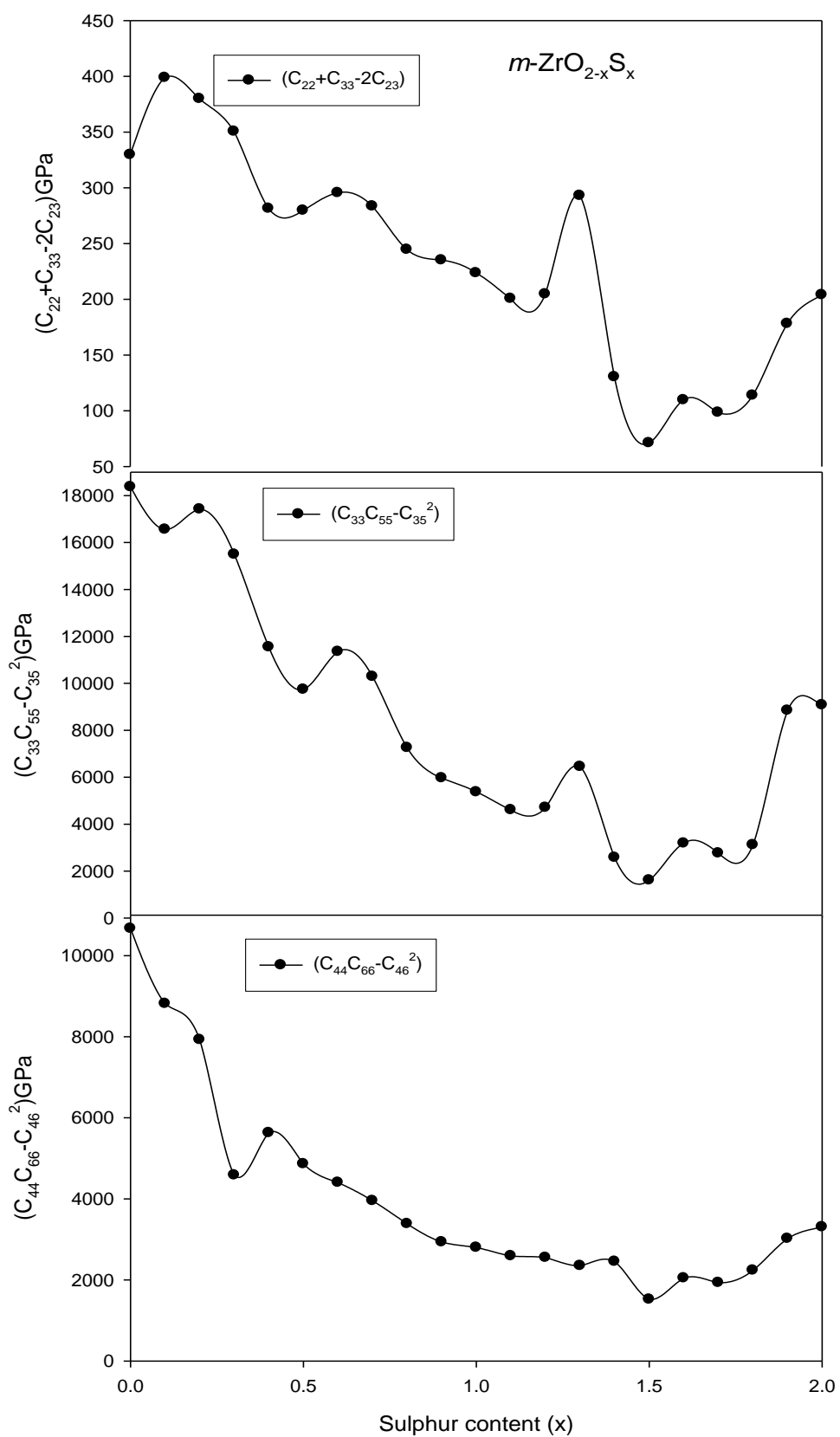


**Figure 32** Variation of the monoclinic structure mechanical stability criterion with S mole fraction for  $m\text{-ZrO}_{2-x}\text{S}_x$  solid solution.

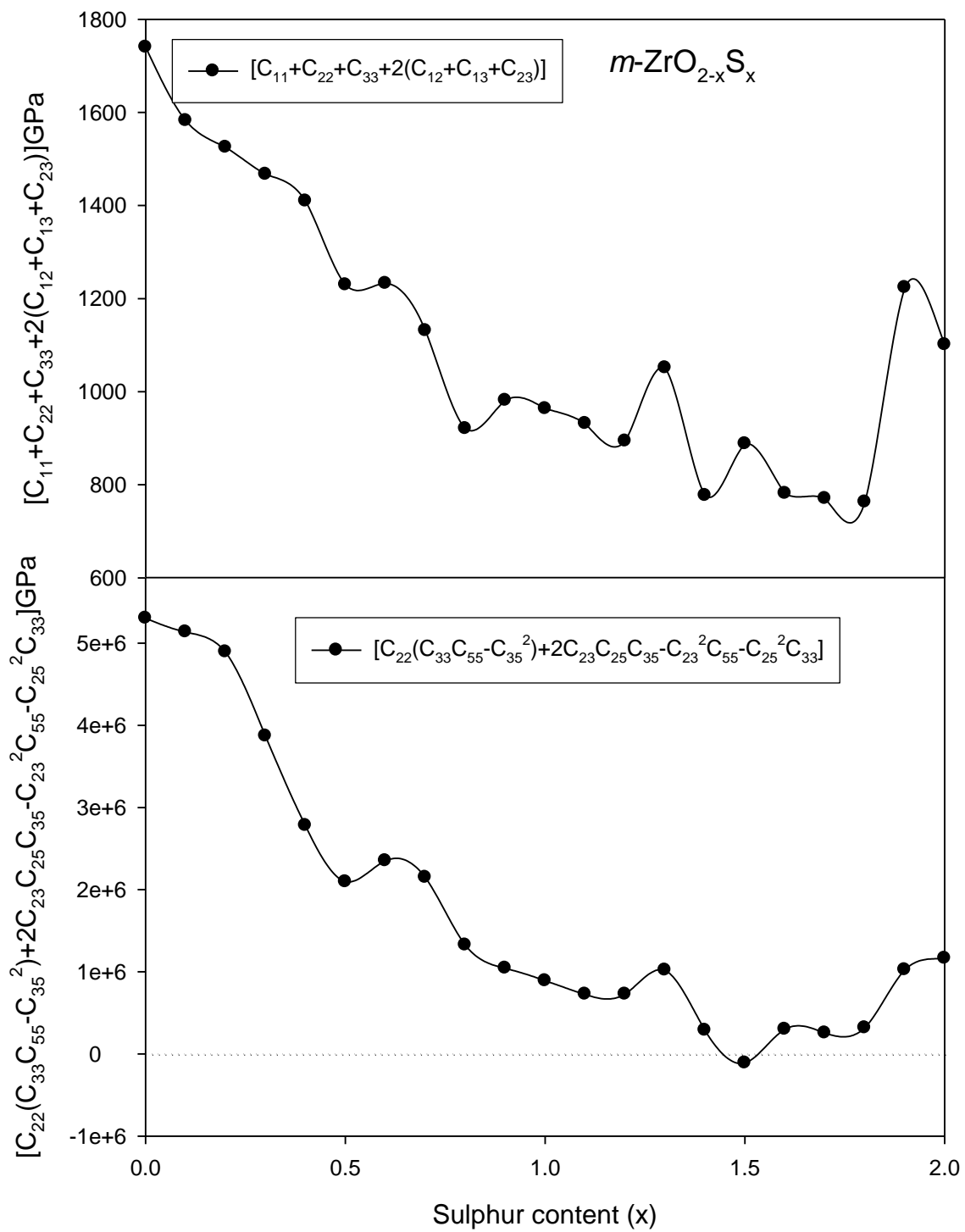


**Figure 33** Variation of the monoclinic structure mechanical stability criterion with S mole fraction for  $m\text{-ZrO}_{2-x}\text{S}_x$  solid solution.

### 3.5.2. Polycrystalline elastic properties

It is of engineering importance to find out the elastic moduli of polycrystalline materials. Accordingly, the bulk modulus ( $B$ ) is derived through fitting to the Murnaghan equation of state (EOS) [149].

$$E(V) = E_0 + \frac{B_0 V}{B_1(B_1 - 1)} \left[ B_1 \left(1 - \frac{V_0}{V}\right) - 1 + \left(\frac{V_0}{V}\right)^{B_1} \right]$$

The shear modulus ( $G$ ) of polycrystalline material could be approximated from elastic constants of single crystals through Voigt's and Reuss' approximations for maximum values of moduli as well as Hill's approximation for average values respectively. Voigt assumes that the ratio of strain is uniform everywhere, while Reuss assumes the stress in polycrystalline aggregate to external stress is uniform [118]. Voigt's ( $G_V$ ) and Reuss' ( $G_R$ ), and Hill's ( $G_H$ ) approximations are given by equations 2.27, 2.28 and 2.29. As a results figure 34-46 summarise the calculated  $B$ ,  $G$ ,  $E$  and  $\nu$  of  $ZrO_{2-x}S_x$  polymorphs with different  $x$  ranges. It can be observed that elastic moduli of polycrystalline  $ZrO_{2-x}S_x$  at  $x = 0$  for three polymorphs from the present study are in good agreement with experimental and theoretical data available in literature.

If tetragonal shear modulus ( $C'$ ), trigonal shear moduli ( $C_{44}$ ) and young modulus ( $E$ ) are negative, it implies that  $c$ - $ZrO_{2-x}S_x$  is mechanical unstable. all the values are reported in figure 34.

$C_{44}$  is negative for the range  $1.1 \leq x \leq 1.85$  implying mechanical instability within this range.  $C'$  is positive for the whole range of  $x$ . It is interesting to note that at the region where  $C'$  is positive it correlates with mixing enthalpy in terms of stability, and the  $E$  follow the similar trend to that of  $C'$ . As a result  $c$ - $ZrO_{2-x}S_x$  is more stable at  $x = 0.6$  as indicated by the higher  $C'$  in figure 34.  $C'$  is more reliable compared to  $C_{44}$  in terms of predicting mechanical stabilities. The highest value of  $C'$  for sulphated  $cZrO_2$  correspond to the highest value of  $E$  and high values  $C_{11}$  and  $C_{22}$  at 0.6, which shows that the  $c$ - $ZrO_{2-x}S_x$  is more stable at  $x = 0.6$  than for the other sulphated  $c$ - $ZrO_2$ .

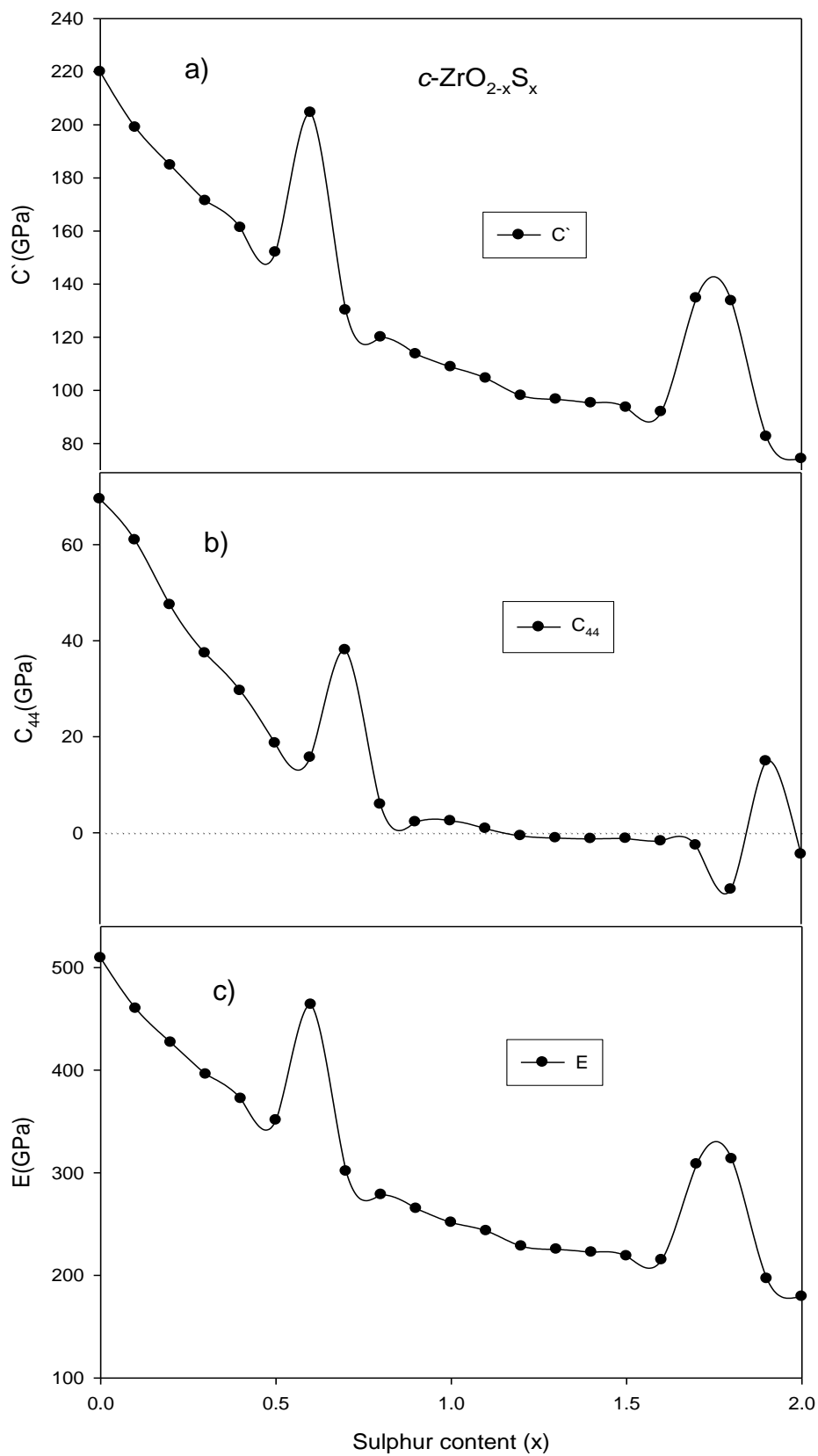


**Figure 34** Variation of the a)  $C'$ , b)  $C_{44}$  and c)  $E$  of S mole fraction for  $c\text{-ZrO}_{2-x}\text{S}_x$  solid solution.

The Poisson's ratios of cubic  $ZrO_2$  as a function of S contents ranges from 0 - 0.21 which shows that all the forces acting on the structure as a function of sulphur content are not central, though the values of U are lowest at  $x = 0.6$  and at  $x = 1.7$ , and the U value is highest at  $x = 2.0$ . The highest value of U correlates with the lowest value of  $C'$ .

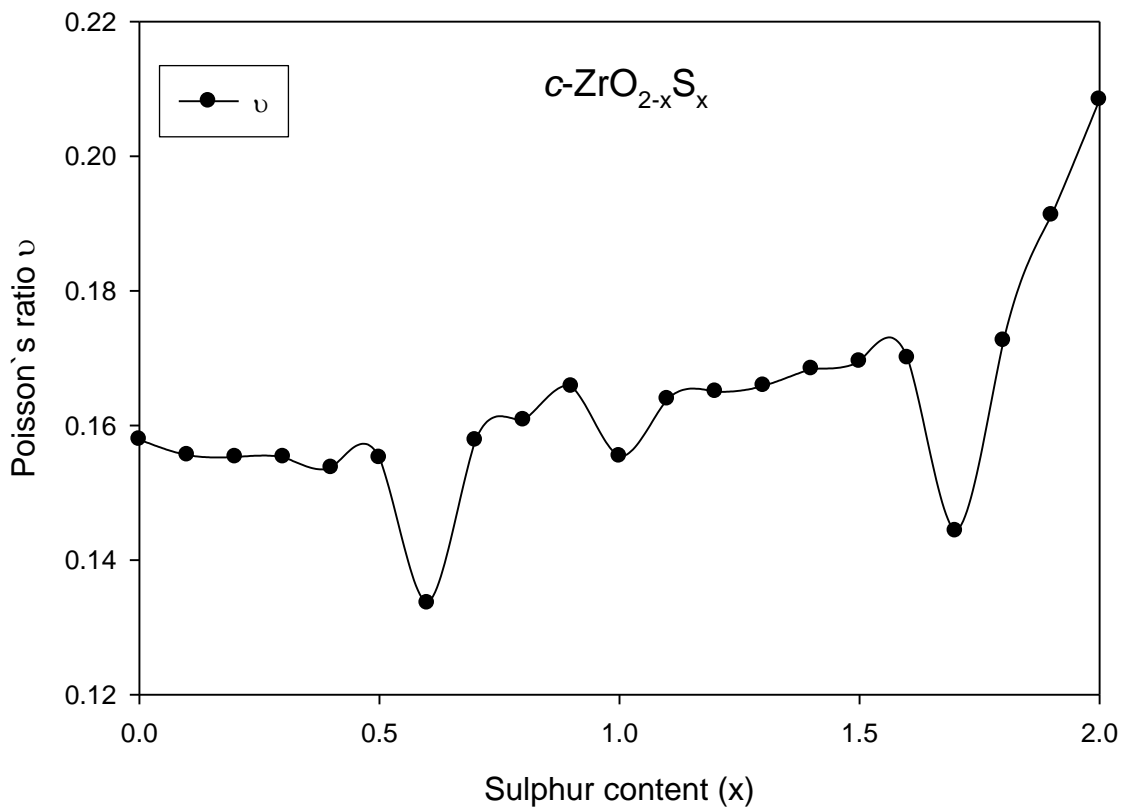


**Figure 35** Variation of the Poisson's ratio with S mole fraction for  $c-ZrO_{2-x}S_x$  solid solution

For  $t-ZrO_{2-x}S_x$  Young modulus and Poisson's ratios we have  $E_x=E_y \neq E_z$  and  $U_{xy}=U_{yx}$   $U_{xz}=U_{yz}$ , and  $U_{zx}=U_{zy}$  respectively. The  $E_x = E_y$  graph shape is similar to the Poisson ratio along  $U_{xz}=U_{yz}$  while the shape of  $E_z$  is similar to the one of Poisson's ratio along  $E_x=E_y$  for all sulphur concentrations in  $t-ZrO_2$ . The tetragonal solid solution shows a decrease of  $E_x$  until it become negative at x ranges from 0.5 to 0.8 and it increases drastically until it reaches the maximum value of 2700 at  $x = 0.9$  the  $E_x$  highest values are at  $x = 0.9$  and  $x = 1.1$ .

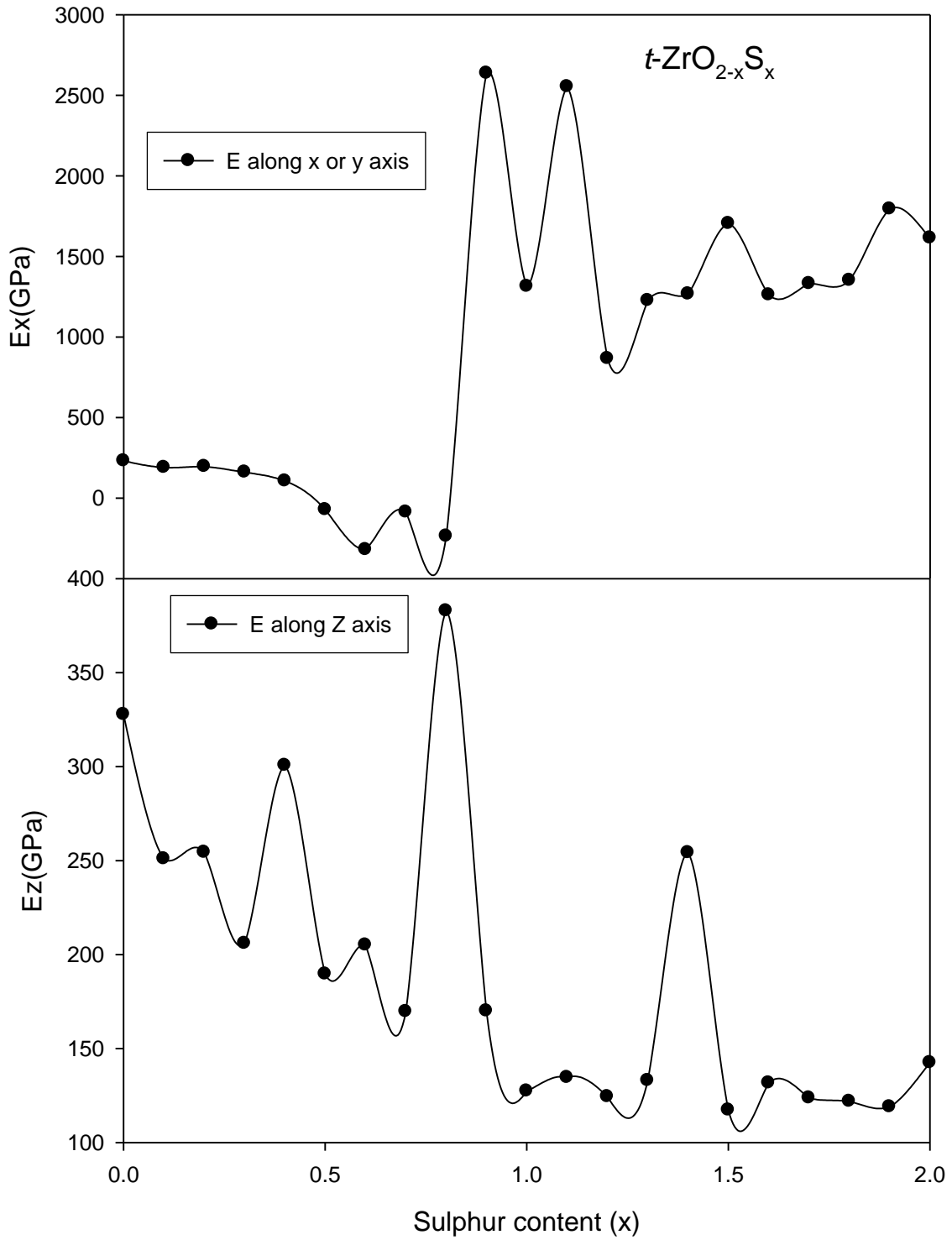


**Figure 36** Variation of the Young modulus with S mole fraction for  $t\text{-ZrO}_{2-x}\text{S}_x$  solid solution

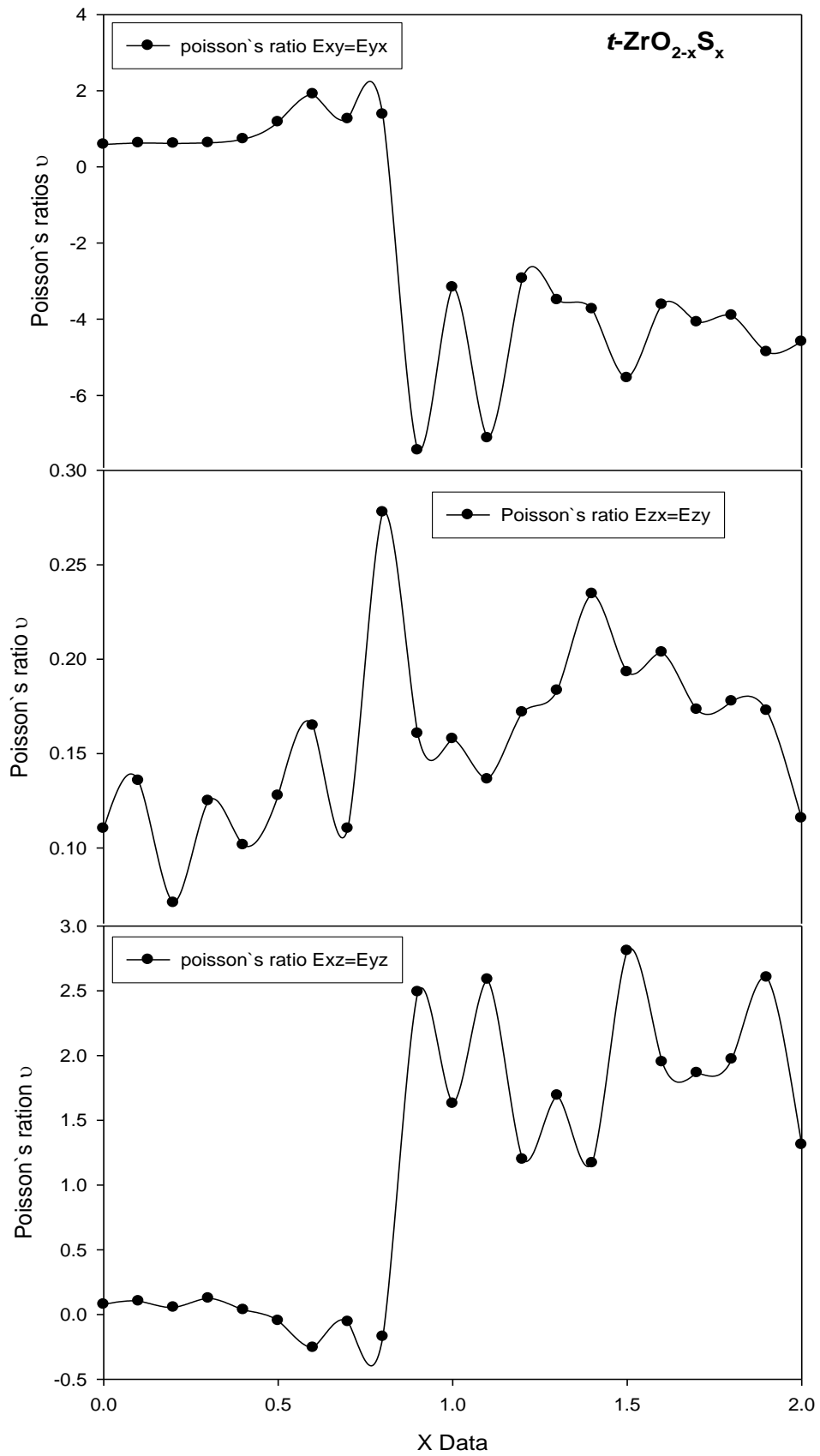


**Figure 37** Variation of the Poisson's ratio with S mole fraction for  $t\text{-ZrO}_{2-x}\text{S}_x$  solid solution

In general the  $E_x$  values for sulphated structures are higher than the  $E_x$  value for unsulphated  $t\text{-ZrO}_2$  from  $x = 0.9$  to  $x = 2$ , while all  $E_x$  values for  $x < 0.9$  are less as compared to the unsulphated structure.

$E_z$  reaches a maximum at  $x = 0.8$  after which it depreciates until it reaches 123GPa then recovers again at  $x = 1.4$ , and further decreases as a function of sulphur contents. It is interesting to note that all  $E_z$  values are positive which implies that our material is stiffer for the entire  $x$  range along  $Z$ . Some  $E_z$  values are negative.

Since Young's modulus is stress / strain, the high modulus at  $x = 0.9$  and at  $x = 0.8$  for  $E_x$  and  $E_z$  respectively, means that the stress value is greater compared to that of the material where the modulus is low, or in other words, the strain is much less compared to that of the material having low Young's modulus. So it tells that, if a material has high Young's modulus, the material requires more load for deformation of shape (within elastic limit).

Poisson's ratios of  $t\text{-ZrO}_{2-x}\text{S}_x$ , while the trend of  $U_{xz}=U_{yz}$  correlates with the Young modulus along  $E_z$  and  $U_{zx}=U_{zy}$  correlates with  $E_x$ , the shape of  $U_{xy}=U_{yx}$  behaves like the oscillating shape of  $U_{xz}$ . All values of  $U_{zx}$  are all within the range of  $-1 < U < 0.5$ , while the  $U_{xy}$  and  $U_{xz}$  are out of the range for some values. For  $U_{xy}$  the Poisson's ratios are positive for  $x$  ranges from  $x=0$  to  $x=0.8$  and their negative for  $x > 0.8$ . for  $U_{xz}$  the values are negative from  $x$  ranges from  $x=0.4$  to  $x=0.8$  and there positive for  $x$  ranges from  $x=0$  to  $x=0.3$ , and their within the range of  $0 < U < 0.5$ , the  $U_{xz}$  for  $x > 0.8$  are all positive but above the Poisson's ratios ranges. While  $U_{zx}$  values are all within the  $0 < U < 0.5$  range, all the values for  $U_{zx}$  are below 0.25 and above 0 except at  $x = 0.8$  where it is above 0.25 but below 0.5 which shows that the forces acting on the structure are central forces at  $x = 0.8$  and are not central for all the other  $x$  values.

Very little work is reported in the literature on elastic properties of pure monoclinic zirconia even with some information there are no experimental values for polycrystalline monoclinic zirconia. The plot in figure 38 of Young modulus values shows a regular decrease for  $E_x$  from  $x = 0$  to  $x = 1.4$  and a dramatic increase at  $x = 1.5$  and a decrease again until it reaches the highest value for the entire range and increases a little from  $x = 1.6$  to  $x = 2.0$ . It is interesting to know that its maximum value is at  $x = 1.5$  and all  $E_x$  are positive.  $E_y$  values start by a small



increase from  $x = 0$  to  $x = 0.2$  and then decrease in a small range and then show a very low value at  $x = 1.5$  and the increases a little from  $x = 1.5$  to  $x = 2.0$ ;

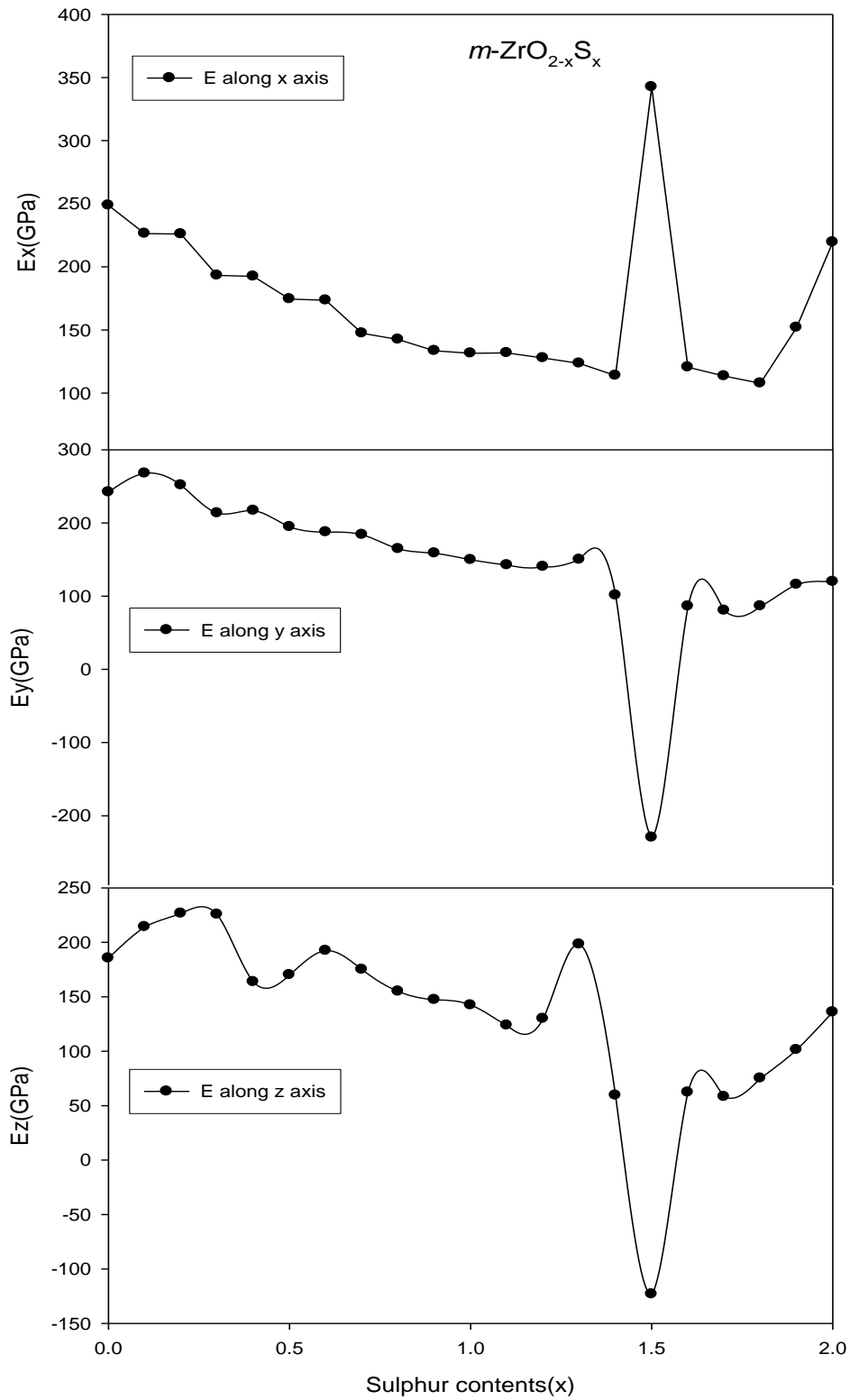


**Figure 38** Variation of the young modulus with S mole fraction for  $m\text{-ZrO}_{2-x}\text{S}_x$  solid solution

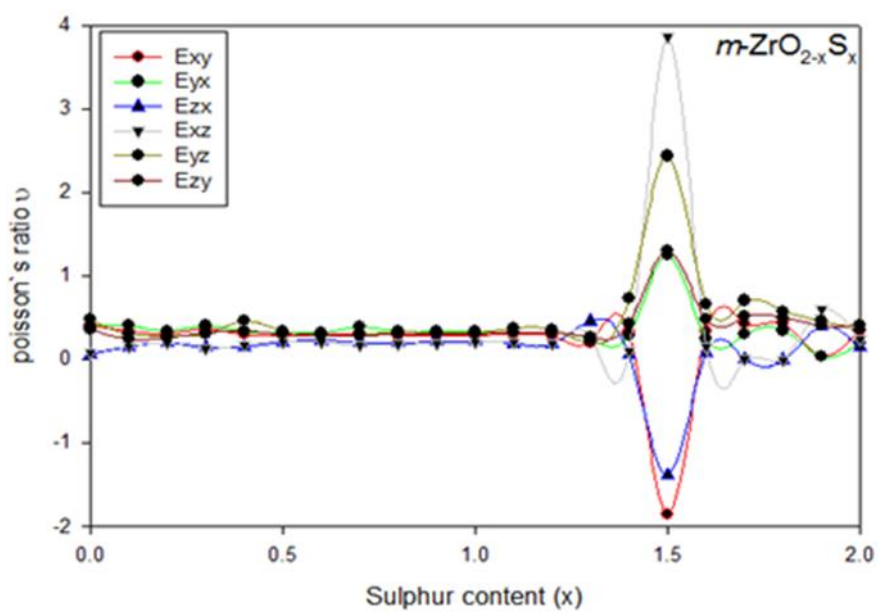
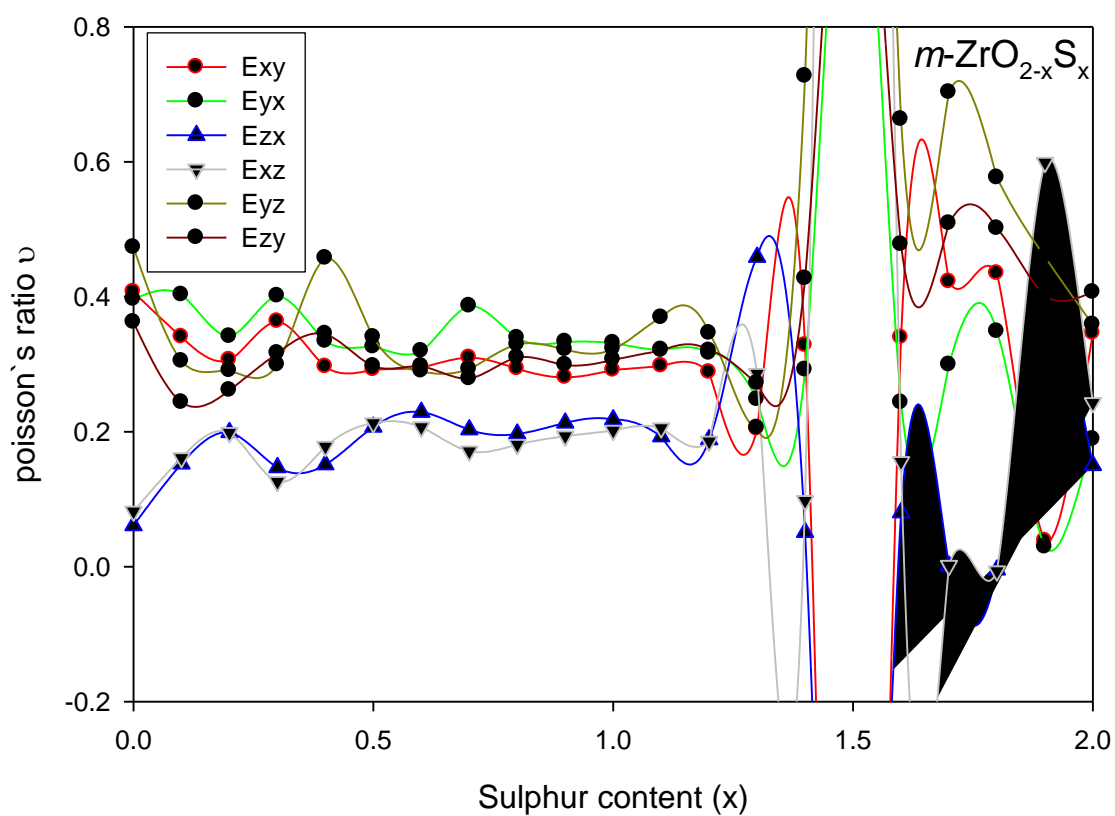


**Figure 39** Variation of the Poisson's ratio with S mole fraction for  $m\text{-ZrO}_{2-x}\text{S}_x$  solid solution

it is interesting to know that  $E_y$  has a minimum value at  $x = 1.5$  and all its values ranging from  $x = 0$  to  $x = 1.3$  are higher than the values for  $x > 1.3$ .  $E_z$  values increase slightly from  $x = 0$  to  $x = 0.3$  and slightly decrease until  $x = 1.2$  then again they increase a little at  $x = 1.3$ ; the decrease drastically from  $x = 1.3$  to  $x = 1.5$  were it became negative then increases again until  $x = 2.0$ .

Monoclinic  $ZrO_2$  Poisson's ratio are within the range  $0 < \nu < 0.5$  for  $x > 1.3$  except for  $\nu_{yz}$  at  $x = 1.2$ . at  $x = 1.5$  we got values that are out of range for all planes where  $\nu_{yz}$ ,  $\nu_{yx}$ ,  $\nu_{xz}$  and  $\nu_{zy}$  are greater than 1 and  $\nu_{xy}$  and  $\nu_{zx}$  are below -1. Above  $x = 1.5$   $\nu_{yz}$  values are above 0.5 at  $x = 1.6, 1.7$  and  $1.8$ ,  $\nu_{zy}$  values are above 0.5 at  $x = 1.7$  and  $1.8$  and  $\nu_{xz}$  values are above 0.5 at  $x = 1.9$ , while other  $\nu$  values are within the  $0 < \nu < 0.5$ . In general  $\nu_{xz}$  and  $\nu_{zx}$  show that forces acting on the structure are not central, however, other  $\nu$  values show that the forces that are acting are mainly central.  $m-ZrO_{2-x}S_x$ . Young modulus and Poisson's ratios are as follows  $E_x \neq E_y \neq E_z$ .

The bulk modulus ( $B$ ) which is a measure of resistance to volume change and shear modulus ( $G$ ) which is a measure of resistance to reversible deformation upon applied shear stress of a polycrystalline material can be estimated from the individual elastic constants  $C_{ij}$  by the Voigt approximation and the Reuss approximation. The general expressions for Voigt and Reuss approaches are represented in equations 2.27, 2.28, 2.29, 2.33 and 2.34 for bulk and shear modulus. The mechanical properties including bulk modulus, shear modulus and Pugh's ratios for three  $ZrO_{2-x}S_x$  polymorphs are shown in figure 40. The bulk modulus for  $m-ZrO_2$ ,  $t-ZrO_2$  and  $c-ZrO_2$  are 184, 193 and 248 GPa, respectively. The fracture strength for material is proportional to the bulk modulus, the stiffer the material, and the smaller the deformation of the material is. Therefore, the deformation of the three phases becomes easier in the order of  $c-ZrO_{2-x}S_x$ ,  $t-ZrO_{2-x}S_x$  and  $m-ZrO_{2-x}S_x$  at  $x = 0$ . It can be seen that  $ZrO_{2-x}S_x$  does not have strong resistance to a volume change of  $ZrO_2$  as a function of sulphur content. The shear modulus decreases in the following order  $112 > 91 > 66$  GPa for  $c-ZrO_{2-x}S_x > m-ZrO_{2-x}S_x > t-ZrO_{2-x}S_x$  at  $x = 0$ , respectively. The larger the value of shear modulus is, the more pronounced is directional bonding between atoms. The present calculations' results demonstrate directional bonding between atoms of  $t-ZrO_{2-x}S_x$  at  $x = (0.9, 1.0, 1.1)$  and  $m-ZrO_{2-x}S_x$  at  $x = 1.5$ .

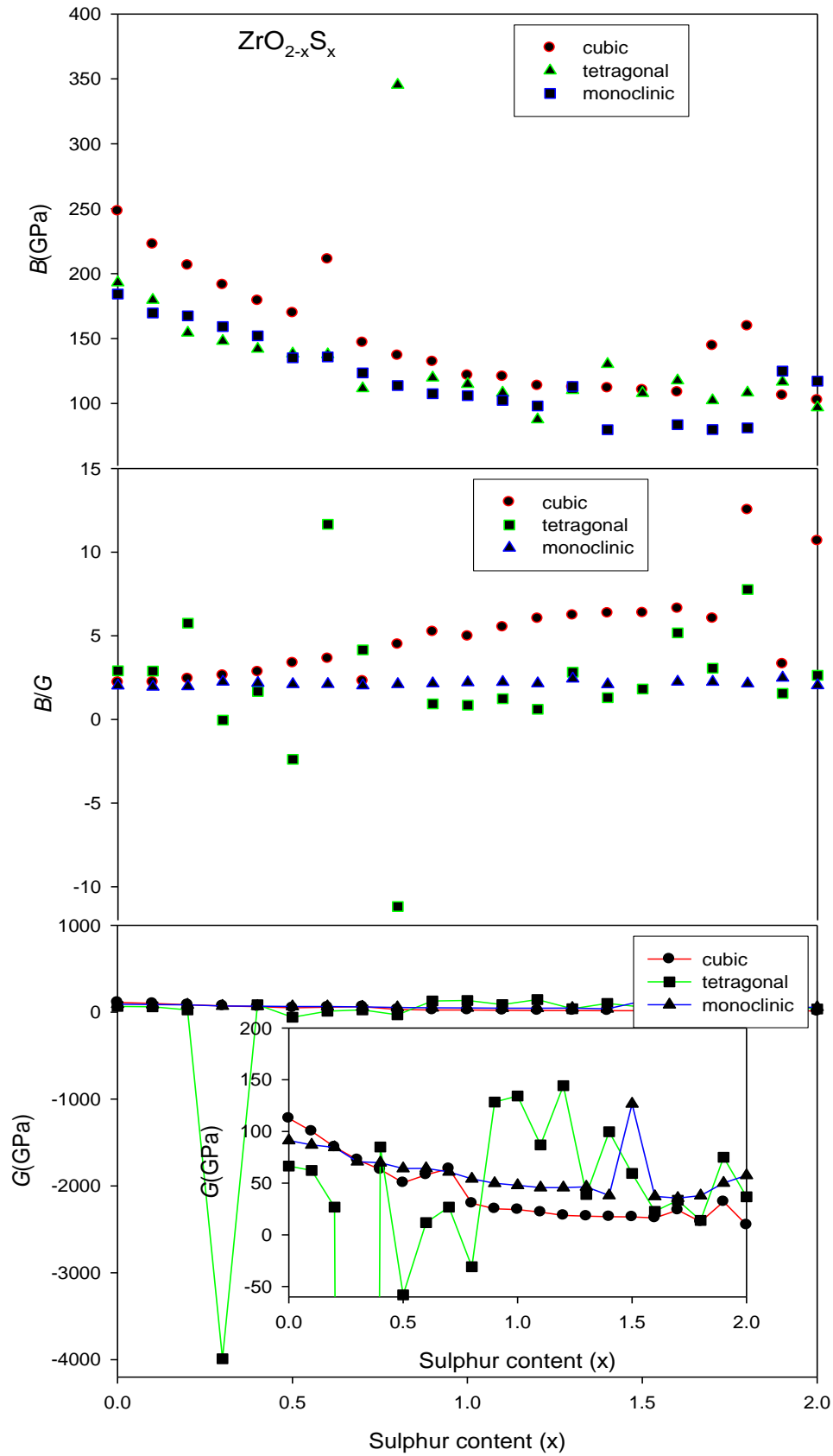


**Figure 40** Variation of the bulk modulus, shear modulus and Pugh's ratio with S mole fraction for (ctm)-ZrO<sub>2-x</sub>S<sub>x</sub> solid solution

The  $B/G$  ratio is related to brittleness and ductility of material: a high  $B/G$  value indicates ductility, while a low value shows brittleness the critical value is about 1.75. It can be seen from figure 40 that for all phase structures of  $ZrO_{2-x}S_x$  at  $x = 0$  the Pugh's have higher values than the critical one, suggesting that they are ductile. We also note that the  $B/G$  decreases in the following order:  $t-ZrO_{2-x}S_x > c-ZrO_{2-x}S_x > m-ZrO_{2-x}S_x$  at  $x = 0$  as seen from the figure. The three phase of  $ZrO_{2-x}S_x$  at  $x = 0$  change from ductile to brittle in the sequence of  $t-ZrO_{2-x}S_x$ ,  $c-ZrO_{2-x}S_x$  and  $m-ZrO_{2-x}S_x$ . This shows that  $m-ZrO_{2-x}S_x$  is the most brittle phase among the three structures. Generally, pure zirconia is monoclinic at room temperature. As the temperature increases,  $m-ZrO_2$  transforms to tetragonal ( $t-ZrO_2$ ) then to cubic ( $c-ZrO_2$ ) fluorite structure. This phase transition induces large volume changes and makes the pure material unsuitable for applications. The large volume changes may cause significant embrittlement of zirconia. These suggestion support our conclusions particularly for energy calculations.

It could be also be observed from figure 40 that  $B/G$  values for  $c-ZrO_{2-x}S_x$  increase with the S composition when  $x > 0.1$  and shows a slight decrease at  $x = 0.7$  and  $1.9$ . Moreover it can be deduced from figure 40 that all  $c-ZrO_{2-x}S_x$  for  $x$  ranges 0 to 2 are ductile with  $B/G$  values greater than 1.75. For  $t-ZrO_{2-x}S_x$  it could be observed that  $B/G$  increases from  $x=0$  to  $x=0.2$  and becomes negative at  $x = 0.3, 0.4, 0.5,$  and  $0.7$ . A negative Poisson ratio is linked to the bulk modulus only in isotropic material such as polycrystalline aggregates, softening in one or more elastic modulus tensor, typical shear modulus of single crystal is known to occur during transformation of structure, not in bulk modulus of polycrystalline aggregates. A single crystal may exhibit a negative Poisson ratio for a restricted range for the angle of deformation. A cooperative rotation of groups of atoms can lead to negative Poisson ratio [150].

Lastly, we investigate the elastic anisotropy factor for all structures of sulphated and unsulphated zirconia. It is well known that micro-cracks are induced in ceramics owing to anisotropy. Hence an important property of crystalline solids is the elastic anisotropy ratio which is defined by equations 2.28, 2.29 and 2.32. Essentially all known crystal are elastically anisotropic. For an anisotropic crystal  $A$  equals 1, while any value smaller or larger than 1 indicates anisotropy. The magnitude of a deviation from 1 is a measure of the degree of elastic anisotropy possessed by a crystal.

To further study the interatomic bonding in our modelling of random solid solution of cubic  $\text{ZrO}_{2-x}\text{S}_x$  solid solution, figure 41 represents the Cauchy relationships,  $C_{12}=C_{44}$ , or zero Cauchy pressure. Pettifor [151] has suggested that it could be used to describe the angular character of atomic bonding in metals and compounds. If the bonding is more metallic in character, the Cauchy pressure will be more positive, a negative Cauchy pressure, however, requires an angular or directional character in the bonding.

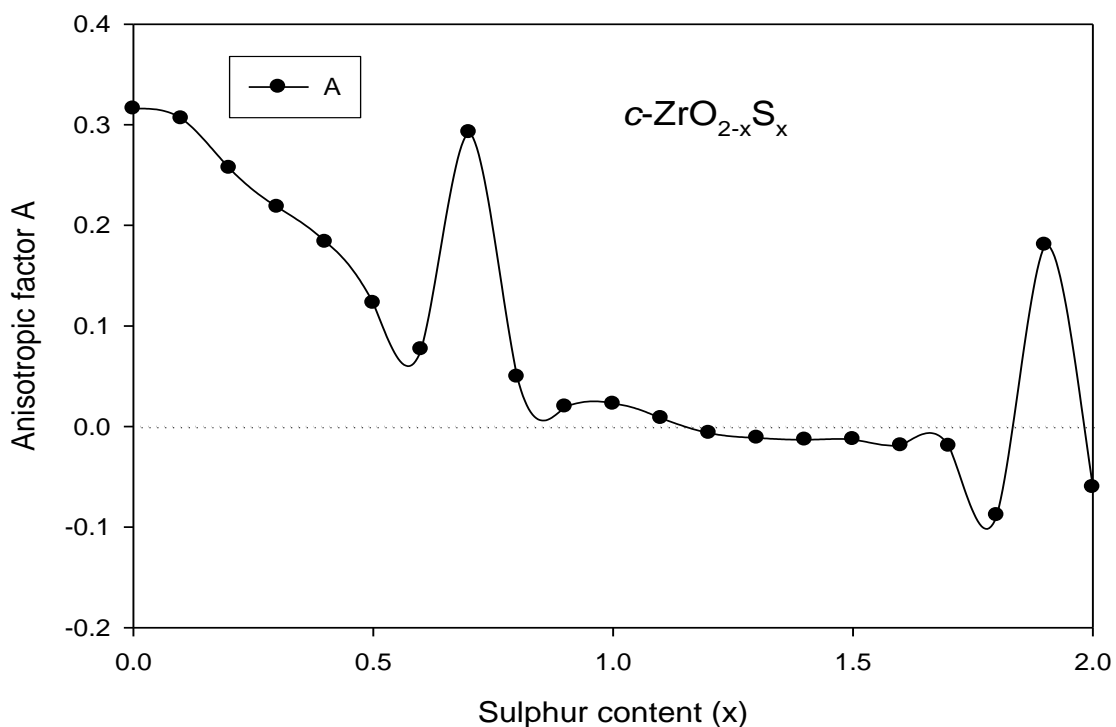


**Figure 41** Variation of anisotropic factor with S mole fraction for  $c\text{-ZrO}_{2-x}\text{S}_x$  solid solution

The more negative the Cauchy pressure, the more directional and lower mobility the bonding. In our calculations the Cauchy pressure has positive values for all values of  $x$ . it is the same ductile/brittle effects of  $C_{12}-C_{44}$  and  $B/G$  that leads to the same pattern of middle of figure 42.

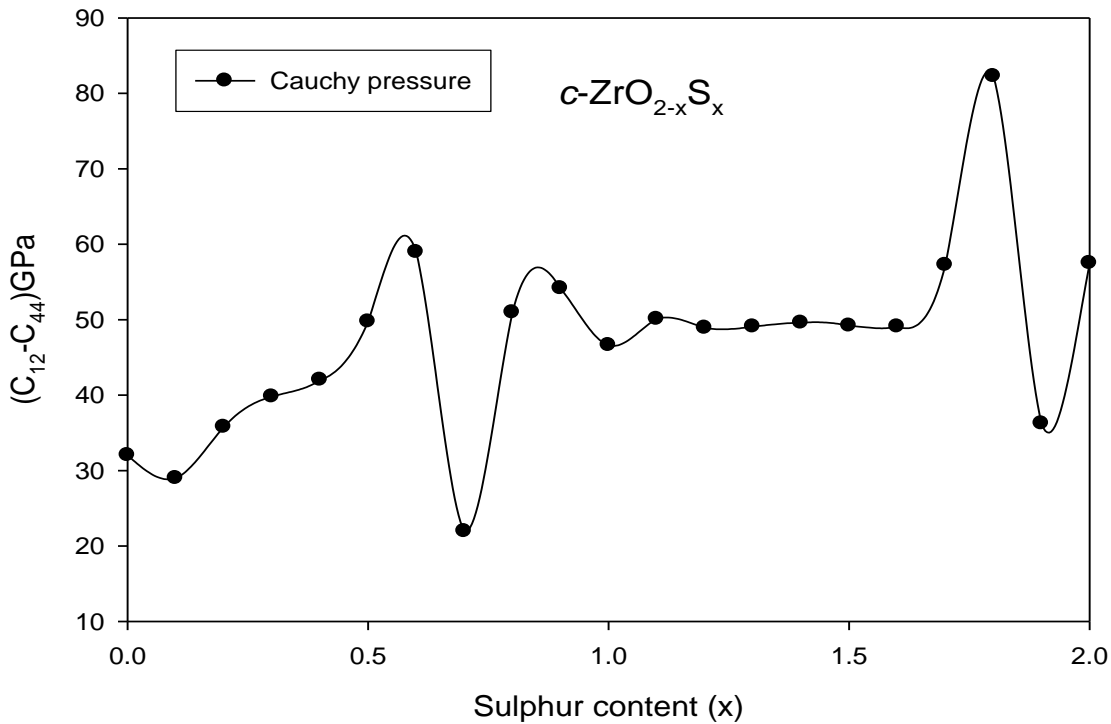


**Figure 42** Variation of Cauchy pressure with S mole fraction for  $c\text{-ZrO}_{2-x}\text{S}_x$  solid solution

The tetragonal anisotropy deviates considerable from unity, indicating the substantial elastic anisotropy for  $t\text{-ZrO}_{2-x}\text{S}_x$ .

It is interesting to note that  $C_{44}$  remains almost essential constant for the first two values of  $x$  (0 and 0.1). While  $C_{66}$  appears to decrease after an addition of sulphur. The denominator in the  $A_1$  anisotropy relation represents simple tension on (001) plane shear while the  $A_2$  anisotropy relation corresponds to shear along [011] direction on the  $(0\bar{1}1)$  plane [152]. The  $C_{66}$  and  $C_{44}$  elastic constants then correspond to shear resistance along [010] and [100] direction in (001) and (010) planes, respectively [152, 153].

Therefore the numerator (denominator) in  $A_3$  ratio represents the shear of intra-(inner-) layer bonds. The  $A_1$  elastic ratio starts by increasing from  $x = 0.0$ - $0.4$  and decrease drastically at  $x = 0.5$  until the values of  $A_1$  becomes negative,  $A_1$  values increase again within the negative range, from  $x = 0.9$  to  $x = 2.0$  the effect of sulphur seems to be the same.  $A_2$  decreases throughout the whole range of  $x$  values and shows a small increase at  $x = (0.6, 0.7)$ . The fully ordered  $t\text{-ZrO}_2$  exhibits significant

change of elastic properties as a function of sulphur content, which may be expressed by the deviation of ratio  $A_3$  from unity,  $A_3 = 0.133$ . However, as sulphur content increases,  $A_3$  shows that there might be micro changes of the structure; sulphur seems to be reducing the magnitude of uniaxial anisotropic elastic properties measured for bulk single crystal of  $t\text{-ZrO}_{2-x}\text{S}_x$ .

Furthermore, this indicates that the volume increase of  $t\text{-ZrO}_2$  caused by the larger size of sulphur content uniaxial, anisotropy  $C_{11} < C_{33}$  for  $x > 0.4$  and  $C_{44} < C_{66}$  for the entire  $x$  range. The one parameter that describes the elastic tetragonality,  $A_3$ , is smaller than unity; this implies that the shear stiffness along (100) is smaller than in (001) direction.

The measurements were not accurate enough to prove a significant deviation from the unity. The small deviation from the unity of  $A_2/A_1$  indicates that the elastic shear anisotropy of the crystal is close to that of equivalent elastically anisotropic crystal with cubic symmetry. Deviations from cubic symmetry of tetragonal elastic anisotropy parameters, as expressed by  $A_1/A_2$  and  $A_3$  are smaller

The elastic ductility behaviour was proposed to be related to so called Cauchy pressure. As stated previously, positive or negative values of the Cauchy pressures 1 and 2 indicate a ductile or brittle behaviour.

Despite the fact that the Young modulus and other elastic constant properties showed a general decrease, the Cauchy pressure is positive. This shows a ductile behaviour. Both Cauchy pressures increase as the sulphur content increases; this indicates that the material is ductile.



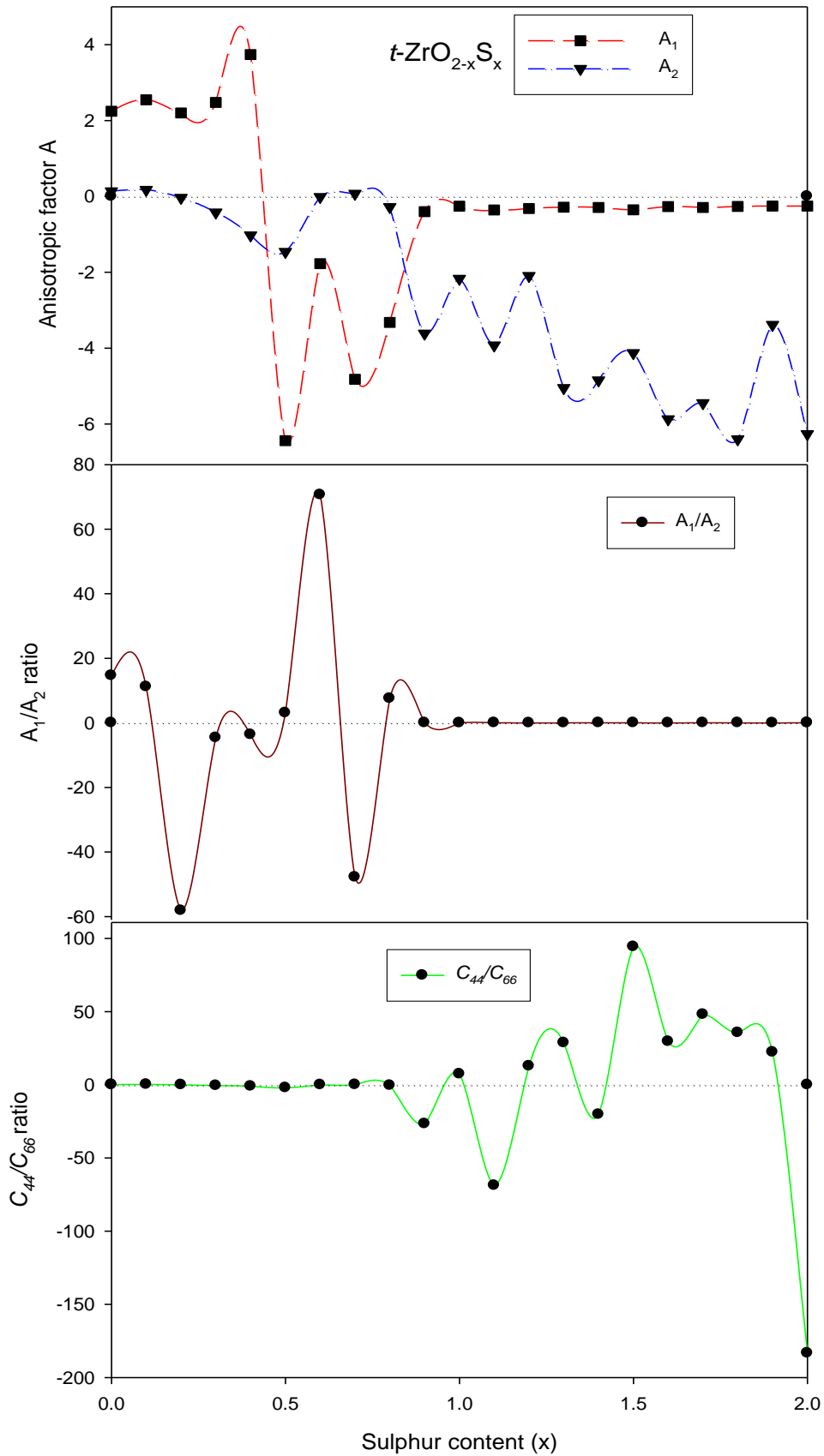


**Figure 43** Variation of anisotropic factor with S mole fraction for  $t\text{-ZrO}_{2-x}\text{S}_x$  solid solution

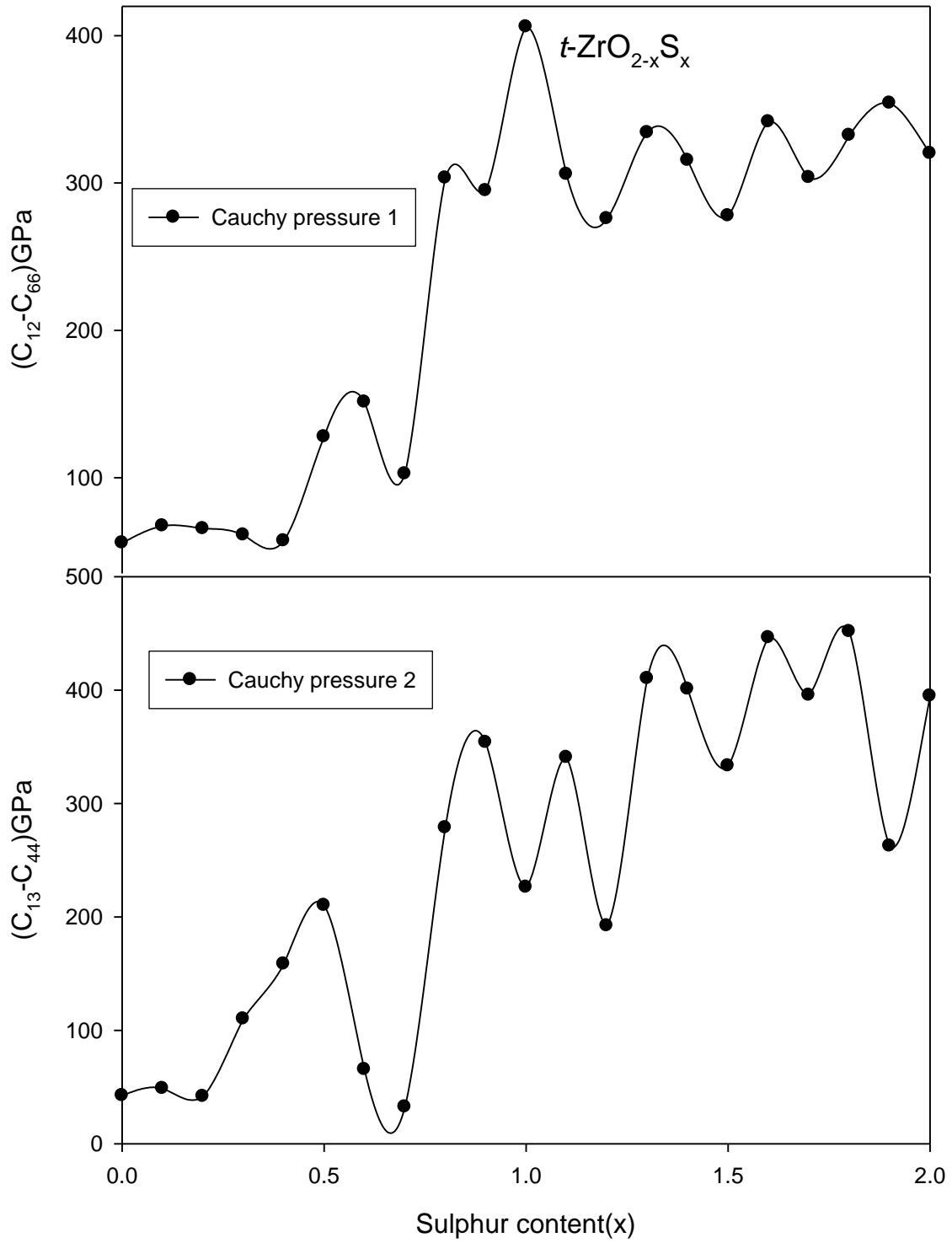


**Figure 44** Variation of Cauchy pressures with S mole fraction for  $t\text{-ZrO}_{2-x}\text{S}_x$  solid solution

The elastic anisotropy ratio is an important physical quality with regards to structural phase stabilities of crystal structures, in our case we investigated the anisotropies of compression (p) and two shear waves (S1 and S2) which are defined as [154].

$$\Delta_p = \frac{C_{33}}{C_{11}}; \Delta_{s1} = \frac{C_{11} - C_{13}}{2C_{44}}; \Delta_{s2} = \frac{2C_{44}}{C_{11} - C_{12}}; \quad 2.36$$

Estimation of anisotropy ratios,  $\Delta_p$ ,  $\Delta_{s1}$  and  $\Delta_{s2}$  are shown in figure 45 indicating the anisotropy of  $m\text{-ZrO}_{2-x}\text{S}_x$  compound, for x ranges from 0 - 2. It can be seen that the anisotropy of compression is fluctuating between 0.6 and 1.0 as a function of sulphur content except at x = 0.8 and 1.3 where the  $\Delta_p$  is 2.76 and 1.55 respectively. While the shear wave1 also  $\Delta_{s1}$  fluctuates except at x=0.8, 2.0, 1.9, 1.7 where it is 0.119, 2.44, 1.93, 1.6 and 1.69 respectively. Shear wave2  $\Delta_{s2}$  ranges from 0.8 to 1.05 for the entire x range except at x=0.1, 1.5, 1.9 and 2.0 where the values are -12.23, 1.47, 0.45 and 0.48 respectively. For a monoclinic structure the shear wave 1 is greater than the shear wave 2 and the compression wave except at x = 0.8 and 1.3. It is interesting to note from Table 16 that the values of  $\Delta_p$ ,  $\Delta_{s1}$  and  $\Delta_{s2}$  are not that different from other values that were investigated using first principle calculation by other researchers[141].

**Table 16** Anisotropy ratios for  $m\text{-ZrO}_{2-x}\text{S}_x$  for x= 0

parameter	theoretical [155]	WC
$\Delta_p$	0.917	0.727
$\Delta_{s1}$	1.498	1.460
$\Delta_{s2}$	0.834	1.00

Additionally the  $C_{13}/C_{12}$  in figure 45 is less than  $\Delta_p$ , for an anisotropic system the small  $C_{13}/C_{12}$  as compared to  $\Delta_p$  indicates that the atomic bonding along Z-axis is stronger than along the x-axis for the entire range of x, except at x = 1.9 and x = 2.0, where  $\Delta_p=0.003$  and  $C_{13}/C_{12}=1.24$  respectively. This implies that bonding along the x-axis is greater than the bonding along z-axis at these values of x.

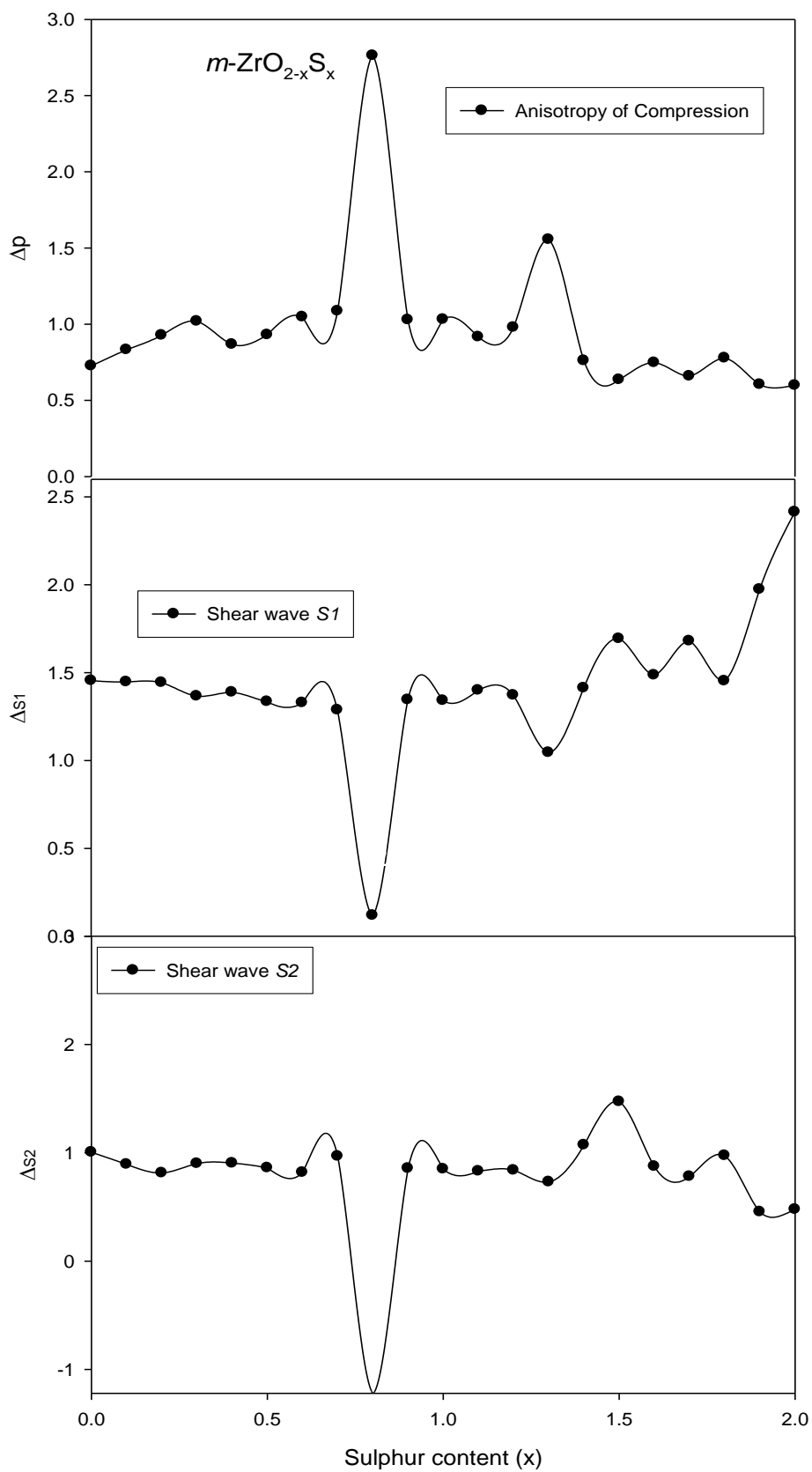


**Figure 45** Variation of anisotropic factor with S mole fraction for  $m\text{-ZrO}_{2-x}\text{S}_x$  solid solution

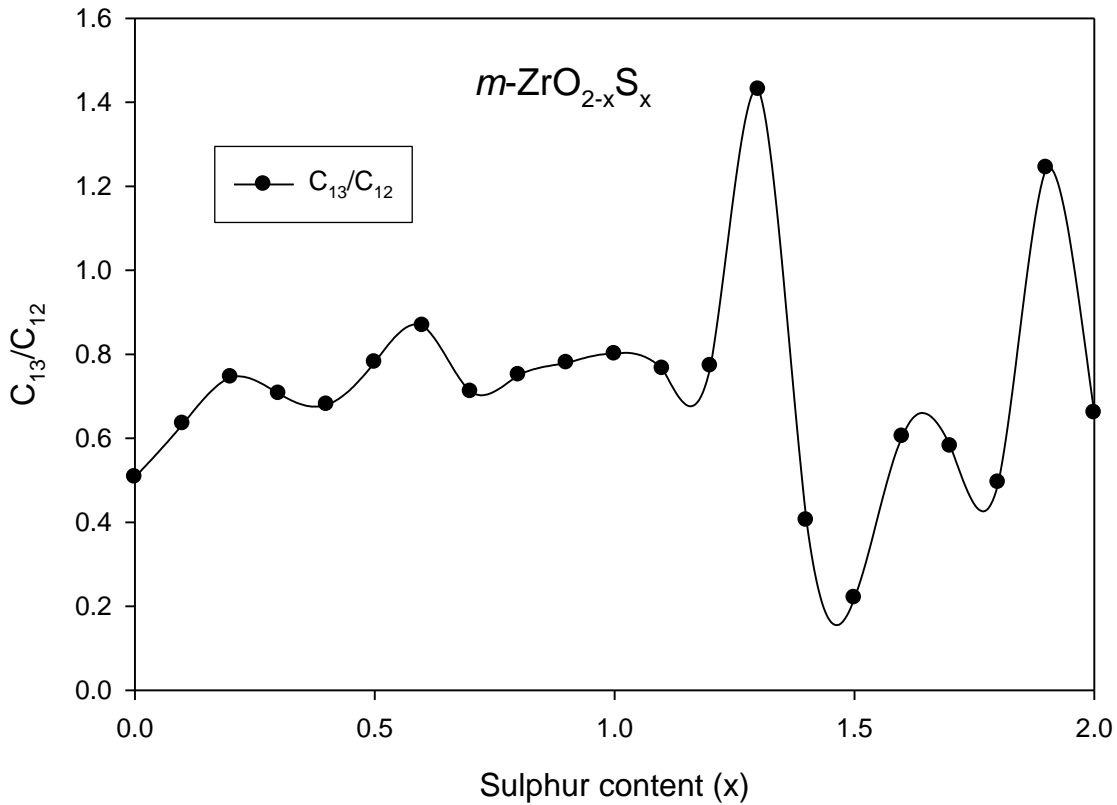


**Figure 46** Variation of anisotropic factor with S mole fraction for  $m\text{-ZrO}_{2-x}\text{S}_x$  solid solution

### 3.5.3. Summary of mechanical stability

It could be seen clearly that the calculated elastic constants are in agreement with the corresponding experimental and calculated values in the literature. (i) The overall diagonal element of elastic constants for  $m\text{-ZrO}_2$  gradually decreases with an increasing S content. However, the extent of decrease for elastic constant  $C_{11}$  and  $C_{22}$  is higher than that of  $C_{44}$ ,  $C_{55}$  and  $C_{66}$ , while  $C_{33}$  shows an increase for some S content concentration, its extent of decrease is higher than that of  $C_{44}$ ,  $C_{55}$  and  $C_{66}$ . As the S increases, the off diagonal elements gradually decrease except at some concentration where there are abrupt changes, where they are fluctuating or show increase as a function of S content. (ii) In addition, the diagonal elements have a higher extent of decrease than the off-diagonal elements. This indicates that the compressibility of  $m\text{-ZrO}_2$  crystal is not anisotropic as sulphur content increases with the conclusion drawn from the figure. (iii) For  $t\text{-ZrO}_2$ , the extent of decrease is  $C_{11}$ ,  $C_{33}$ ,  $C_{12}$  and  $C_{13}$  with increasing S content is higher than that of  $C_{44}$  and  $C_{66}$ , whereas the extent of decrease  $C_{11}$  and  $C_{12}$  are higher than that of  $C_{44}$  thus it can be

concluded that  $t\text{-ZrO}_2$  and  $c\text{-ZrO}_2$  are also not anisotropic under compression. The elastic constants  $C_{11}$  and  $C_{33}$  for  $t\text{-ZrO}_2$  decrease gradually and show a sudden increase in some S contents with their highest values at  $x = 0.8$ . (iv) It was observed that  $B$  of the solid solution decreases as we add sulphur contents. (v) we notice that with the increases in the distance between average Zr-OS bond, the  $B$  decreases owing to lattice expansion. (vi) In each of the cases, we see that  $B > G$ , which implies that the limiting parameter for mechanical stability of these materials is the shear modulus  $G$ . (vii) the direct influence of sulphur on the shear modulus of  $\text{ZrO}_2$  is less obvious than the case of  $B$ . (viii) We can see that the examined doped compounds for  $c\text{-ZrO}_{2-x}\text{S}_x$ ,  $t\text{-ZrO}_{2-x}\text{S}_x$  and  $m\text{-ZrO}_{2-x}\text{S}_x$  are ductile from  $x = 0.0 - 2.0$ , while  $m\text{-ZrO}_{2x}\text{S}_x$  is showing brittleness at these values of  $x = 0.4, 0.6$  and  $0.9$ . One of the reasons that can be attributed to these predictions is the size of doping element, which tends to affect volume of  $\text{ZrO}_2$ .

## CHAPTER 4

### CONCLUSIONS AND FUTURE WORK

#### 4.1. Conclusions and summary

Based on the density functional theory calculations, it has been shown that the variation of structural properties, electronic properties and elastic properties of random alloys is possible by using VCA. The VCA results resemble those observed by other first principle calculations. To draw a conclusion on the work carried out for this thesis is rather difficult as, it should be clear from the above discussions that we have barely scratched the surface on the applications of solid solutions techniques. Even so, we believe that the insights obtained from these initial studies indicate that, the chemical approach is quite valuable in elucidating solid solution phenomena. although it seems that our calculations using VCA is inadequate to describe this system (this work has been motivated by the experimental suggested effect of sulphur on *c*-ZrO<sub>2</sub>)

In summary, we have performed first principles calculations within the density function theory frame work using GGA WC exchange-correlation functionals for the ZrO<sub>2-x</sub>S<sub>x</sub> solid solution with x=0.0, 0.1, 0.2, 0.3, 0.4, 0.5, 0.6, 0.7, 0.8, 0.9, 1.0, 1.1, 1.2, 1.3,1.4, 1.5, 1.6, 1.7, 1.8, 1.9, 2.0, obtaining optimized geometries, structural and elastic constants, electronic band structures were calculated for x = 0.0 - 0.5. The unit cell optimizations exhibit a good agreement with the experimental results, in most of the cases the equilibrium lattice constants have shown a small error of 0.05 - 2%. Partial replacement of oxygen by sulphur leads to the almost linear expansion of lattice parameter and volume expansion rate due to atomic radius difference between oxygen and sulphur, which is equal to 1.09Å for sulphur compared to 0.65 Å of the host atom oxygen. Formation energies and cohesive energies for both tetragonal and cubic solid solution showed similar trends though they differ in magnitudes, they were positive at x = 0.8 to 1.5 for cohesive energies and formation energies for all three phases are positive for x ranging from x = 0.3 to x = 1.9 which suggests phase instabilities in this concentration range. The difference between our calculations of cohesive energies and available calculated cohesive energies showed a maximum error of 16%, while formation energies showed a maximum error of 4%.

The calculated electronic band structures underestimate measured main band gaps by about 1.6 eV for  $c\text{-ZrO}_{2-x}\text{S}_x$ , 1.5 eV for  $t\text{-ZrO}_{2-x}\text{S}_x$  and 2.3 eV for the  $m\text{-ZrO}_{2-x}\text{S}_x$  at  $x = 0$  computations as compared to the experimental ones. By close examination of bandwith sequence we note that the band gaps are 3.319 eV, 2.910 eV, 2.551eV, 2.232 eV, 1.946 eV and 1.686 eV for  $c\text{-ZrO}_{2-x}\text{S}_x$ , 4.019 eV, 3.651 eV, 3.320 eV, 3.010 eV, 2.732 eV and 2.465 eV for  $t\text{-ZrO}_{2-x}\text{S}_x$  and 3.580 eV, 3.234 eV, 2.924 eV, 2.638 eV, 2.358 eV and 2.165 eV for  $m\text{-ZrO}_{2-x}\text{S}_x$  at  $x = 0, 0.1, 0.2, 0.3, 0.4, 0.5$ . This implies that weaker covalency in this order, the strength of covalency may be related to the calculation results of cohesive energies, which are -28.283 eV, -22.94 eV, -18.123 eV, -13.753 eV, -9.850 eV and -6.387 eV, -28.287 eV, -23.017 eV, -18.192 eV, -13.825 eV, -9.88 eV and -6.425 eV and -28.377 eV, -23.133 eV, -18.337 eV, -13.979 eV, -10.076 eV and -6.638 eV for  $c\text{-ZrO}_{2-x}\text{S}_x$ ,  $t\text{-ZrO}_{2-x}\text{S}_x$  and  $m\text{-ZrO}_{2-x}\text{S}_x$ , respectively. It interesting to note that the band gaps obtained are in favourable agreement with other available calculated first principle values.  $c\text{-ZrO}_{2-x}\text{S}_x$  have direct band gaps, while  $t\text{-ZrO}_{2-x}\text{S}_x$  and  $m\text{-ZrO}_{2-x}\text{S}_x$  have indirect band gaps. The PDOS reveals that the uppermost valence bands have mainly a p-like character, while the bottom of the conduction band originates mainly from s orbitals, with the presence of d levels above 5 eV. Sulphur addition to  $\text{ZrO}_{2-x}\text{S}_x$  changes the conduction properties of  $\text{ZrO}_2$  based structures, and this can significantly change the traditional properties of  $\text{ZrO}_2$ .  $\text{ZrS}_2$  shows that the lower orbitals for Zr other than 4d are available for bonding.

We have shown also that we can successfully predict elastic properties of three polymorphs  $m\text{-ZrO}_2$ ,  $t\text{-ZrO}_2$  and  $c\text{-ZrO}_2$  typical to within 10% of experiment, with maximum error of 20%. The consistency that was used to estimate the elastic constants for unsulphated structures has also been for sulphated structures. A strong influence of the size of sulphur atom is seen on elastic properties of  $\text{ZrO}_2$ . Sulphur addition causes increase in lattice constants while decreasing bulk modulus. The work in this thesis provides evidence for a softening of the bulk modulus and negative Poisson's ratios particularly for  $t\text{-ZrO}_{2-x}\text{S}_x$  and  $m\text{-ZrO}_{2-x}\text{S}_x$ .  $c\text{-ZrO}_{2-x}\text{S}_x$  (at  $x = 0.6$ ) seems to be the most stable structure as compared to all sulphated structures evidenced by the higher Young modulus,  $C_{11}$ ,  $C_{12}$ ,  $C'$  negative cohesive energy and low Poisson's ratio. It can be seen from calculated anisotropy ratios that all structures are not elastic isotropic. One of the reasons for the ductile nature of the



compound can be attributed to their metallic bonds, known from their positive Cauchy pressure. The brittle nature of compound is also shown to be influenced by nature of bonding, for example the presence of mixture of ionic and covalent bond in  $ZrO_{2-x}S_x$ , is herein to be a factor contributing to the low ductility of these compounds. Generally all sulphated structures are less stable as evidenced by all the results we got from this thesis.

The predicted elastic properties include elastic stiffness constants  $C_{ij}$ , the bulk modulus and the Young modulus, the Poisson ratio and the anisotropy ratio.

Despite this intensity of effort, a few of the elastic properties have been studied and generally the subject would be strengthened by future studies, these properties include all sulphated  $t$ - $ZrO_2$  and  $m$ - $ZrO_2$  structures. Due to fundamental complexity of dopant-induced phase stabilisation of  $ZrO_2$ , it is not possible at present to undertake theoretical and experimental studies of identical system. In the first principle studies of this three polymorphs, we do not have theoretical values of sulphated  $t$ - $ZrO_2$  and  $m$ - $ZrO_2$  for all investigated properties. While for sulphated  $c$ - $ZrO_2$  we do have other first principle calculated values for lattice parameters, formation energy, cohesive energy and electronic structure part. However, for sulphated  $c$ - $ZrO_2$  we do not have any theoretical values to compare with mechanical properties in this thesis.

The currently used VCA approach does not only predict the available correct structural parameters but it is also computationally and time efficient. Since sulphated  $c$ - $ZrO_2$  is of much interest both scientifically and technologically, one might expect many of these areas to be studied intensively within next few years. We hope that some of our results estimated for the first time in this work such as the elastic properties of  $ZrO_2$  as a function of sulphur contents, makes a significant contribution to the existing data and simulate the experimental basic properties of hypothetical solid solution  $ZrO_{2-x}S_x$ .

## 4.2. Future work and recommendations

Modelling work has allowed some suggestions to be made to find experimental collaborators regarding possible future work. Considerable success has been achieved in deducing structural properties of materials using VCA. In Chapter 3, some suggestions were made as to possible structures for a series of  $\text{ZrO}_{2-x}\text{S}_x$  system.

It was noted however that these structural postulations were far from conclusive as the structures maintain their symmetries using VCA. Although VCA assumes  $\text{ZrO}_2$  in their symmetry, other symmetry are possible using Supercell and UNiversal CLuster Expansion (UNCLE) [156] approach, and future work would ideally consider these in combination with the approach already presented. Furthermore, the Supercell and UNCLE might be of considerable use in this instance. In MedeA-UNCLE lets you determine stable multi-component crystal structures and rank metastable structures by enthalpy of formation. Performing VASP ab-initio calculations on automatically chosen sets of small models, MedeA-UNCLE captures the configurational complexity of real materials at different temperatures by means of Monte Carlo random sampling. Future work utilising this approach might be prudent in this instance.

Future work could involve different approaches like Pettifor-type structure and high-throughput (HT) first-principles [157, 158] maps that point to new opportunities for solid solution research. The maps demonstrate that the integration of the empirical and computational data produces enhanced maps that should provide a more comprehensive foundation for rational materials design. The theoretical predictions presented by the map will hopefully serve as a motivation for the experimental validation and be a guide for future studies of these important systems.

## BIBLIOGRAPHY

- [1] R. Srinivasan and B. H. Davis, "Zirconia: A Review of a Super Ceramic," in *Material Synthesis and Characterization*, New York, Plenum Press, 1997, pp. 147-188.
- [2] X. Song and A. Sayari, "Sulfated Zirconia-Based Strong Solid-Acid Catalysts: Recent Progress.," *Catal. Rev. Sci. Eng.*, vol. 38, pp. 329-412, 1996.
- [3] M. H. Bocanegra-Bernal and S. Dioz De La Torre, "Phase Transitions in Zirconium dioxide and Related Material for High Performance Engineering Ceramics," *J. Mater. Sci.*, vol. 37, pp. 4947-4971, 2002.
- [4] M. Kibsey, J. Romualdez, X. Huang, R. Kearsley and Q. Yang, "Mechanical Properties of Titania-Doped Yttria Stabilized Zirconia (TiYSZ) for Use as Thermal Barrier Coating (TBC)," *J. eng. gas turb power.*, vol. 133, pp. 1221011-1221019, 2011.
- [5] Z. Khamverdi and Z. Moshiri, "Zirconia: An Up-to-date Literature Review," *A review.*, vol. 4, pp. 1-15, 2013.
- [6] L. Fryda, K. D. Panopoulos and E. Kakaras, "Integrated CHP with Autothermal Biomass Gasification and SOFC-MGT," *Energy Convers. Manage.*, vol. 49, pp. 281-290, 2008.
- [7] S. Cordiner, M. Feola M, V. Mulone and F. Romanelli, "Analysis of a SOFC Energy Generation System Fuelled with Biomass Reformate," *Appl. Therm. Eng.*, vol. 27, pp. 738-747, 2007.
- [8] S. Karellas , J. Karl and E. Kakaras , "An Innovative Biomass Gasification Process and Its Coupling with Microturbine and Fuel Cell Systems.," *Energy*, vol. 33, pp. 284-291, 2008.
- [9] J. R. Andersson, H. Kleinke and H. F. Franzen, "  $ZrO_{2-x}S_x$ : Stabilization of Cubic  $ZrO_2$  by a Partial Exchange of Oxygen by Sulfur," *J. Alloys Compd.* , vol. 259, pp. L14 - L18, 1997.
- [10] Z. Shao, W. Zhou and Z. Zhu, "Advanced Synthesis of Materials for Intermediate-Temperature Solid Oxide Fuel Cells," *prog mater sci.*, vol. 57, pp. 804-874, 2012.

- [11] J. Iniguez, D. Vanderbilt and L. Bellaiche, "First-Principles Study of  $(\text{BiScO}_3)_{1-x}(\text{PbTiO}_3)_x$  Piezoelectric Alloys," *Phys. Rev. B.*, vol. 67, pp. 2241071-2241076, 2003.
- [12] N. J. Ramer and A. M. Rappe, "Application of a New Virtual Crystal Approach for the Study of Disordered Perovskites," *J. Phys. Chem. Solids.*, vol. 61, pp. 315-320, 2000.
- [13] R. G. Nesten and M. B. Hall, "A Zirconium Concentrated-Arc Infrared Source for Infrared Spectroscopy," *J. Optical Soc. Am.*, vol. 42, pp. 257-258, 1952.
- [14] L. Navias, "Ceramic Dielectric Material and Method of Making". United States Of America Patent 2,515,790, 18 July 1950.
- [15] D. Smith and H. Newkirk, "The Crystal Structure of Baddeleyite (monoclinic  $\text{ZrO}_2$ ) and its Relation to the Polymorphism of  $\text{ZrO}_2$ ," *Acta. Cryst.*, vol. 18, pp. 983-991, 1965.
- [16] M. Finnis and T. Paxton, "Crystal Structures of Zirconia from First Principle and Self-Consistent Tight Binding," *Phys. Rev. Lett.*, vol. 81, pp. 5149-5152, 1998.
- [17] G. Teufer, "The Crystal Structure of Tetragonal  $\text{ZrO}_2$ ," *Acta. Cryst.*, vol. 15, p. 1187, 1962.
- [18] J. McCullough and K. Trueblood, "The Crystal Structure of Baddeleyite (monoclinic  $\text{ZrO}_2$ )," *Acta. Cryst.*, vol. 12, pp. 507-511, 1959.
- [19] H. J. Goldschmidt, "Selected Applications of High-Temperature X-Ray Studies in the Metallurgical Field," *Adv. X-ray Anal.*, vol. 5, pp. 191-212, 1962.
- [20] G. M. Wolten, "Diffusionless Phase Transformations in Zirconia and Hafnia," *J. Am. Chem. Soc.*, vol. 46, pp. 418-422, 1963.
- [21] A. Christensen and E. A. Carter, "First-Principles Study of the Surfaces of Zirconia," *Phys. Rev. B.*, vol. 58, pp. 8050-8064, 1998.
- [22] E. V. Stefanovich, A. L. Shluger and C. R. A. Catlow, "Theoretical Study of the Stabilization of Cubic-Phase  $\text{ZrO}_2$  by Impurities," *Phys. Rev. B.*, vol. 49, pp. 11560-11571, 1994.
- [23] W. Z. Zhu, T. C. Lei, Y. Zhou and Z. S. Ding, "Effect of Cooling Rate on Tetragonal to Monoclinic Transformation in Hot Pressed  $\text{ZrO}_2(\text{Y}_2\text{O}_3)$  Ceramics," *Scripta. Metall. Mater.*, vol. 33, pp. 1439-1444, 1995.

- [24] R. H. French, S. J. Glass, F. S. Ohuchi, Y. N. Xu and W. Y. Ching, "Experimental and Theoretical Determination of the Electronic Structure and Optical Properties of Three Phases of  $ZrO_2$ ," *Phys. Rev. B.*, vol. 49, pp. 5133-5142, 1994.
- [25] H. Yugami, A. Koike, M. Ishigame and T. Suemoto, "Relationship between Local Structures and Ionic Conductivity in  $ZrO_2$ - $Y_2O_3$  Studied by Site-Selective Spectroscopy," *Phys. Rev. B.*, vol. 44, pp. 9214-9222, 1991.
- [26] K. Yasuda, S. Arai, M. Itoh and K. Wada, "Influence of  $Y_2O_3$  Distribution on the Rate of Tetragonal to Monoclinic Phase Transformation of Ytria-Stabilized Zirconia During Hydrothermal Aging," *J. Mater. Sci.*, vol. 34, pp. 3597-3604, 1999.
- [27] S. J. Hong, S. D. De La Torre, L. Gao, K. Miyamoto and H. Miyamoto, "Synthesis and Mechanical Properties of  $ZrO_2/Al_2O_3$  Composites Prepared by Spark Plasma Sintering," *J. Mater. Sci. Lett.*, vol. 17, pp. 1313-1315, 1998.
- [28] R. C. Garvie, "The Occurrence of Metastable Tetragonal Zirconia as Crystallite Size Effect," *J. Phys. Chem.*, vol. 69, pp. 1238-1243, 1965.
- [29] R. C. Garvie, "Stabilization of the Tetragonal Structure in Zirconia Microcrystals," *J. Phys. Chem.*, vol. 82, pp. 218-224, 1978.
- [30] Y. Murase and E. Kato, "Role of Water Vapour in Crystallite Growth and Tetragonal-Monoclinic Phase Transformation of  $ZrO_2$ ," *J. Am. Ceram. Soc.*, vol. 66, pp. 196-200, 1983.
- [31] P. E. D. Morgan, "Synthesis of 6-nm Ultrafine Monoclinic Zirconia," *J. Am. Ceram. Soc.*, vol. 67, p. 637-704, 1984.
- [32] C. J. Norman, P. A. Goulding and I. McAlpine, "Role of Anions in the Surface Area Stabilisation of Zirconia," *Catal. Today.*, vol. 20, pp. 313-321, 1994.
- [33] C. J. Norman, P. A. Goulding and P. J. Moles, "The role of sulfate in the stabilization of zirconia," *Stud. Surf. Sci. Catal.*, vol. 90, pp. 269-272, 1994.
- [34] B. H. Davis, R. A. Keogh and R. Srinivasan, "Sulfated Zirconia as a Hydrocarbon Conversion Catalyst," *Catal. Today.*, vol. 20, pp. 219-256, 1994.
- [35] R. Srinivasan, R. J. De Angelis and B. H. Davis, "Factors Influencing the Stability of the Tetragonal Form of Zirconia," *J. Mater. Res.*, vol. 1, pp. 583-588,

1986.

- [36] R. Srinivasan, M. B. Harris, S. F. Simpson, R. J. De Angelis and B. H. Davis, "Zirconium Oxide Crystal Phase: The Role of pH and Time to Attain the Final pH for Precipitation of Hydroxous Oxide," *J. Mater. Res.*, vol. 3, pp. 787-797, 1988.
- [37] O. Yu. Kurapova and V. G. Konakov, "Phase Evolution in Zirconia Based System," *Rev. Adv. Mater. Sci.*, vol. 36, pp. 177-190, 2014.
- [38] S. J. Juutilainen, P. A. Simell and A. O. I. Krause, "Zirconia: Selective Oxidation Catalyst for Removal of Tar and Ammonia from Biomass Gasification Gas," *App. Catal. B-Environ.*, vol. 62, pp. 86-92., 2006.
- [39] S. Juutilainen, P. Simell and O. Krause, Doped zirconias in catalytic cleaning of gasification gas, New Bury: CPL Press, 2006.
- [40] K. Tanabe, "Surface and Catalytic Properties of  $ZrO_2$ ," *Mater. Chem. Phys.*, vol. 13, p. 347-364, 1985.
- [41] R. Nielsen, "Zirconium and zirconium compounds," in *In: Ullmann's encyclopedia of industrial chemistry 7th edn.*, Wiley- VCH, 2007.
- [42] F. del Monte, W. Larsen and J.D. Mackenzie, "Stabilization of Tetragonal  $ZrO_2$  in  $ZrO_2$ - $SiO_2$  Binary Oxides," *J. Am. Ceram. Soc.*, vol. 83, pp. 628-634, 2000.
- [43] F. del Monte, W. Larsen and J.D. Mackenzie, "Chemical Interactions Promoting the  $ZrO_2$  Tetragonal Stabilization in  $ZrO_2$ - $SiO_2$  Binary Oxides," *J. Am. Ceram. Soc.*, vol. 83, pp. 1506-1512, 2000.
- [44] W. Torres, S. Pansare and J. Goodwin, "Hot Gas Removal of Tars, Ammonia, and Hydrogen Sulfide from Biomass Gasification Gas," *Catal. Rev. Sci. Eng.*, vol. 49, pp. 407-456, 2007.
- [45] M. Sugioka, T. Nakayama, Y. Uemichi and T. Kanazuka., "Promotive Effect of  $H_2S$  for Hydrocarbon Conversions," *React. Kinet. Catal. Lett.*, vol. 41, pp. 345-350, 1990.
- [46] M. Ziolek, J. Kujava, O. Sauer, and G. C. Lavalley, "Influences of  $H_2S$  Adsorption on Catalytic Properties of Metal Oxides," *J. Mol. Catal.*, vol. 97, pp. 49-56, 1995.
- [47] A. Clearfield and P. Vaughan, "The Crystal Structure of Zirconyl Chloride

- Octahydrate and Zirconyl Bromide Octahydrate,” *Acta. Cryst.*, vol. 9, pp. 555-558, 1956.
- [48] G. M. Bodner, “Bodner Research Web,” 7 February 1998. [Online]. Available: <http://chemed.chem.purdue.edu/genchem/topicreview/bp/ch10/group6.php>. [Accessed 17 November 2011].
- [49] K. S. Bartwal and O. N. Srivasta, “Growth and Characterization of Single Crystals in the Series  $ZrS_xSe_{2-x}$ ,” *Mater. Sci. Eng.*, vol. 33, pp. 115-121, 1995.
- [50] J. D. McCullough, L. Brewer and L. A. Bromley, “The Crystal Structure of Zirconium Oxysulfide,  $ZrOS$ ,” *Acta Cryst.*, vol. 1, pp. 287-289, 1948.
- [51] O. Malyi, Z. Chen and P. Wu, “Effect of Sulphur Impurity on the Stability of Cubic Zirconia and its Interfaces with Metals,” *J. Mater. Chem.*, vol. 21, pp. 12363-12368, 2011.
- [52] J. R. Anderson, H. Kleinke and H. G. Franzen, “ $ZrO_{2-x}S_x$ : Stabilization of Cubic  $ZrO_2$  by Partial Exchange of Oxygen by Sulphur,” *J. Alloy. Compd.*, vol. 259, pp. 14-18, 1997.
- [53] G. Ceder, M. Asta, W.C. Carter, M. Sluiter, M. E. Mann, M. Kraitchman and D. de Fontaine, “Phase Diagram and Low-Temperature Behavior of Oxygen Vacancy Ordering in  $YBa_2Cu_3O_z$  using Ab Initio Interactions,” *Phys. Rev. B.*, vol. 41, pp. 8698-8701, 1990.
- [54] A. van der Ven, M. K. Aydinol, G. Ceder, G. Kresse and J. Hafner, “First-Principles Investigation Of Phase Stability In  $Li_xCoO_2$ ,” *Phys. Rev. B.*, vol. 58, pp. 2975-2987., 1998.
- [55] R. G. Parr and W. Yang, Density functional theory of atoms and molecules, New York: Oxford University Press, 1989.
- [56] M. P. Allen and D. J. Tildesley, Computer Simulation of Liquids, New York: Oxford University Press, 1987.
- [57] L. Bellaiche and D. Vanderbilt, “Virtual Crystal Approximation Revisited: Application to Dielectric and Piezoelectric Properties of Perovskites,” *Phys. Rev. B.*, vol. 61, pp. 7877-7882, 2000.
- [58] B. Velicky, S. Kirkpatrick and H. Ehrenreich, “Single-Site Approximations in the Electronic Theory of Simple Binary Alloys,” *Phys. Rev.*, vol. 175, p. 747–766,

1968.

- [59] M. J. Phasha, M. Kasonde and P. E. Ngoepe, "Effect of Pressure on the Metastable Phase Formation of Equilibrium Immiscible Ti-Mg System Studied by Ab Initio Technique and Mechanical Milling," in *Science Real and Relevant: 2nd CSIR Biennial Conference, CSIR International Convention Centre Pretoria, Pretoria, 2008*.
- [60] M. J. Phasha, P. E. Ngoepe, H. R. Chauke, D. G. Pettifor and D. Nguyen-Mann, "Link Between Structural and Mechanical Stability of fcc- and bcc-Based Ordered Mg-Li Alloys," *IMCs.*, vol. 18, pp. 2083-2089, 2010.
- [61] S. V. Stolbov and R. E. Cohen, "First-principles Calculation of the Formation Energy in MgO-CaO Solid Solutions," *Phys. Rev. B.*, vol. 65, pp. 0922031-0922033, 2002.
- [62] S. Yamamoto, T. Wakabayashi and H. Kobayashi, "Cohesive Energy and Energy Fluctuation as a Measure of Stability of Phases in Alloys," *J. Japan Inst. Metals.*, vol. 58, pp. 855-864, 1994.
- [63] V. N. Nikiforov, V. G. Sredin and K. R. Kurbanov, "Elasticity Moduli of  $Cd_xHg_{1-x}Te$  Solid Solutions," *Russ J Math Phys.*, vol. 54, pp. 271-276, 2011.
- [64] M. Wuttig, L. Dai and J. Cullen, "Elasticity and Magnetoelasticity of Fe-Ga Solid Solutions," *Appl. Phys. Lett.*, vol. 80, pp. 1135-1135, 2002.
- [65] J. D. Bass and M. Kanzaki, "Elasticity of a Majorite-Pyrope Solid Solution," *GRL.*, vol. 17, pp. 1989-1992, 1990.
- [66] K. Chen, L. Zhao, P. C. Patnaik and J. S. Tse, "Elastic Properties of Multi-Component Nickel Solid-Solutions," *TMS.*, pp. 753-758, 2004.
- [67] S. F. Pugh, "Relations Between the Elastic Moduli and the Plastic Properties of Polycrystalline Pure Metals," *Phil. Mag.*, vol. 45, pp. 823-843, 1954.
- [68] X. H. Hou and S. J. Hu, "First Principles Studies on the Electronics Structures of  $(Li_{1-x} Me_x)FePO_4$  (Me=Na and Be)," *Chinese Sci Bull.*, vol. 55, pp. 3222-3227, 2010.
- [69] S. J. Smith and B. T. Sutcliffe, "The Development of Computational Chemistry in the United Kingdom," *Rev Comp Ch.*, vol. 70, p. 271-316, 1997.
- [70] K. Burke, "Perspective on density functional theory," *J. Chem. Phys.*, vol. 136,



- pp. 1509011-15090110, 2012.
- [71] A. J. Cohen, P. Mori-Sánchez and W. Yang, “Challenges for Density Functional Theory,” *Chem. Rev.*, vol. 112, p. 289–320, 2012.
- [72] J. P. Perdew, A. Ruzsinszky, L. A. Constantin, J. Sun and G. I. Csonka , “Some Fundamental Issues in Ground-State Density Functional Theory: A Guide for the Perplexed,” *J. Chem. Theory Comput.* , vol. 5, p. 902–908, 2009.
- [73] P. Hohenberg and W. Kohn, “Inhomogeneous Electron gas,” *Phys. Rev. B.*, vol. 136, pp. 864-871, 1964.
- [74] M. Levy , “Universal Variational Functionals of Electron Densities, First-Order Density Matrices, and Natural Spin-Orbitals and Solution of the V-Representability Problem,” *Proc. Natl. Acad. Sci. U.S.A.*, vol. 76, p. 6062–6065, 1979.
- [75] L. J. Sham and W. Kohn, “Self-Consistent Equations including Exchange and Correlation Effects,” *Phys. Rev.*, vol. 140, pp. 1133-1138, 1965.
- [76] J. P. Perdew, A. Ruzsinszky, J. Tao, V. N. Staroverov, G. E. Scuseria and G. I. Csonka , “Prescription for the Design and Selection of Density Functional Approximations: More Constraint Satisfaction with Fewer Fits,” *J. Chem. Phys.*, vol. 123, p. 0622011–0622019, 2005.
- [77] A. E. Mattsson, P. A. Schultz, M. P. Desjarlais, T. R. Mattsson and K. Leung, “Designing Meaningful Density Functional Theory Calculations in Material Science,” *Modelling Simul. Mater. Sci. Eng.*, vol. 13, pp. 1-31, 2005.
- [78] J. P. Perdew and K. Schmidt, “Jacob's ladder of Density Functional Approximations for the Exchange-Correlation Energy,” *IP Conf. Proc.*, vol. A577, pp. 1-20, 2001.
- [79] J. P. Perdew and A. Zunger , “Self-Interaction Correction to Density-Functional Approximations for Many-Electron Systems,” *Phys. Rev. B.*, vol. 23, pp. 5048-5079, 1981.
- [80] S. H. Vosko, L. Wilk and M. Nusair, “Accurate Spin-Dependent Electron Liquid Correlation Energies for Local Spin Density Calculations: A Critical Analysis,” *Can. J. Phys.*, vol. 58, pp. 1200-1211, 1980.
- [81] D. M. Ceperley and B. J. Alder, “Ground State of the Electron Gas by a

- Stochastic Method," *Phys. Rev. Lett.*, vol. 45, pp. 566-569, 1980.
- [82] J. P. Perdew and Y. Wang , "Accurate and Simple Analytic Representation of the Electron Gas Correlation Energy," *Phys. Rev. B.*, vol. 45, pp. 13244-13249, 1992.
- [83] W. Koch and M. C. Holthausen, *A Chemist's Guide to Density Functional Theory*, Weinheim: Wiley-VCH Verlag GmbH, 2001, pp. 935-1818.
- [84] J. P. Perdew, J. A. Chevary, S. H. Vosko, K. A. Jackson, M. R. Pederson, D. J. Singh and C. Fiolhais, "Atoms, Molecules, Solids and Surfaces: Applications of the Generalized Gradient Approximation for Exchange and Correlation," *Phys. Rev. B.*, vol. 46, pp. 6671-6687, 1992.
- [85] J. P. Perdew and W. Yue, "Accurate and Simple Density Functional for the Electronic Exchange Energy: Generalized Gradient Approximation," *Phys. Rev. B*, vol. 33, pp. 8800-8802, 1986.
- [86] J. P. Perdew, "Density-Functional Approximation for the Correlation Energy of the Inhomogeneous electron Gas," *Phys. Rev. B.*, vol. 33, pp. 8822-8824, 1986.
- [87] A. D. Becke , "Density-functional Exchange-Energy approximation with Correct Asymptotic Behaviour," *Phys. Rev.*, vol. 38, pp. 3098-3100, 1988.
- [88] J. P. Perdew, K. Burke and M. Ernzerhof, "Generalized Gradient Approximation Made Simple," *Phys. Rev. Lett.*, vol. 77, pp. 3865-3868, 1996.
- [89] J. P. Perdew, K. Burke and Y. Wang, "Generalized Gradient Approximation for the Exchange-Correlation Hole of a many-Electron System," *Phys. Rev. B.*, vol. 54, p. 16533–16539, 1996.
- [90] L. Vitos, B. Johansson, J. Kollar and H. L. Skriver, "Exchange Energy in the Local Airy Gas Approximation," *Phys. Rev. B.*, vol. 62, pp. 10046-10050, 2000.
- [91] V. Milman, B. Winkler, J. A. White, C. J. Pickard, M. C. Payne, E. V. Akhmatkaya and R. H. Nobes., "Electronic Structure, Properties and Phase Stability of Inorganic Crystals: The Pseudopotential Plane-Wave Approach.," *J Quant Chem.*, vol. 77, pp. 895-910, 2000.
- [92] M. D. Segall, P. J. D. Lindan, M. J. Probert, C. J. Pickard, P. J. Hasnip, S. J. Clark and M. C. Payne, "First-principles Simulation: Ideas, Illustrations and the

- CASTEP code,” *J. Phys. Cond. Matt.*, vol. 14, pp. 2717 - 2744, 2002.
- [93] M. C. Payne, M. P. Teter, D. C. Allan, T. A. Arias and J. D. Joannopoulos, “Iterative Minimization Techniques for ab initio Total-Energy Calculations: Molecular Dynamic and Conjugate Gradients,” *Rev. Mod. Phys.*, vol. 64, pp. 1045-1097, 1992.
- [94] J. C. Phillips, “Energy-Band Interpolation Scheme Based on a Pseudopotential,” *Phys. Rev.*, vol. 112, pp. 685-695, 1958.
- [95] J. S. Blakemore, *Solid State Physics*, London: Cambridge University Press, 1985.
- [96] J. C. Phillips and L. Kleinman, “New Method for Calculating Wave Functions in Crystal and Molecules,” *Phys. Rev.*, vol. 116, pp. 287-294, 1959.
- [97] M. L. Cohen and V. Heine, “The Fitting of Pseudopotentials to Experiment Data and their Subsequent Application,” *Sol. State Phys.*, vol. 24, pp. 37-248, 1970.
- [98] H. Hellmann, “A New Approximation Method in the Problem of Many Electrons,” *J. Chem. Phys.*, vol. 3, p. 61, 1935.
- [99] W. E Pickett, “Pseudopotential Methods in Condensed Matter Applications,” *Comp. Phys. Rep.*, vol. 9, pp. 115-197, 1989.
- [100] D. Brust and B. Alder, *The Pseudopotential Method and the Single-Particle Electronic Excitation Spectra of Crystals*, *Methods in Computational Physics*, vol. 8, New York: Academic press, 1968, pp. 33-61.
- [101] H. J. Monkhorst and J. D. Pack, “On Special Points for Brillouin Zone Integrations,” *Phys. Rev. B.*, vol. 13, pp. 5188-5192, 1976.
- [102] N. J. Ramer and A. M. Rappe, “Virtual-Crystal Approximation that Works: Locating a Compositional Phase Boundary in  $\text{Pb}(\text{Zr}_{1-x}\text{Ti}_x)\text{O}_3$ ,” *Phys. Rev. B.*, vol. 62, pp. 743-745, 2000.
- [103] L. Bellaiche and D. Vanderbilt, “Virtual Crystal Approximation Revisited: Application to Dielectric and Piezoelectric Properties of Perovskites,” *Phys. Rev. B.*, vol. 61, pp. 7877-7782, 2000.
- [104] B. R. Sahu, “Electronic Structure and Bonding of Ultralight LiMg,” *Mater. Sci. Eng. B.*, vol. 49, p. 74–78, 1997.
- [105] V. I. Zubov, N. P. Tretiav, J. N. Teixeira Rabelo and J. F. Sanchez Ortiz,

- “Calculations of the Thermal Expansion Cohesive Energy and Thermodynamic Stability of a Van der Waals Crystal - Fullerene C60,” *Phys. Lett. A.*, vol. 198, pp. 223-227, 1995.
- [106] M. J. Mehl, B. M. Klein and D. A. Papaconstantopoulos, “First-Principles Calculation. of Elastic Properties,” in *Intermetallic Compounds*, London, John Wiley & Sons Ltd, 1994, pp. 195-2010.
- [107] J. Chen, L. L. Boyer, H. Krakauer and M. J. Mehl, “Elastic Constants of NbC and MoN: Instability of B1-MoN,” *Phys. Rev. B.*, vol. 37, pp. 3295-3298, 1988.
- [108] B. B. Karki, G. J. Ackland and J. Crain , “Elastic Instability in Crystal from ab initio Stress-Strain Relations,” *J. Phys. Condens. Matter.*, vol. 9, pp. 8579-8589, 1997.
- [109] Y. Le Page and P. Saxe, “Symmetry-General Least-Squares Extraction of Elastic Coefficients from Ab Initio Total Energy Calculations,” *Phys. Rev. B.*, vol. 63, pp. 1741031-1741038, 2001.
- [110] G. Ghosh and G. B. Olson, “The Isotropic Shear Modulus of Multicomponent Fe-Base Solid Solutions,” *Acta Mater.*, vol. 50, p. 2655–2675, 2002.
- [111] R. Labusch, “Statistical Theories of Solid Solution Hardening,” *Acta Metall.* , vol. 20, pp. 917-927, 1972.
- [112] F. R. N. Nabarro, “The Theory of Solution Hardening,” *Phil. Mag.* , vol. 35, pp. 613-622, 1977.
- [113] S. Kamran, K. Chen and L. Chen , “Ab Initio Examination of Ductility Features of fcc Metals,” *Phys. Rev. B.*, vol. 79, pp. 0241061-0241068, 2009.
- [114] S. Goumri-Said and M. B. Kanoun, “Theoretical Investigations of Structural, Elastic, Electronic and Thermal Properties of Damiaoite PtIn<sub>2</sub>,” *Comp. Mat. Sci.*, vol. 43, p. 243–250, 2008.
- [115] B. B. Karki, G. J. Ackland and J. Crain, “Elastic Instabilities in Crystals from Ab Initio Stress–Strain,” *J. Phys. Condens. Matter.*, vol. 9, p. 8579–8589, 1997.
- [116] A. Al-Ghaferi, P. Mullner, H. Heinrich, G. Kostorz and J. M. K. Wiezorek, “Elastic Constants of Equiatomic L10-Ordered FePd Single Crystals,” *Acta Mater.*, vol. 54, p. 881–889, 2006 .
- [117] İ. Erdem, H. Hüseyin Kart and T. Cagin , “First Principles Studies of SnO at

- Different Structures,” *Mater Sci Eng.*, vol. 45, pp. 108-113, 2010.
- [118] R. Hill, “The Elastic Behaviour of a Crystalline Aggregate,” *Proc. Phys. Soc.*, vol. 65, pp. 349-354, 1952.
- [119] B. D. Fulcher, X. Y. Cui, B. Delley and C. Stamp, “Hardness Analysis of Cubic Metal Mononitrides from First Principle,” *Phys. Rev. B.*, vol. 85, pp. 1841061-1841069, 2012.
- [120] G. Ackland, “Embrittlement and the bistable crystal structure of zirconium hydride,” *Phys. Rev. Lett.*, vol. 80, pp. 2233-2236, 1998.
- [121] D. Vanderbilt, “Soft Self-Consistent Pseudopotentials in Generalized Eigenvalue Formalism,” *Phys. Rev. B.*, vol. 41, pp. 7892-7894, 1990.
- [122] R. Hamann, M. Schluter and C. Chiang, “Norm-Conserving Pseudopotentials,” *Phys. Rev. Lett.*, vol. 43, pp. 1494-1497, 1979.
- [123] C. J. Howard, R. J. Hill and B. E. Reichert, “Structures of ZrO<sub>2</sub> Polymorphs at Room Temperature by High-Resolution Neutron Powder Diffraction,” *Acta Cryst.*, vol. 44, pp. 116-120, 1988.
- [124] X. Zhao and D. Vanderbilt, “Phonons and Lattice Dielectric Properties of Zirconia,” *Phys. Rev. B.*, vol. 65, p. 075105, 2002.
- [125] L. K. Dash, N. Vast, P. Baranek, M. C. Cheynet and L. Reining, “Electronic Structure and Electron Energy-Loss Spectroscopy of ZrO<sub>2</sub> Zirconia,” *Phys. Rev. B.*, vol. 70, pp. 2451161-24511617, 2004.
- [126] G. Jomard, T. Petit, A. Pasturel, L. Magaud, G. Kresse and J. Hafner, “First-Principles Calculations to Describe Zirconia Pseudopolymorphs,” *Phys. Rev. B.*, vol. 59, p. 4044–4052, 1999.
- [127] S. Fabris, A.T. Paxton and M.W. Finnis, “Relative Energetics and Structural Properties of Zirconia Using a Self-Consistent Tight-Binding Model,” *Phys. Rev. B.*, vol. 61, pp. 6617-6630, 2000.
- [128] A. P. Mirgorodsky and P. E. Quintard, “Lattice-Dynamic Treatment of Vibrational and Elastic Properties of Cotunnite-Type ZrO<sub>2</sub> and HfO<sub>2</sub>: Comparison with Ambient Pressure Polymorphs,” *J. Am. Ceram. Soc.*, vol. 82, p. 3121–3124, 1999.
- [129] J. E. Jaffe, R. A. Bachorz, and M. Gutowski, “Low-Temperature Polymorphs of

- ZrO<sub>2</sub> and HfO<sub>2</sub>: A Density-Functional Theory Study,” *Phys. Rev. B.*, vol. 72, p. 144107, 2005.
- [130] P. A. Lee, G. Said and R. Davis, “Negative Resistance and Switching Effect in the Single Crystal Layer Compounds SnS<sub>2</sub> and ZrS<sub>2</sub>,” *Solid State Comm.*, vol. 7, p. 1359–1361, 1969.
- [131] P. K. Lam, M. L. Cohen and G. Martinez, “Analytic Relation Between Bulk Moduli and Lattice Constants,” *Phys. Rev. B.*, vol. 35, p. 9190–9194, 1987.
- [132] R. L. Fleishcher , “Effects of Non-Uniformities on the Hardening of Crystals,” *Acta Metall.*, vol. 8, p. 598–604, 1960.
- [133] S. Fabris, A. T. Paxton and M. W. Finnis, “Relative Energetics and Structural Properties of Zirconia Using a Self-Consistent Tight-Binding Model,” *Phys. Rev. B.*, vol. 61, pp. 6617-6630, 2000.
- [134] D. K. Smith and H. W. Newkirk, “The Crystal Structure of Baddeleyite (Monoclinic ZrO<sub>2</sub>) and its Relation to the Polymorphism of ZrO<sub>2</sub>,” *Acta Crystallogr.*, vol. 18, pp. 983-991, 1965.
- [135] Z. T. Sui, X. Y. Xiao, K. Q. Huang and C. Z. Wang, “Standard Gibbs Free Energy of Formation of ZrOS,” *J. Less. Common. Met.*, vol. 163, p. 109–113, 1990.
- [136] H. Jiang, R. I. Gomez-Abal, P. Rinke and M. Scheffler, “Electronic Band Structure of Zirconia and Hafnia Polymorphs from GW Perspective,” *Phys. Rev. B.*, vol. 81, pp. 0851191-0851199, 2010.
- [137] B. Kralik, E. K. Chang and S. G. Louie, “Structural Properties and Quasiparticle Band Structure of Zirconia,” *Phys. Rev. B.*, vol. 57, pp. 7027-7036, 1998.
- [138] Y. S. Kim, H. C. Ko and H. S. Park, “Electronic Structure and Chemical Bonding of Zirconium disulfide,” *Mat Mater.*, vol. 6, pp. 177-180, 2000.
- [139] G. K. Wertheim, F. J. Di Salvo and D. N. E. Buchanan, “Valence band of Layer Structure Transition Metal Chalcogenides,” *Sol. State Comm.*, vol. 13, p. 12225, 1973.
- [140] H. M. Kandil, J. D. Greiner and J. F. Smith, “Single-Crystal Constants of Ytria-Stabilized Zirconia in the Range 20°C to 700°C,” *J. Am. Ceram. Soc.*, vol. 67, pp. 341-346, 1984.

- [141] R. Orlando, C. Pisani and C. Roetti, "Ab initio Hartree-Fock Study of Tetragonal and Cubic Phases of Zirconium dioxide," *Phys. Rev. B.*, vol. 45, pp. 592-601, 1992.
- [142] R. E. Cohen, M. J. Mehl and L. L. Boyer, "Phase transitions and Elasticity in Zirconia," *Physica B.*, vol. 150, pp. 1-9, 1988.
- [143] A. P. Mirgorodsky, M. B. Smirnov and P. E. Quintard, "Lattice-Dynamical Study of the Cubic-Tetragonal-Monoclinic Transformations of Zirconia," *Phys. Rev. B.*, vol. 55, pp. 19-22, 1997.
- [144] S. Chan, Y. Fang, M. H. Grinsditch, Z. Li, M. V. Nevitt, W. M. Robertson and E. S. Zouboulis, "Temperature Dependence of the Elastic Moduli of Monoclinic Zirconia," *J. Am. Ceram. Soc.*, vol. 74, pp. 1742-1744, 1991.
- [145] E. H. Kisi and C. J. Howard, "Elastic Constants of Tetragonal Zirconia Measured by a New Powder Diffraction Technique," *J. Am. Ceram. Soc.*, vol. 81, p. 1682-1684, 1998.
- [146] S. K. Chan, "private communication, reported in Kisi and Howard," *J. Am. Ceram. Soc.*, vol. 81, pp. 1682-1684, 1998.
- [147] M. V. Nevitt, S. Chan, J. Z. Liu, M. H. Grinsditch, and Y. Fang, "The Elastic Properties of Monoclinic  $ZrO_2$ ," *Physica B.*, vol. 152, pp. 230-233, 1988.
- [148] G. Fadda, L. Colombo and G. Zanzotto, "First-Principles Study of the Structural and Elastic Properties of Zirconia," *Phys. Rev. B.*, vol. 79, p. 214102, 2009.
- [149] F. Birch, "Finite Strain Isotherm and Velocities for Single-Crystal and Polycrystalline NaCl at High Pressures and 300 K," *J. Geophys. Res.*, vol. 83, pp. 1257-1268, 1978.
- [150] R. H. Baughman, J. M. Shacklette, A. A. Zakhidov and S. Stafstrom, "Negative Poisson's Ratios as a Common Feature of Cubic Metals," *Nature*, vol. 392, pp. 362-365, 1998.
- [151] D. G. Pettifor, "Theoretical predictions of structure and related properties of intermetallics.," *Mater. Sci. Technol.*, vol. 8, p. 345-349, 1992.
- [152] C. L. Fu and M. H. Yoo, "Elastic Constants, Fault Energies, and Dislocation Reactions in TiAl: A First-Principles Total-Energy Investigation," *Philos. Mag. Lett.*, vol. 62, pp. 159-165, 1990.

- [153] D. Nguyen-Manh, V. Vitek and A. P. Horsfield , “Environmental Dependence of Bonding: A Challenge for Modelling of Intermetallics and Fusion Materials,” *Prog Mater Sc.*, vol. 52, pp. 255-298, 2007.
- [154] X. H. Deng, W. Lu, Y. M. Hu and H. S. Gu, “The Elastic Properties of Hexagonal Osmium Under Pressure: The First-Principles Investigations,” *Physica B.*, vol. 404, p. 1218–1221, 2009.
- [155] Q. J. Liu, Z. T. Liu and L. P. Feng, “Elastic ,Electronic Structure, Chemical bonding and Optical Properties of Monoclinic ZrO<sub>2</sub> from First-Principles,” *Physica B.*, vol. 406, pp. 345-350, 2011.
- [156] D. Lerch, O. Wiekhorst, G. L. W. Hart, R. W. Forcade and S. Muller, “UNCLE:a Code for Constructing Cluster Expansions for Arbitrary Lattices with Minimal User-Input,” *Modelling Simul. Mater. Sci. Eng.*, vol. 17, pp. 0550121-05501218, 2009.
- [157] S. Curtarolo, W. Setyawan, G. L. W. Hart, M. Jahnatek, R. V. Chepulskii, R. H. Taylor, S. Wang, J. Xue, K. Yang, O. Levy, M. Mehl, H. T. Stokes, D. O. Demchenko and D. Morgan, “AFLOW: an Automatic Frame-Work for High-Throughput Materials Discovery,” *Comp. Mat. Sci.*, vol. 58, pp. 218-226, 2012.
- [158] S. Curtarolo, W. Setyawan, S. Wang, J. Xue, K. Yang, R. H. Taylor, L. J. Nelson, G. L. W. Hart, S. Sanvito, M. Buongiorno Nardelli, N. Mingo, and O. Levy, “AFLOWLIB.ORG: A distributed materials properties repository from high-throughput ab initio calculations,,” *Comp. Mat. Sci.*, vol. 58, pp. 227-235, 2012.